UNIVERSIDAD DISTRITAL
FRANCISCO JOSÉ DE CALDAS

REVISTA Ingeniería

Four-monthly scientific journal

2024

Volume 29 - Issue 3 ISSN 0121-750X E-ISSN 23448393

REVISTA Ingeniería

Volume 29 · Issue 3 · Year 2024 · ISSN 0121-750X · E-ISSN 2344-8393

Four-monthly Scientific Journal

UNIVERSIDAD DISTRITAL
FRANCISCO JOSÉ DE CALDAS

Carrera 7 No. 40-53
Edificio Administrativo
Piso 7 - Facultad de Ingeniería
Bogotá, Colombia
Teléfono: + 57 (1) 323 93 00 ext. 2413
Correo revista:
revista_ing@udistrital.edu.co

http://revistas.udistrital.edu.co/ojs/index.php/reving

Focus and Scope

The *Ingeniería* journal is an open-access academic-scientific online publication specialized in knowledge related to the fields of Engineering and Technology, according to the classification of scientific areas established by the Organization for Economic Cooperation and Development (OECD). Its main goal is to disseminate and promote debates about advances in research and development in the diverse areas of Engineering and Technology. We focus on disseminating original and unpublished articles in English that are relevant at both the national and international level. We seek to provide a platform to share knowledge and foster collaboration between researchers and professionals in the field. The journal does not request any Article Processing Charges (APC), as it is directly funded by Universidad Distrital Francisco José de Caldas. Moreover, the journal operates following a double-blind review process, thus ensuring the impartiality and quality of the published works. The journal is published in a continuous fashion and follows a quarterly numbering.

Editors

Scientific and Editorial Committee

Directives

Technical Committee

Open Access Policy

The *Ingeniería* journal provides free access to its content. This free access is granted under the principle of making research freely available to the public, which en-courages a greater exchange of global knowledge.

Article Processing Charge

No publication fees are charged to the authors or their institutions, nor are any payments made to expert peer reviewers or associate or adjunct editors. The *Ingeniería* journal is funded by Universidad Distrital Francisco José de Caldas, its Faculty of Engineering, and its Central Research Office.

Indexed in

Scopus
Publindex Colombia Categoría B
Directorio Latindex
Applied Science & Technology Source Ultimate (EBSCO)
Fuente Académica Plus (EBSCO)
Catálogo 2.0 Latindex
Dialnet
Google Schola Metrics
MIAR

SciELO
Redalyc
Fuente Académica Premier (EBSCO)
Emerging Sources Citation Index Bibliographic Bases (SC)
OpenAlex
DOAJ
ROAD
PKP Index

Peer-reviewers in this Issue

Hans Dieter Betz
Ludwig-Maximilians-Universität München, Germany

Zhu Li
College of Electronics and Information, Hangzhou
Dianzi University, China

Irvin López-García
Universidad Autónoma Metropolitana – Azcapotzalco, Mexico

Andrzej Karbowski
Politechnika Warszawska, Poland

José Francisco Gómez-Aguilar
Centro Nacional de Investigación y Desarrollo
Tecnológico, Mexico

Alexander Molina-Cabrera
Universidad Tecnológica de Pereira, Colombia

Carlos Andrés Ramos-Paja
Universidad Nacional de Colombia, Colombia

Ajoy Kanti Mondal
Institute of National Analytical Research and Service,
Bangladesh Council of Scientific and Industrial
Research, Bangladesh

Zhiqiang Chen
Northwest Institute of Nuclear Technology, Xi'an, China

Mario Andrés Noriega-Valencia
Universidad Nacional de Colombia, Colombia

Jesús de la Casa Hernández
Universidad de Jaén, Spain

Jesus Maria Lopez Lezama
Universidad de Antioquia, Colombia

Bruno Domenech
Universitat Politécnica de Catalunya, Spain

Abdelraouf M Ishtaiwi
University of Petra, Jordan

Ramesh C Bansal
University of Sharjah, United Arab Emirates

Gabriel Avelino Sampedro
University of the Philippines Open University, Faculty
of Information and Communication Studies, Philippines

Table of contents

Editorial

Environmental Engineering

Mechanical Engineering

Electrical, Electronic and Telecommunications Engineering

Computational Intelligence

Chemical, Food, and Environmental Engineering

Education in Engineering

UNIVERSIDAD DISTRITAL
FRANCISCO JOSÉ DE CALDAS

Ingeniería

https://revistas.udistrital.edu.co/index.php/reving/issue/view/1241

DOI: https://doi.org/10.14483/23448393.22697

Editorial

Solving the Power Flow Problem in Transmission Networks Using Nonlinear Complex-Domain Modeling Via Julia Software

Oscar Danilo Montoya[1], Edwin Rivas-Trujillo[1], and Walter Gil-González[2]

[1]Universidad Distrital Francisco José de Caldas, Colombia
[2]Universidad Tecnológica de Pereira

Solving the power flow problem for transmission grids is crucial for ensuring the reliable and efficient operation of electrical power systems. Power flow analysis allows engineers to determine the voltage, current, and power flow of a network, which is essential for maintaining system stability and avoiding overloads. Accurate power flow solutions help to identify potential issues such as voltage drops, line losses, and system inefficiency, enabling the proactive maintenance and optimization of the network. This analysis is vital for integrating renewable energy sources, as it ensures effective power distribution even under variable generation conditions. Ultimately, solving the power flow problem enhances the overall resilience, reliability, and economic performance of transmission networks, supporting a stable supply of electricity to consumers.

1. Complex-variable power flow modeling

For electrical systems, the power flow problem can be formulated as a complex-variable optimization model (1). This optimization problem takes the following form:

Objective function:

$$\text{mín}\, P_{\text{loss}} = \mathbf{Re}\left\{\sum_{k\in\mathbf{N}}\sum_{m\in\mathbf{N}} \mathbb{V}_k^{\star}\mathbb{Y}_{km}\mathbb{V}_m\right\}, \tag{1}$$

where P_{loss} represents the active power losses in the transmission system; $\mathbb{V}_k$ and $\mathbb{V}_m$ correspond to the voltage variables in the complex domain that are assignable to nodes k and m; $\mathbb{Y}_{km}$ is the component of the nodal admittance matrix that relates nodes k and m; and $\mathbf{N}$ represents the set that contains all the nodes in the system. Note that the operator $\mathbf{Re}\left\{\mathbb{X}\right\}$ obtains the real part of the complex variable $\mathbb{X}$, while the operator $\mathbb{X}^{\star}$ obtains its complex conjugate.

Editorial

Set of constraints:

$$\mathbb{S}^{\star}_{g,k} - \mathbb{S}^{\star}_{d,k} = \mathbb{V}^{\star}_{k} \sum_{m\in\mathbf{N}} \mathbb{Y}_{km}\mathbb{V}_{m}, \ \{\forall k \in \mathbf{N}\} \tag{2}$$

$$\mathbb{V}_s = V_s\angle 0, \ s = \text{slack node} \tag{3}$$

$$|\mathbb{V}_j| = V_j, \ j = \text{PV nodes} \tag{4}$$

$$\mathbf{Re}\left\{\mathbb{S}_{g,j}\right\} = P_{g,j}. \ j = \text{PV nodes} \tag{5}$$

where $\mathbb{S}_{g,k}$ corresponds to the complex power injected by the generator connected to node k; $\mathbb{S}_{d,k}$ represents the complex power demanded at node k; $\mathbb{V}_s$ denotes the complex voltage assigned to the slack node (reference bus), whose magnitude is V_s; V_j corresponds to the magnitude of the voltage assignable to the nodes; and $P_{g,j}$ is the active power assigned to these nodes.

It is important to mention that the formulation (1)–(5) can also represent the optimal power flow problem in the complex domain if the active power constraint assigned to the PV nodes is relaxed, allowing them to move within their maximum and minimum capacity limits (2).

2. The IEEE-WSCC

To illustrate the solution to the power flow problem in transmission systems according to the formulation (1)-(5), consider the IEEE-WSCC (Western System Coordinating Council) system, whose impedance and nodal voltage data are shown in Fig. 1. Note that the data reported in this figure were obtained by applying the Newton-Raphson method (3).

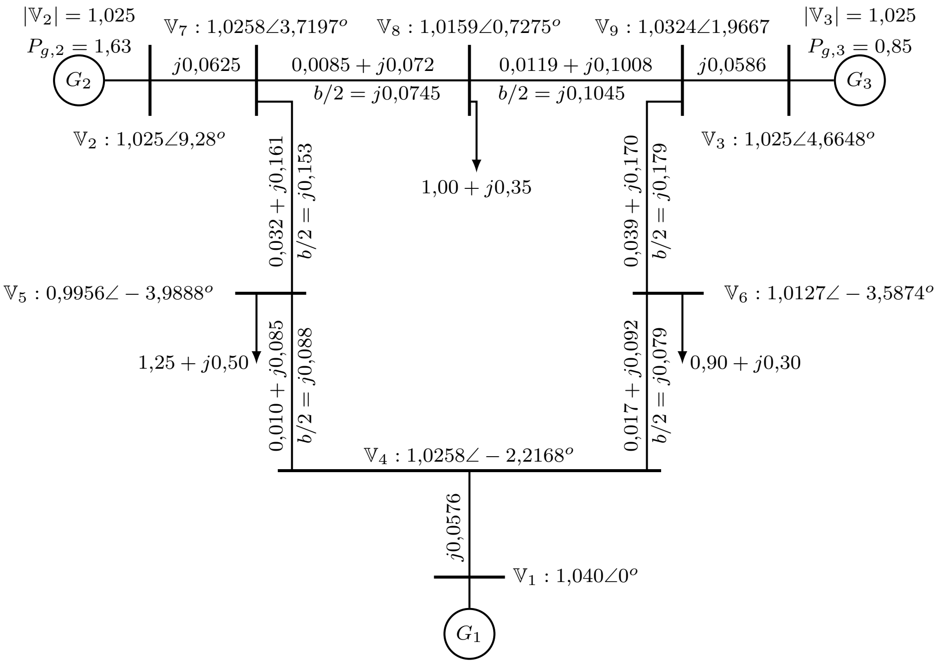

Figure 1. IEEE-WSCC (adapted from (4))

3. Julia software implementation

This section illustrates the computational implementation of the mathematical model (1)-(5) in the Julia software, using the `Ipopt` solver in the `JuMP` optimization environment (5).

```
using DataFrames, LinearAlgebra
Vb = 1; Sb = 100; Zb = 1;
branch_data = DataFrames.DataFrame([
(1,4,0.0000,0.0576,0.0000),(2,7,0.0000,0.0625,0.0000),
(3,9,0.0000,0.0586,0.0000),(4,5,0.0100,0.0850,0.1760),
(4,6,0.0170,0.0920,0.1580),(5,7,0.0320,0.1610,0.3060),
(6,9,0.0390,0.1700,0.3580),(7,8,0.0085,0.0720,0.1490),
(8,9,0.0119,0.1008,0.2090),]);
DataFrames.rename!(branch_data, [:k,:m,:Rkm,:Xkm,:Bk])
node_data = DataFrames.DataFrame([
(1,  3, 1.040,   0.0,  0.0,   0.0, 0.0),
(2,  2, 1.025,   0.0,  0.0, 163.0, 0.0),
(3,  2, 1.025,   0.0,  0.0,  85.0, 0.0),
(4,  0, 1.000,   0.0,  0.0,   0.0, 0.0),
(5,  0, 1.000, 125.0, 50.0,   0.0, 0.0),
(6,  0, 1.000,  90.0, 30.0,   0.0, 0.0),
(7,  0, 1.000,   0.0,  0.0,   0.0, 0.0),
(8,  0, 1.000, 100.0, 35.0,   0.0, 0.0),
(9,  0, 1.000,   0.0,  0.0,   0.0, 0.0),]);
DataFrames.rename!(node_data, [:k, :type, :Vk0,
                   :Pdk, :Qdk, :Pgk, :Qgk])
N = size(node_data,1); L = size(branch_data,1)
A = zeros(N,L)
for l = 1:L
    k = branch_data.k[l]; m = branch_data.m[l]
    A[k,l] = 1;  A[m,l] = -1
end
z = (branch_data.Rkm .+ im*branch_data.Xkm)/Zb
Sd = (node_data.Pdk .+ im*node_data.Qdk)/Sb
Sgo = (node_data.Pgk .+ im*node_data.Qgk)/Sb
Ybus = A*inv(diagm(z))*transpose(A)
for l = 1:L
    k = branch_data.k[l]; m = branch_data.m[l]
    Ybus[k,k] = Ybus[k,k] + 1*im*branch_data.Bk[l]/2;
    Ybus[m,m] = Ybus[m,m] + 1*im*branch_data.Bk[l]/2;
end
using JuMP, Ipopt
PF = Model(Ipopt.Optimizer);
@variable(PF, Sg[k in 1:N] in ComplexPlane());
@variable(PF,V[k in 1:N] in ComplexPlane(),
```

```
          start = 1.0 + 0.0im);
for k in 1:N
    if node_data.type[k] == 3
        @constraint(PF,V[k] == node_data.Vk0[k] + 0*im);
    elseif node_data.type[k] == 2
        @constraint(PF,abs2(V[k])==(node_data.Vk0[k])^2);
        @constraint(PF,real(Sg[k]) == real(Sgo[k]));
    else
        @constraint(PF, Sg[k] == 0);
    end
    @constraint(PF,conj(Sg[k]) -  conj(Sd[k]) ==
    conj(V[k])*sum(Ybus[k,m]*V[m] for m = 1:N))
end
@objective(PF,Min,Sb*real(sum(conj(V[k])*
sum(Ybus[k,m]*V[m] for m = 1:N) for k = 1:N)));
JuMP.optimize!(PF)
@show objective_value(PF);
bus_data = DataFrames.DataFrame(;k = 1:N,
Vmag = round.(abs.(value.(V)), digits = 4),
Vang = round.(angle.(value.(V))*180/pi, digits = 4),
Pg = round.(real(value.(Sg)),digits = 4),
Qg = round.(imag(value.(Sg)),digits = 4))
```

By executing this computational routine, the following results are obtained:

```
EXIT: Optimal Solution Found.
objective_value(PF) = 4.6410214744826453
 Row k      Vmag     Vang     Pg       Qg
   1     1   1.04     0.0      0.7164   0.2705
   2     2   1.025    9.28     1.63     0.0665
   3     3   1.025    4.6648   0.85    -0.1086
   4     4   1.0258  -2.2168   0.0      0.0
   5     5   0.9956  -3.9888  -0.0      0.0
   6     6   1.0127  -3.6874  -0.0      0.0
   7     7   1.0258   3.7197  -0.0     -0.0
   8     8   1.0159   0.7275   0.0      0.0
   9     9   1.0324   1.9667  -0.0      0.0
```

Thus, it is possible to note that:

i. The electrical variables, *i.e.*, the magnitude and angle of the voltages at each of the buses, are equivalent to the solution obtained using the Newton-Raphson method (Fig. **1**) (3).

ii. Under the given operating conditions, the active power losses for this system amount to 4.6410 MW.

Remark 1. *Suppose that the programmer is interested in solving the optimal power flow problem for transmission networks. In this scenario, the active power injection at the PV buses is left unconstrained, allowing the programmer to determine the optimal combination of these power inputs in order to minimize the total grid power losses.*

Conclusion

This editorial note provides an easily implementable computational routine to deal with the power flow problem in transmission networks, which can be extended to any single-phase AC grid, using a complex-domain variable formulation. The solution to the power flow problem is obtained via the interior point optimizer (*i.e.*, the `Ipopt` solver) available in Julia's `JuMP` optimization environment. This routine is presented as a tutorial, using the IEEE-WSCC network to demonstrate that the power flow solution is equivalent to the solution reached with the classical Newton-Raphson method.

Acknowledgment

This research received support from the Ibero-American Program of Science and Technology for Development (CYTED), through the thematic network 723RT0150, *i.e.*, *Red para la integración a gran escala de energías renovables en sistemas eléctricos* (RIBIERSE-CYTED).

Referencias

[1] O. D. Montoya, C. A. Ramírez-Vanegas, and J. R. González-Granada, "Dynamic active and reactive power compensation in distribution networks using pv-statcoms: A tutorial using the julia software," *Res. Eng.*, vol. 21, p. 101876, Mar. 2024. https://doi.org/10.1016/j.rineng.2024.101876↑ 1

[2] X. Bai, H. Wei, K. Fujisawa, and Y. Wang, "Semidefinite programming for optimal power flow problems," *Int. J. Elec. Power Energy Sys.*, vol. 30, no. 6–7, pp. 383–392, Jul. 2008. https://doi.org/10.1016/j.ijepes.2007.12.003↑ 2

[3] A. Garcés-Ruiz, W. J. Gil-González, and O. D. Montoya-Giraldo, *Introducción a la estabilidad de sistemas eléctricos de potencia*. Pereira, Colombia: Universidad Tecnológica de Pereira, 2023. https://doi.org/10.22517/9789587228960↑ 2, 4

[4] P. Anderson and A. Fouad, *Power system control and stability*. Piscataway, NJ: Wiley-Interscience, 2003. https://ieeexplore.ieee.org/servlet/opac?bknumber=5264012↑ 2

[5] J. Bezanson, A. Edelman, S. Karpinski, and V. B. Shah, "Julia: A fresh approach to numerical computing," *SIAM Rev.*, vol. 59, no. 1, pp. 65–98, 2017. https://doi.org/10.1137/141000671↑ 3

Oscar Danilo Montoya

Compatibility and Electromagnetic Interference group, Department of Engineering, Universidad Distrital Francisco José de Caldas; Electrical Engineer, Master of Electrical Engineering, and PhD in Engineering.
Email: odmontoyag@udistrital.edu.co

Edwin Rivas-Trujillo

Compatibility and Electromagnetic Interference group, Department of Engineering, Universidad Distrital Francisco José de Caldas; Electrical Engineer, Master of Electrical Engineering, and Master and PhD in Electrical Engineering, Electronics, and Automation.

Email: erivas@udistrital.edu.co

Walter Gil-González

Electromagnetic Fields and Energy Phenomena group, Department of Engineering, Universidad Tecnológica de Pereira; Electrical Engineer, Master of Electrical Engineering, PhD in Engineering, and PhD in Renewable Energy.

Email: wjgil@utp.edu.co

UNIVERSIDAD DISTRITAL
FRANCISCO JOSÉ DE CALDAS

Ingeniería

https://revistas.udistrital.edu.co/index.php/reving/issue/view/1241

DOI: https://doi.org/10.14483/23448393.22136

Research

Lightning Occurrence between 2016 and 2020 in Fusagasugá, Cundinamarca, Colombia

Ocurrencia de rayos entre 2016 y 2020 en Fusagasugá, Cundinamarca, Colombia

Fernando Díaz-Ortíz[1]*, Neyder Perilla López[2], Juan Ospina Carrillo[2], and Pedro Cifuentes Guerrero[1]

[1]Electronics Engineering Program, Universidad de Cundinamarca, Fusagasugá, Colombia
[2]Systems and Computer Engineering Program, Universidad de Cundinamarca, Fusagasugá, Colombia

Abstract

Context: Lightning is a powerful natural phenomenon that poses a risk to life and infrastructure, given the enormous amounts of energy it can transfer in short periods of time, especially in cloud-to-ground strikes. Since lightning requires specific meteorological conditions for its generation, its occurrence is often influenced by conditions such as topography, rainfall, and wind patterns. Therefore, having information about lightning occurrences in a region is crucial for comprehensive risk management against this extreme natural phenomenon.
Methods: In this study, we implemented a methodology based on knowledge discovery in databases (KDD) to analyze and visualize data provided by Vaisalas's GLD360 lightning location network.
Results: The results indicate that, in Fusagasugá, Cundinamarca, there are two lightning activity peaks: one in the first half of the year (March) and another in the second half (October). Lightning events are most frequent during the afternoon, with a peak around 5:00 p.m. (local time). Additionally, most lightning events occur in two areas with low population density, covering 25 % of the territory and ranging from 500 to 1000 meters above sea level.
Conclusions: These findings highlight the importance of precise knowledge regarding the location of lightning events for planning prevention and risk management. In this case, efforts and resources should primarily focus on a small proportion of the municipality to substantially impact the population and infrastructure.

Keywords: lightning, atmospheric electrical discharge, climatology, lightning location

Article history

Received:
7th /May/2024

Modified:
15th /Jun/2024

Accepted:
30th /Jul/2024

Ing, vol. 29, no. 3,
2024. e22136

---

* **Correspondence:** faugustodiaz@ucundinamarca.edu.co

Resumen

Contexto: Los rayos son un fenómeno natural poderoso que representa un riesgo para la vida y la infraestructura, pues puede transferir enormes cantidades de energía en cortos periodos de tiempo, especialmente en descargas nube-tierra. Dado que los rayos requieren condiciones meteorológicas específicas para su generación, su ocurrencia suele estar influenciada por factores como la topografía, la precipitación y los patrones de viento. Por lo tanto, contar con información sobre la ocurrencia de rayos en una región es crucial para una gestión integral del riesgo frente a este fenómeno natural extremo.
Métodos: En este estudio se implementó una metodología basada en la extracción de conocimiento en bases de datos (KDD) para analizar y visualizar los datos proporcionados por la red de localización de rayos GLD360 de Vaisala.
Resultados: Los resultados indican que, en Fusagasugá, Cundinamarca, existen dos picos de actividad de rayos: uno en la primera mitad del año (marzo) y otro en la segunda mitad (octubre). Los eventos de rayos son más frecuentes durante la tarde, con un pico alrededor de las 5:00 p.m. (hora local). Además, la mayoría de los eventos de rayos ocurren en dos áreas con baja densidad poblacional, que cubren el 25 % del territorio y se encuentran a una altitud de entre 500 y 1000 metros sobre el nivel del mar.
Conclusiones: Estos hallazgos destacan la importancia de contar con un conocimiento preciso sobre la ubicación de los eventos de rayos para la planificación de la prevención y la gestión del riesgo. En este caso, los esfuerzos y recursos deben centrarse principalmente en una pequeña proporción del municipio para tener un impacto sustancial en la población y la infraestructura.

Palabras clave: rayos, descargas eléctricas atmosféricas, climatología, localización de rayos

Table of contents

1. Introduction

Atmospheric electrical discharges, commonly known as *lightning*, are intense natural phenomena originating within storm clouds (1). Lightning flashes are the optical manifestation of a lightning strike, while thunder is the acoustic counterpart. Most lightning occurs within storm clouds, with only a small percentage striking between the clouds and the ground. However, in regions with intense electrical activity, cloud-to-ground lightning strikes can pose significant risks to infrastructure and life (2).

The occurrence of lightning is neither uniform in time nor space and depends on factors such as the variability of rainfall patterns (3), moisture transport due to wind regimes (4), and particular topographical features (5). Regions like the Congo River basin (6) and northern South America are known for their intense lightning activity (7). This includes parts of the Andean region, the Colombian Caribbean region, and the Maracaibo Lake region in Venezuela, where lightning activity is notably higher than the global average (8) (9).

Lightning data are obtained from measurement stations located at ground level or on satellite platforms (10). Since lightning occurs within storm clouds, the electromagnetic fields generated by the clouds' electrical activity are usually measured. Stations detect variations in the electric and magnetic fields caused by each discharge, known as *strokes*. A lightning flash generally consists of one or more strokes, a phenomenon dubbed *lightning multiplicity* (11).

Measurement stations are often part of lightning observation networks, with some offering free access to databases with information about lightning strike locations and electrical parameters. This information is crucial for studying the specifics of lightning's electrical parameters and apparent occurrence patterns (12). The latter focuses on the time and location of lightning occurrences, which is essential for designing lightning risk management plans and warning against extreme weather events.

This work sought to determine the lightning climatology of Fusagasugá, Cundinamarca, given the lack of detailed studies in the area. This municipality, with over 150 000, inhabitants is located 60 km from the city of Bogotá and settled on uneven terrain at around 1700 meters above sea level. This study aims to contribute to scientific knowledge and provide relevant information for local authorities involved in prevention and risk management.

Most of the electrical activity in storm clouds occurs internally, so obtaining optical records is challenging. Therefore, almost all lightning detection systems rely on observing variations in ambient electric and magnetic fields. Electric field and loop antennas are commonly used for this purpose. To determine the impact point of a lightning strike, simultaneous measurements from multiple antennas are necessary, to verify the discharge and establish its coordinates. Over time, several regional, national, and global networks have recorded lightning activity. The World Wide Lightning Location Network (WWLLN), an academic initiative, is widely used in several lightning climatology studies. Moreover, the GLD360 lightning location network, managed by Finnish company Vaisala, utilizes magnetic field sensors and the time-of-arrival (TOA) method for lightning location.

Technological advancements have enabled the study of storm cloud electrical activity from satellite platforms, sometimes using adapted versions of ground sensors. However, the primary focus is detecting light emissions from the top of the cloud, as is the case of the Tropical Rainfall Measuring Mission/Lightning Imaging Sensor (TRMM/LIS) project and the Geostationary Lightning Mapper (GLM). Combined, these lightning location networks have facilitated the creation of lightning climatologies, which are crucial for evaluating and managing the risks that lightning poses to populations and infrastructure.

Some studies have identified regions with electrical activity above the global average in South China (13), the Congo River basin (6), and northern Asia (12). Other studies have examined national climatologies in places like Sri Lanka (14), South Africa (15), Poland (16), Bangladesh (17), and Australia (18). Studies in Colombia have focused on identifying spatial and temporal patterns across the country, as seen in (19, 20). Regional patterns have also been analyzed, such as those in the north of Colombia (2, 21) and the department of Santander (22). All cited studies agree on identifying intense lightning activity, particularly concentrated in the middle basin of the Magdalena River and the Momposina Depression. As an example, Fig. **1** illustrates 17 years of satellite observations (TRMM/LIS), highlighting areas with the highest electrical activity.

Noteworthy studies analyzing fatalities due to lightning strikes in Colombia include publications by (23), (24), and (25). Additionally, works related to risk analysis regarding lightning strikes can be found in (26), (27), (28), and (29).

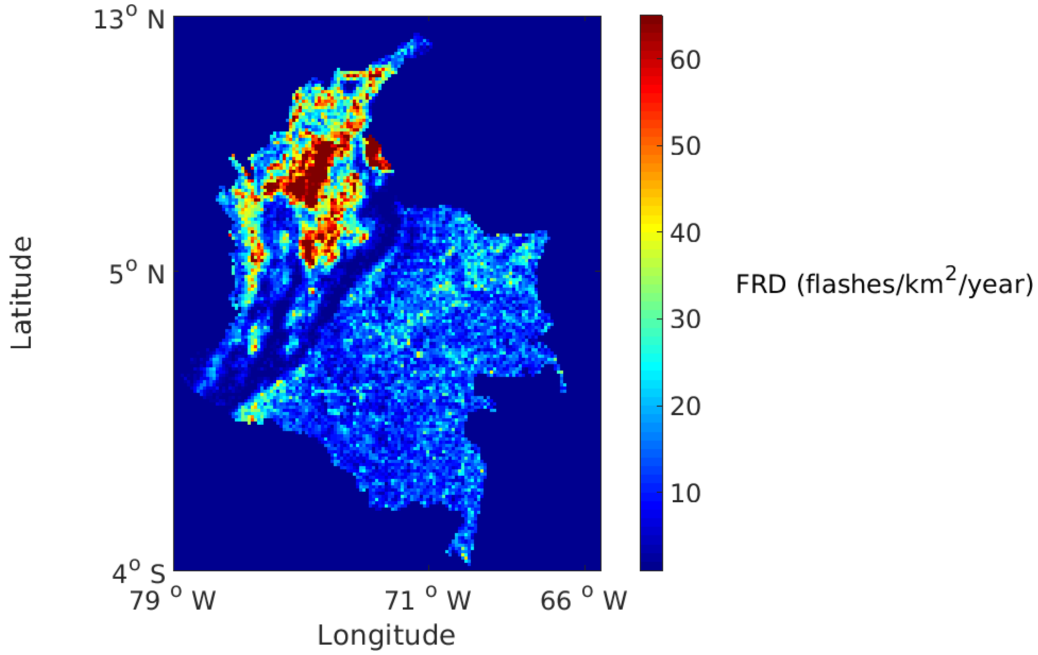

Figure 1. 17 years of satellite observations of lightning over Colombia from TRMM/LIS.
Adapted from: (20)

2. Methodology

The lightning location data used in this study were recorded by Vaisala's GLD360 network, which provided the authors with a database containing approximately 80 million records from the central region of Colombia, as observed from January 1, 2016, to December 31, 2020. These data correspond to a circular area with a radius of approximately 500 km centered on Bogotá, covering about 700 000 square kilometers of Colombian territory. In Vaisala's GLD360 network, each in-cloud or cloud-to-ground stroke is counted as one lightning event. However, confusion can arise due to the terminology used in recording lightning data. As noted by (30, p. 2): "GLD360 does not classify events between CG strokes and IC pulses; all events are labeled CG strokes".

The GLD360 network provides lightning data with a detection efficiency of approximately 80 %, and a median location accuracy between 1.5 and 2.5 km, depending on various landscape factors. The dataset contains nearly 80 million tuples, each recording the date, time, latitude, longitude, and peak current, with a sign indicating the estimated discharge polarity. Additional details of the dataset are summarized in Table I.

Table I. Dataset description

Feature	Description
Resource type	dataset
Temporal range start	2016-01-01
Temporal range end	2020-12-31
Bounding box north lat.	8.3
Bounding box south lat.	1.1
Bounding box west long.	70.5
Bounding box east long.	77.7
Resource format	ASCII
Asset size	4100 MB
Legal constraints	These data are restricted by a user agreement

The methodology for determining lightning incidence patterns in Fusagasugá consisted of two stages, each focusing on different but complementary aspects of data analysis. In the first stage, Power BI was used to pre-process the database, cleaning and filtering the information relevant to the municipality of Fusagasugá and eliminating duplicate or irrelevant records. Subsequently, geographic data transformation was carried out using ArcGIS, which offers advanced tools for spatial analysis and geographic information management.

In the second stage, the event occurrence rates in Fusagasugá from 2016 to 2020 were analyzed to identify temporal and geographic patterns. For the temporal analysis, the annual behavior of lightning activity from 2016 to 2020 was examined, using different time scales to determine monthly, daily, and hourly patterns. Geographically, the stroke occurrence was analyzed by rural districts (*veredas*), which allowed identifying the distribution of the atmospheric electrical activity within the municipal area.

The data analysis utilized the Tableau tool, given its usability, compatibility with web development, ease of integration with various data sources, and ability to create interactive visualizations. With this tool, three dashboards were developed: *Stroke occurrence rates in Fusagasugá 2016-2020*, *Frequency of strokes throughout the day in Fusagasugá*, and *Intensity of strokes per rural district and year*. Each dashboard presents the requested information, offering simple interaction with the presented elements.

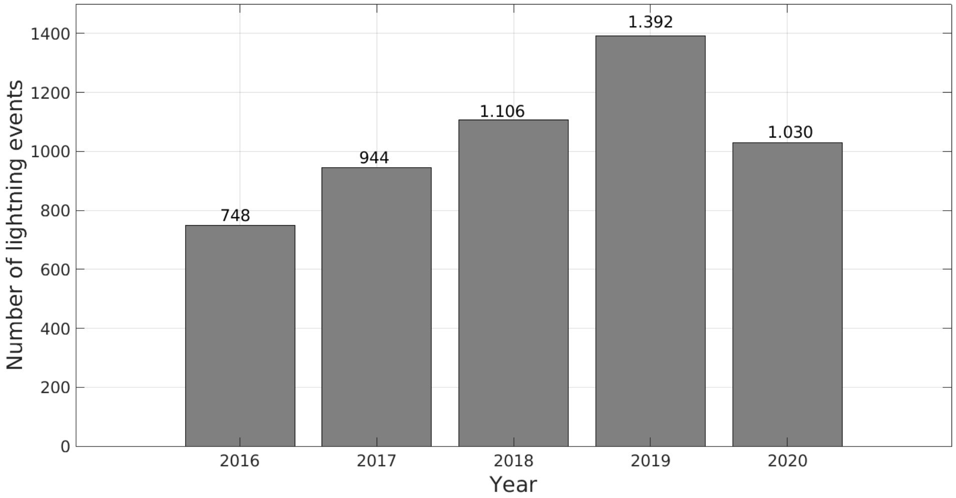

Figure 2. Five years of ground-based lightning observations for Fusagasugá, Cundinamarca, Colombia

Furthermore, a web version of the development was created, accessible through the following link: `https://rayos-pi.vercel.app/`. This web version offers an interactive experience for users to explore the results.

3. Results

Fig. 2 illustrates the total number of lightning strokes recorded in Fusagasugá from January 1, 2016, to December 31, 2020. Over these 1827 days, 5220 strokes were recorded within the municipality's territory. The graph depicts an apparent annual increase in lightning events, with a 26 % increase from 2016 to 2017, a 17 % increase from 2017 to 2018, and a 25 % surge from 2018 to 2019. However, this upward trend is interrupted by a 26 % reduction from 2019 to 2020.

The year 2020 exhibited a lower annual lightning activity but reported peak activity in the first half of the year, much higher than that observed in the previous four years (Fig. 2). Although this study does not examine the relationship between lightning activity and other meteorological phenomena, the decrease in activity observed in 2020 may be related to the weakening of the final phase of the La Niña phenomenon experienced between 2020 and 2021 (16).

With the available data, we can estimate the density of lightning events per square kilometer per year ($events/km^2/year$) in the municipality. Considering Fusagasugá's area of approximately $204\ km^2$, the average is $5{,}1\ events/km^2/year$, a value significantly lower than the departmental average of $22\ events/km^2/year$ and the national average of $30\ events/km^2/year$. It is important to note that the data provided by lightning location systems (LLS) have a detection efficiency (DE) lower than 100 %, implying that some strokes, especially weaker ones, are not detected. Therefore, these results should be seen as indicative of lightning activity rather than as a precise measurement.

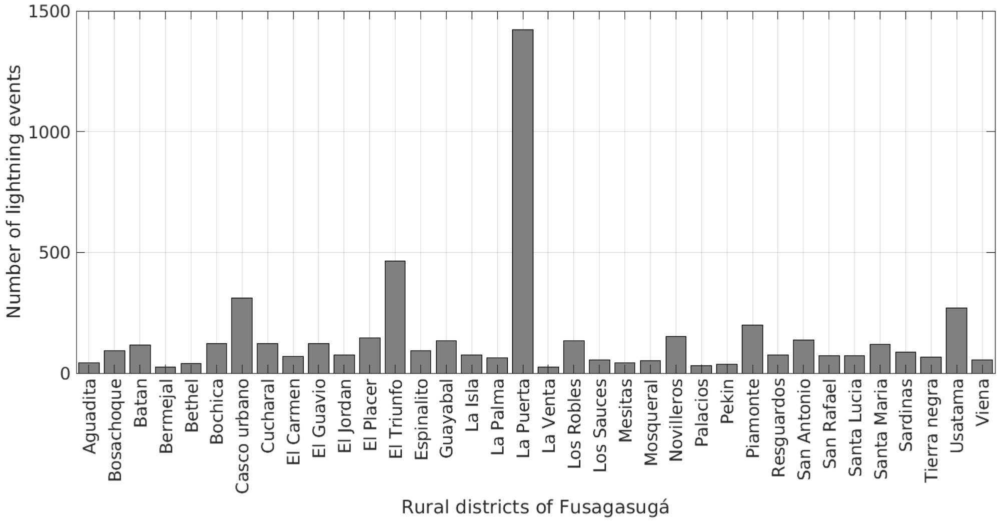

Figure 3. Lightning events in Fusagasugá, ordered by rural district

Fusagasugá exhibits diverse topography and altitude, with approximately 21 % of its territory being flat, 37 % undulating, and 42 % mountainous, ranging from 500 to 3000 meters above sea level. The data were segmented by rural district using developed software, aiming to determine the distribution of lightning activity within the municipality (Fig. 3). Notably, lightning activity is predominantly concentrated in the rural district of La Puerta, characterized by a low population density and an average altitude of 1000 meters above sea level. This area encompasses the populated center of Chinauta, situated on a flat land extension between the Cuja River canyon and the Chocho River canyon. El Triunfo, the second rural district with the highest activity, shares a border with La Puerta and has a lower altitude, spanning between Alto de Canecas and Boquerón, bordering the municipalities of Pandi and Icononzo in the department of Tolima. Together, these two rural districts contribute to over 36 % of municipality's lightning activity while covering less than 25 % of the territory.

Due to the lack of official information on the rural districts' extensions, data from the *corregimientos* (*i.e.*, townships) were utilized. *Corregimientos* are larger rural divisions comprising several rural districts. Fusagasugá is divided into five administrative divisions: North (seven rural districts), East (six rural districts), West (six rural districts), Southwest (six rural districts), and Southeast (ten rural districts), along with the urban center. Lightning event densities were calculated using the territorial extension of each *corregimiento*, and the available lightning event data per rural district. The northern administrative division showed a density of 3.9 $events/km^2/year$, the eastern reported 3.7 $events/km^2/year$, the western exhibited 4.6 $events/km^2/year$, and the southeastern indicated 2.9 $events/km^2/year$. Remarkably, the southeastern region exhibited the highest activity density (9.4 $events/km^2/year$), significantly surpassing the averages of the municipality and the other administrative divisions, highlighting the need for special attention from risk management entities in this area.

Fig. 4 details the occurrence of lightning events in Fusagasugá, providing insight into the months with the highest activity in the municipality. By plotting data from the five-year observation period, it becomes apparent that lightning activity in Fusagasugá follows a bimodal pattern, characterized by peaks in two distinct periods: one in the first semester (March) and another in the second semester (October-November). This bimodal behavior arises from the pronounced transition between these two activity peaks, aligning with the typically drier season in the middle of the year, when lightning activity decreases.

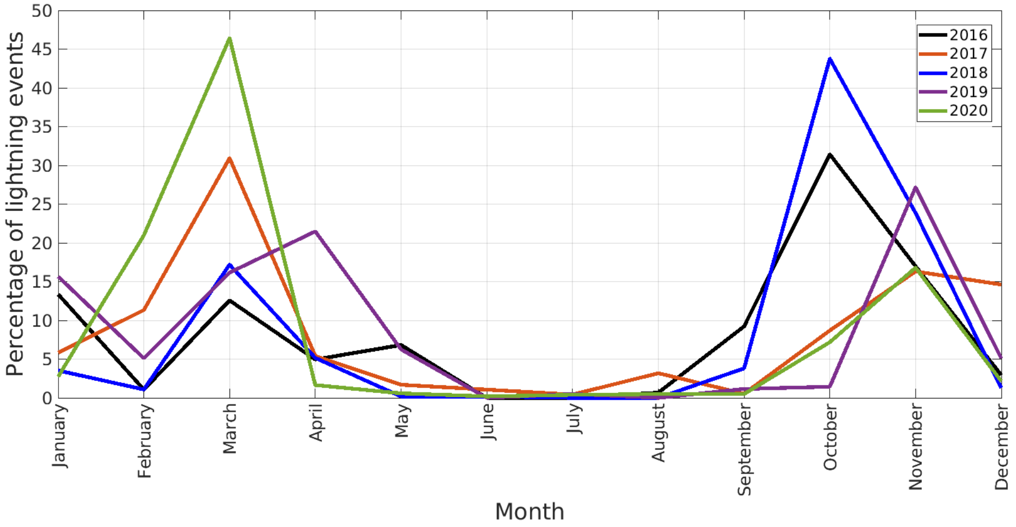

Figure 4. Monthly pattern of occurrence for lightning activity in Fusagasugá

In the observed years, 2017 and 2020 exhibited more intense lightning activity in the first semester, whereas the other three years showed higher activity in the second semester (2016, 2018, and 2019). This variance may be attributed to the prevailing rainfall patterns during those periods.

To determine the timing of lightning occurrences in Fusagasugá, five years of data were filtered and plotted by hour. As depicted in Fig. 5, the activity remains minimal during the morning hours and until noon. Subsequently, there is a gradual increase, with two peaks observed around 17:00 and 01:00 (local time, GMT+5).

When consolidating the results on monthly and hourly lightning occurrences in Fusagasugá, it becomes feasible to plan outdoor activities with reduced risk, considering the minimal likelihood of lightning during the morning hours in the middle of the year. Conversely, heightened activity is observed during the afternoon hours in March, October, and November. Nevertheless, it is essential to note that validating this preliminary conclusion requires extending the observation period to encompass additional years, aiming to confirm the identified patterns.

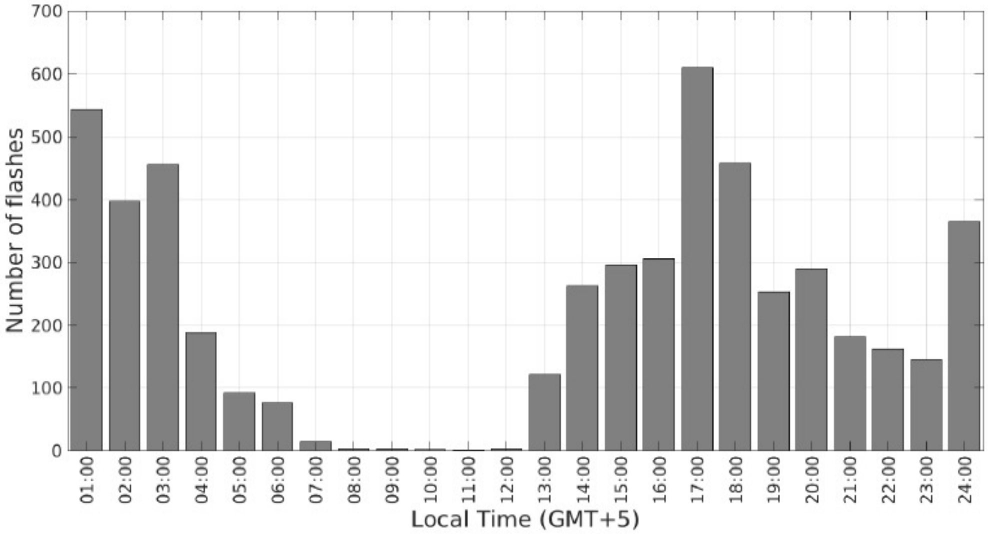

Figure 5. Hourly pattern occurrence for lightning activity in Fusagasugá

4. Discussion

Both lightning events and flash densities are generally estimated for larger areas, often at the country level or beyond. Examples of this approach can be found in works like (14) in Sri Lanka, (18) in Australia, (6) in the Congo River basin, and (15) in Southern Africa. The problem with this method is that it provides mean values that may not accurately represent the entire region, as these areas are not necessarily uniform in terms of topography, vegetation, and other factors.

To illustrate this point, Vaisala's data can be used, noting that their networks account for total lightning, including both in-cloud and cloud-to-ground strokes. Vaisala uses the term *event* to count total lightning. According to their data, Colombia has an average value of 30 $events/year/km^2$. While this confirms a high lightning intensity in the country, it overestimates activity in regions like Orinoquía and the Amazon, where the lightning event densities are below 20 $events/year/km^2$. In contrast, the Momposina Depression can have values above 100 $events/year/km^2$. This discrepancy highlights the problem of using average values to describe lightning intensity over large areas, as it can mask the actual behavior, leading to underestimation in some regions and overestimation in others.

For example, the average number of lightning events for the entire territory of Fusagasugá is low when compared to the departmental and national averages. However, when analyzing occurrences in rural districts, it becomes clear that a municipality's small area experiences high lightning activity. Relying solely on municipal average activity would overlook the local population and infrastructure, as they would not be considered at high risk of lightning impact. The results of this research highlight the importance of lightning climatology studies on smaller scales.

Studies on lightning climatology focused on small areas aid in developing accurate local risk maps. These maps are essential for first responders to focus on protecting, mitigating, or preparing inhabitants and infrastructure for the threat of lightning impacts in specifically identified areas.

Finally, it is important to highlight two features of the lightning data provided by LLS. Firstly, their detection efficiency is less than 100 %, meaning that these data cannot be considered a complete representation of the phenomenon, but rather a representative sample. The second feature is that LLS lightning data heavily rely on wave propagation conditions, which are influenced by the terrain, vegetation, and structures along the path. Therefore, accurately determining lightning locations in very small areas has limitations due to the inherent uncertainty of the measuring system.

5. Conclusions

This article presents the findings from a data analysis of Vaisala's GLD360 lightning detection network for Fusagasugá, Cundinamarca. To facilitate the processing and interpretation of lightning data, the Knowledge Discovery in Databases (KDD) methodology was used in conjunction with Tableau for data visualization .

The lightning activity demonstrates an apparent annual increase over the observed five-year period. However, because of the limited observation window, generalizing this trend is not feasible. In Fusagasugá, lightning activity exhibits a bimodal pattern, peaking in March and October, with a noticeable transition between them and a minimum occurrence in June and July. Most of the activity starts after noon, reaching its peak around 17:00 hours (GMT+5) and extending with reduced intensity into the early morning.

Approximately 36 % of the lightning activity concentrates in just two rural areas, covering less than 25 % of the total municipal area and situated between 500 and 1000 meters above sea level. This highlights the importance of focusing on these areas for risk management and prevention regarding the hazards to the local population and infrastructure that are produced by atmospheric electrical discharges.

Accessing data through Tableau streamlines the visualization and interpretation of results, potentially benefiting the first respondents involved in risk management and regional planning. Despite the relevance of the findings, the authors advocate for expanding the observation window to encompass more annual series, to validate the identified patterns over time.

Data on lightning locations are crucial for local authorities tasked with risk management, highlighting the necessity for similar analyses in other regions. Typically, this information is presented as average values for broader areas, which could result in ineffective efforts and resource allocation by authorities aiming to mitigate the risks associated with lightning activity to people and infrastructure.

Averaging values of lightning activity across larger regions can obscure high-intensity activity in smaller zones, such as rural districts. This is likely a widespread issue, given the uneven landscape in most of the country, especially in the Andean region.

6. CRediT author statement

Díaz-Ortiz conceived the idea and conducted the review and editing processes. *Perilla* and *Ospina* processed the data, developed the software, performed the visualization, and drafted the original manuscript. *Cifuentes* administered the project and provided critical feedback.

References

[1] J. R. Dwyer and M. a. Uman, "The physics of lightning," *Phys. Rep.*, vol. 534, no. 4, pp. 147–241, 2013. http://linkinghub.elsevier.com/retrieve/pii/S037015731300375X

[2] J. Inampués, D. Aranguren, A. Cruz, J. Gonzalez, H. Torres, and H. D. Betz, "Severe thunderstorms in the colombia and venezuela high lightning active areas," *2017 Int. Symp. Lightning Protection*, pp. 359–364, 2017. http://dx.doi.org/10.1109/SIPDA.2017.8116952

[3] V. B. S. Silva and V. E. Kousky, "The south american monsoon system: Climatology and variability," in *Modern Climatology*, S.-Y. S. Wang and R. R. Gillies, Eds. Rijeka: IntechOpen, 2012, ch. 5. https://doi.org/10.5772/38565

[4] I. Hoyos, F. Dominguez, J. Cañón-Barriga, J. A. Martínez, R. Nieto, L. Gimeno, and P. A. Dirmeyer, "Moisture origin and transport processes in colombia, northern south america," *Climate Dyn.*, vol. 50, no. 3, pp. 971–990, 2018. http://dx.doi.org/10.1007/s00382-017-3653-6

[5] D. Aranguren, J. López, J. Inampués, H. Torres, and H. D. Betz, "Cloud-to-ground lightning activity in colombia and the influence of topography," *J. Atmos. Sol.-Terr. Phys.*, vol. 154, pp. 1850–1855, 2014. http://dx.doi.org/10.1016/j.jastp.2016.08.010

[6] S. Soula, J. K. Kasereka, J. F. Georgis, and C. Barthe, "Lightning climatology in the congo basin," *Atmos. Res.*, vol. 178-179, pp. 304–319, 2016. https://doi.org/10.1016/j.atmosres.2016.04.006

[7] R. Albrecht, S. Goodman, D. Buechler, R. Blakeslee, and H. Christian, "LIS 0.1 degree very high resolution gridded lightning climatology data collection." 2016. http://dx.doi.org/10.5067/LIS/LIS/DATA306

[8] D. Aranguren, J. Lopez, J. Montanyà, and H. Torres, "Natural observatories for lightning research in colombia," in *2018 Int. Conf. Electromagn. Adv. Appl. (ICEAA)*, 2018, pp. 279–283. http://dx.doi.org/10.1109/ICEAA.2018.8520371

[9] R. E. Bürgesser, M. G. Nicora, and E. E. Ávila, "Characterization of the lightning activity of relámpago del catatumbo"," *J. Atmos. Sol.-Terr. Phys.*, vol. 77, pp. 241–247, 2012. http://dx.doi.org/10.1016/j.jastp.2012.01.013

[10] D. J. Cecil, D. E. Buechler, and R. J. Blakeslee, “Gridded lightning climatology from TRMM-LIS and OTD: Dataset description,” *Atmos. Res.*, vol. 135-136, pp. 404–414, 2014. http://dx.doi.org/10.1016/j.atmosres.2012.06.028

[11] J. Herrera, C. Younes, and L. Porras, “Cloud-to-ground lightning activity in colombia: A 14-year study using lightning location system data,” *Atmos. Res.*, vol. 203, pp. 164–174, 2018. https://doi.org/10.1016/j.atmosres.2017.12.009

[12] L. D. Tarabukina and V. I. Kozlov, “Climatology of lightning activity in northern asia in 2009-2016,” in *23rd Int. Symp. Atmos. Ocean Opt. Atmospherics Phys.*, 2017, pp. 1–7. http://dx.doi.org/10.1117/12.2287579

[13] D. Zheng, Y. Zhang, Q. Meng, L. Chen, and J. Dan, “Climatology of lightning activity in south china and its relationships to precipitation and convective available potential energy,” *Adv. Atmos. Sci.*, vol. 33, no. 3, pp. 365–376, 2016. http://dx.doi.org/10.1007/s00376-015-5124-5

[14] U. Sonnadara, W. Jayawardena, and M. Fernando, “Climatology of lightning flash activities over sri lanka,” *Theor. Appl. Climatol.*, 2018. http://dx.doi.org/10.1007/s00704-019-02808-w

[15] S. Sen Roy and R. C. Balling, “Spatial patterns of diurnal lightning activity in southern africa during austral summer,” *Atmos. Res.*, vol. 145-146, pp. 182–188, 2014. http://dx.doi.org/10.1016/j.atmosres.2014.03.026

[16] M. Taszarek, B. Czernecki, and A. Kozio{\textbackslash}l, “A cloud-to-ground lightning climatology for poland,” *Monthly Weather Rev.*, vol. 143, no. 11, pp. 4285–4304, 2015. https://doi.org/10.1175/MWR-D-15-0206.1

[17] E. T. Ongee, M. M. Rahman, Y. Yamane, A. Dewan, and R. Mahmood, “Spatial and temporal analysis of a 17-year lightning climatology over bangladesh with LIS data,” *Theor. Appl. Climatol.*, vol. 134, no. 1, pp. 347–362, 2017. http://dx.doi.org/10.1007/s00704-017-2278-3

[18] Y. Kuleshov, “Thunderstorm and lightning climatology of australia,” in *Modern Climatol.*, 2012. http://dx.doi.org/10.5772/35075

[19] H. Torres, E. Perez, C. Younes, D. Aranguren, J. Montaña, and J. Herrera, “Contribution to lightning parameters study based on some american tropical regions observations,” *IEEE J. Sel. Topics Appl. Earth Observ. Remote Sensing*, vol. 8, no. 8, pp. 4086–4093, 2015. http://dx.doi.org/10.1109/JSTARS.2015.2428217

[20] F. Diaz, D. Ortiz, and F. Roman, “Lightning climatology in colombia,” *Theor. Appl. Climatol.*, no. 123456789, 2022. https://doi.org/10.1007/s00704-022-04012-9

[21] J. A. López, J. Montanyà, O. V. Der, D. Romero, D. Aranguren, H. Torres, J. Taborda, J. Martinez, U. Magdalena, and S. Marta, “First data of the colombia lightning mapping array - COLMA,” in *33rd Int. Conf. Lightning Protection*. IEEE Press, Piscataway, NJ, USA, 2016. http://dx.doi.org/10.1109/ICLP.2016.7791436

[22] B. S. A. Murillo, E. A. S. Ríos, and K. A. V. López, “Actividad de rayos en el departamento de santander entre 2014 y 2016,” *Ingenieria*, vol. 26, no. 3, pp. 419–435, 2022. http://dx.doi.org/10.14483/23448393.17585

[23] Cristancho, Jorge, M. Jorge Enrique Rodríguez, G. Carlos Andrés Rivera, and F. Román, "Lightning incident with multiple natives injured in the sierra nevada de santa marta - colombia: Description of scenario," in *2019 Int. Symp. Lightning Protection (XV SIPDA)*, 2019, pp. 1–7. http://dx.doi.org/10.1109/SIPDA47030.2019.8951570

[24] J. A. Barreto, J. S. Fernandez, D. E. Villamil, H. E. Rojas, and F. Santamaria, "Analysis of the certified lightning fatalities and their relation with rainfall in colombia for the period 2008–2018," in *2021 35th Int. Conf. Lightning Protection (ICLP) and XVI Int. Symp. Lightning Protection (SIPDA)*, 2021, pp. 01–06. http://dx.doi.org/10.1109/ICLPandSIPDA54065.2021.9627416

[25] N. Navarrete-Aldana, M. A. Cooper, and R. L. Holle, "Lightning fatalities in colombia from 2000 to 2009," in *2014 Int. Conf. Lightning Protection (ICLP)*, 2014, pp. 40–46. http://dx.doi.org/10.1109/ICLP.2014.6971992

[26] D. E. Villamil, H. E. Rojas, F. Santamaria, R. L. Holle, and W. Brooks, "Analysis of the lightning mortality risk in the provinces of cundinamarca - colombia," in *2022 36th Int. Conf. Lightning Protection (ICLP)*, 2022, pp. 545–548. http://dx.doi.org/10.1109/ICLP56858.2022.9942616

[27] D. E. Villamil, H. E. Rojas, F. Santamaria, and W. Diaz, "Lightning risk and disaster risk management at the beginning of the 2020s," in *2021 35th Int. Conf. Lightning Protection (ICLP) and XVI Int. Symp. Lightning Protection (SIPDA)*, 2021, pp. 01–05. http://dx.doi.org/10.1109/ICLPandSIPDA54065.2021.9627393

[28] O. A. Rodriguez, O. C. Rocha, K. Morcillo, and D. E. Villamil, "Promoting lightning safety inside school articulation programs at the colombian national training service (SENA)," in *2022 36th Int. Conf. Lightning Protection (ICLP)*, 2022, pp. 504–507. http://dx.doi.org/10.1109/ICLP56858.2022.9942577

[29] C. Tovar, D. Aranguren, J. López, J. Inampués, and H. Torres, "Lightning risk assessment and thunderstorm warning systems," in *2014 Int. Conf. Lightning Protection (ICLP)*, 2014, pp. 1870–1874. http://dx.doi.org/10.1109/ICLP.2014.6973434

[30] R. Said and M. Murphy, "GLD360 upgrade: Performance analysis and applications," in *24th Int. Lightning Detection Conf.*, 2016. https://training.weather.gov/wdtd/courses/woc/severe/data-fusion/lightning/gb-ltg-prod/story_content/external_files/Said_Murphy_2016.pdf

Fernando Díaz-Ortiz

PhD in Electrical Engineering, MSc in Electronics Engineering, MSc in Information Sciences, and Bachelor's degree in Electronics Engineering. Currently, he is an assistant professor at Universidad de Cundinamarca. His interests include atmospheric electric discharges and telecommunications.
Email: faugustodiaz@ucundinamarca.edu.co

Juan Pablo Ospina Carrillo

A systems engineer graduated from Universidad de Cundinamarca, he possesses outstanding skills in data analysis. His academic background and professional experience have equipped him with a deep understanding of the techniques and tools necessary to interpret and effectively leverage information. Known for his ability to extract meaningful insights from complex datasets, he adeptly identifies patterns, trends, and relevant opportunities. **Email:** jpospina@ucundinamarca.edu.co

Neyder Alfredo Perilla López

Systems engineer graduated from Universidad de Cundinamarca, possessing great data analysis skills. His academic background and professional experience have equipped him with a profound understanding of techniques and tools required for data interpretation and utilization. Renowned for his capacity to extract valuable insights from intricate datasets, he adeptly identifies patterns, trends, and opportunities.

Email: naperilla@ucundinamarca.edu.co

Pedro Luis Cifuentes Guerrero

An electronics engineer specializing in Software Engineering with a Master's degree in Software Architecture, he currently teaches in the Electronic Engineering program of Universidad de Cundinamarca. His expertise and passion lie in software development applied across diverse domains such as tourism, agriculture, the Internet of Things (IoT), weather stations, and sports sciences. His approach focuses on developing innovative technological solutions to optimize processes and enhance efficiency within these sectors.

Email: pcifuentes@ucundinamarca.edu.co

UNIVERSIDAD DISTRITAL
FRANCISCO JOSÉ DE CALDAS

Ingeniería

https://revistas.udistrital.edu.co/index.php/reving/issue/view/1241

DOI: https://doi.org/10.14483/23448393.21483

Research

Extreme Testing of Guard Cables with Fiber Optics: A Case Study

Pruebas en condiciones extremas de cable de guarda con fibra óptica: un caso de estudio

Erick-Alejandro González-Barbosa[1], Fernando Jurado-Pérez[1], José-Joel González-Barbosa[2] *, and Julio César Méndez Gutierrez [1]

[1]Tecnológico Nacional de México/ITS de Irapuato, México

[2]Instituto Politécnico Nacional, CICATA-Queréretaro, México

Abstract

Context: Optical fiber ground wires (OPGWs) sometimes melt and rupture when exposed to extreme conditions, such as atmospheric discharges, short circuits, and corrosive agents, that affect their electrical and mechanical properties. These conditions depend on the geographical area where the cable is installed, with the most critical being industrial and coastal zones as well as marine and mountainous environments. This research analyzes a cable rupture due to lightning strikes from a coastal zone.
Method: The analysis discusses cable selection criteria based on engineering specifications. It also discusses standardized test methods and procedures. The tests performed are based on visual and dimensional inspections, mechanical stress assessments, and chemical analysis.
Results: The complete analysis allows determining the necessary basis for the characterization and mathematical parameterization of OPGWs, establishing considerations that contribute to proper functioning in order to reduce communication and power supply interruptions.
Conclusions: This study helps to estimate the behavior of the entire structure and the quality of failed OPGWs, providing insights into improving cable design and maintenance practices in harsh environments.

Keywords: OPGW cables, mechanical tests, atmospheric discharges

Article history

Received:
7th/Nov/2023

Modified:
25rd/Jun/2024

Accepted:
6th/Aug/2024

Ing, vol. 29, no. 3, 2024. e21483

---

* **Correspondence:** jgonzalezba@ipn.mx

Resumen

Contexto: Los cables de tierra con fibra óptica (OPGW) a veces se derriten y rompen cuando se exponen a condiciones extremas como descargas atmosféricas, cortocircuitos y agentes corrosivos, lo que afecta sus propiedades eléctricas y mecánicas. Dichas condiciones dependen de la zona geográfica donde se instale el cable; las áreas más críticas son las zonas industriales y costeras, así como los ambientes marinos y montañosos. Esta investigación analiza la ruptura de un cable debido a rayos en una zona costera.

Método: Este análisis discute los criterios de selección de cables basados en especificaciones de ingeniería. También se discuten los métodos y procedimientos de prueba estandarizados. Las pruebas realizadas se basan en inspecciones visuales y dimensionales, pruebas de esfuerzo mecánico y análisis químico.

Resultados: El análisis completo permite obtener las bases necesarias para la caracterización y parametrización matemática de los OPGW, estableciendo consideraciones que contribuyen al correcto funcionamiento para reducir las interrupciones de comunicación y suministro eléctrico.

Conclusiones: Este estudio ayuda a estimar el comportamiento de toda la estructura y la calidad de OPGW fallidos, proporcionando información para mejorar el diseño y las prácticas de mantenimiento de los cables en entornos adversos.

Palabras clave: cables OPGW, pruebas mecánicas, descargas atmosféricas

Table of contents

1. Introduction

Composite fiber optic ground wires protect transmission lines from atmospheric discharge or lightning strikes, as they can lead to the interruption of the energy supply. During the last decade, the influence of atmospheric discharges on OPGW cables has been observed, noting considerable damages, ranging from the rupture of exposed cables to compromised mechanical resistance (Fig. 1). Optical fiber ground wires (OPGW) are designed to carry out two functions: the protection of power transmission lines from atmospheric discharges and data transmission via integrated fiber optics. OPGWs have gained considerable importance worldwide due to their double function, *i.e.*, protection and communication. Thereupon, to ensure their capacity, electro-mechanical test methods focusing on reproducing extreme operating conditions have been developed.

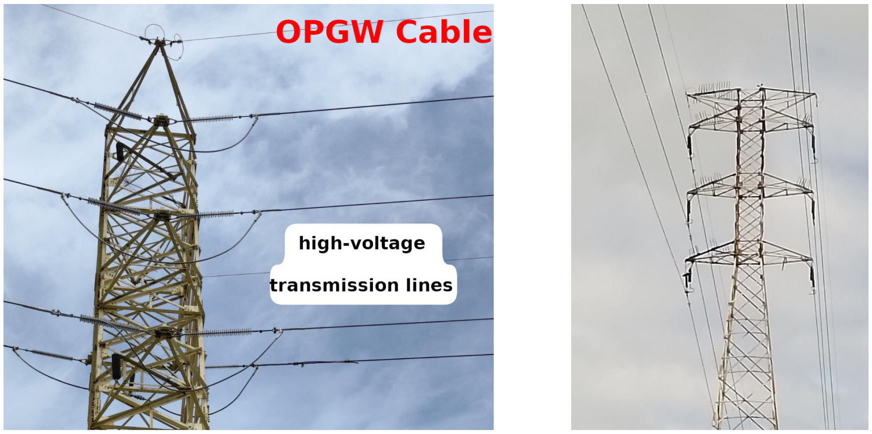

Figure 1. This figure depicts a tower with an OPGW. The tower stands tall as a structural support for the OPGW and is designed to provide grounding and communication capabilities. This cable typically includes optical fibers for high-speed data transmission, and it is integrated with a metal sheath for grounding purposes, thereby ensuring the power transmission network's structural stability and functional efficiency

(1) simulated lightning strikes on OPGWs through an anode and a negative electrode that generated electrical impulses (discharges) between 100 and 200 Coulomb for 200 ms. The temperature distribution along the cable was monitored while considering heat release at the lightning strike's position and using a distributed fiber optic temperature sensor (DOFTS). For the inner part of the OPGW, the temperature increase captured by the DOFTS was only several degrees Celsius. These experimental results also showed that the use of DOFTS has great potential for maintaining transmission lines, and that the transmission of electrical energy is not affected when lightning impacts generate less than 100 Coulomb. A similar project was carried out by (2), who proposed the use of DOFTS for better cable monitoring and maintenance, aiming to avoid potential risks leading to power outages or shortened operating times. Similar works have analyzed heat transfer and melting, as well as the breaking of wires in OPGWs (3). This has been done through direct current (DC) arc tests simulating lightning strikes to analyze melting and characterize the breakage of the wire strands. Said characterization involves the fusion of threads and the distribution of heat the transferred per area by an induced current arc of 1-100 kA. For these tests, the variables considered include current, duration (time), polarity, and gap length, in addition to size, type, and number of threads for cable selection.

Furthermore, (4) performed a mathematical analysis that predicted the melting and failure of wires in the face of lightning discharges simulated via 0.1-100 kA DC arcs, and (5) validated these conditions through various tests and mathematical thermal behavior models.

The work by (6) presented a comprehensive analysis based on the simulation of events with harmful effects such as electric shocks, short circuits, and wind-related incidents. Mathematical models, simulations, and thermomechanical sensors (DTS) placed along the OPGW fibers were used to determine their behavior. The cables were exposed to environmental factors such as wind, rain, humidity, and snow, as well as to the cooling/heating effects of short circuits and instantaneous current increases in the conductor phase – when OPGWs are exposed to these conditions, gradual insulation deformations take place.

In (7), the authors studied the experimental and numerical responses of the TF1000 under different wind loads. Moreover, (2) stated that cables suffer deterioration in frozen areas due to constant layers of ice, with deformations appearing when the additional tension is higher than 30 kN, potentially leading to fiber breakage. In (8), the effects of melting ice on the structure of a commercial and a modified OPGW supported by DOFTS were analyzed, examining the characteristics of the temperature distribution and variation due to the melting of ice on both OPGW cables.

The research presented in (9) proposed a comprehensive performance evaluation structure for transmission towers in power line systems. The authors considered the wind as the main factor of analysis, incorporating its speed and direction as well as the orientation of the lines. They proposed an optimal arrangement and used 50 years' worth of statistical data on the wind in the area. With the OPGW grounded at each tower, the probability of lightning strikes and losses increased. Moreover, (10) suggested the use of these cables as lightning rods for power transmission lines, since lightning strikes are unavoidable and often cause cable unraveling or breakage. These accidents are serious threats to the transmission of information. The research confirmed that the high temperature of the electric arc and the effects of thunder are the main reasons for power line breakage.

One of the main disturbances in this type of cable is the fraying of steel, generally associated with the presence and impact of atmospheric discharges that affect the wire, which is common in transmission lines located in critical areas (11). The work by (4) concluded that some metallic wires in power line ground cables (GW) and OPGWs sometimes melt and break from high-energy lightning strikes. The damage exhibits high concentrations of energy located at specific points of the wire, capable of melting and detaching cable strands (Fig. 2a). The effects caused by corrosion were also considered, as derived from the material used in the structure, which degrades due to inclement weather. In some cases, there were incrustations by the effects of load, in addition to corrosion, with the melting and loss of material observed in fault zones.

a) b) A discharge c) Several continuous discharges

Figure 2. a) OPGW cable affected by an atmospheric discharge (Federal Electricity Commission) and guard cable with CFE optical fibers E1000-21. b) and c) Experimental results of controlled electrical discharges in the laboratory (11)

Fig. 2 shows the conditions potentially generated by atmospheric discharge in the cable, which involve high energy in short periods of time, or *vice versa*. It has been determined that the first case is associated with atmospheric discharges and the second with short-circuit conditions. The authors of (11) suggested that the damage increases linearly with the increase in charge transfer. As the discharge area increases, the intensity of the arc charge decreases. However, the volume of damage undergoes a non-monotonous change, which is due to complex variations in the area of attachment of the arc, regulated by the discharge space and the intensity of the current.

According to the Federal Electricity Commission, there were more than 967 failure events in the studied cable type in 2022 in Mexico (12). Attenuation was considered to be the main cause of failure. Specifically, 381 failure events related to attenuation were reported, as well as 51 to splice boxes, 189 to fiber optic cuts, and two to hardware. Failure by attenuation implies that optical fibers can no longer transmit data, with efforts, extreme temperatures, and external conditions being the main causes. Junction box failure occurs when wires are poorly tied. Fiber optic cuts are due to the different types of sudden events to which cables are exposed, and hardware failure primarily occurs when fastening in the towers does not coincide with the dimensions of the installed cable (13).

After reviewing the background on OPGWs and failure drivers, we will discuss some conditions to promote the development of procedures for the supervision, evaluation, and analysis of this cable type. The studied wires were exposed to atmospheric discharges causing their forced exit from transmission lines. Thereupon, one of the priorities was to know the effect of discharges on the electrical shielding of OPGWs in transmission towers at the national level. Regarding this specific case, we describe the methodology for analyzing a failed wire in one of the critical areas of the Republic of Mexico. The objective of this study is to investigate the performance and failure mechanisms of OPGWs under extreme environmental and mechanical conditions leading to rupture. By conducting comprehensive visual inspections, dimensional assessments, mechanical stress tests, and chemical analyses, this research aims to identify critical factors that contribute to the degradation and ultimate failure of OPGWs. The findings will provide valuable insights into improving design, material selection, and maintenance practices to enhance the durability and reliability of OPGWs in harsh operating environments.

2. Methodology

The proposed methodology also makes it possible to accurately assess the effects on the failed cable both at the location of the fault and close to it. The tests involved allow determining the causes of the damage and proposing precautionary measures. The case study includes a sample of a guard cable with an integrated fiber optic wire subdivided into two sections after the failure (Fig. 3a). Both sections are linked to failure by cable fraying, as observed in the fractured wires.

There are several tests for this type of cable, both before commissioning and after failure. The methodology described herein includes the main tests stipulated in the regulations applied to OPGWs after failure:

→ *Visual inspection* is carried out at the macro and micro levels. In both sections of the wires, observation and detailed analysis of the fault zones are performed, for which a microscope is used as an adjunct. From this inspection, the type of failure (ductile or brittle), the incrustation of external agents, the level corrosion, and the material loss are obtained.

→ *Dimensional inspection* is a necessary technical test to ensure the quality and dimensional conditions under which the cable operates. This inspection records the current diameter of each wire, thereby obtaining melting and material loss values. Dimensions are measured using a Vernier caliper or a micrometer.

→ *Mechanical stress*. Mechanical tension is measured using a tension testing machine applied to each of the failed wires. It is defined as the mechanical behavior based on the effort against breaking times. Fitting the stress *vs.* time curve allows predicting the cable's fatigue life, *i.e.*, the number of cycles it can withstand before failure. It also helps to understand the cable's elastic and plastic deformation behaviors over time. Sudden increases in stress or deviations from expected patterns can indicate potential failure points or areas that require maintenance. This test also allows understanding creep behavior and ensures that the cable maintains its integrity and performance over its expected service life. In critical applications, continuous monitoring of stress over time provides real-time data on cables' structural health, enabling timely decisions to prevent failures.

→ *Chemical analysis* is used to identify the characteristics of the scale and corrosive elements in the cable. Scattered X-ray energy is used to this effect.

The analysis presented herein is based on 12 aluminum alloy wires surrounding the core of an OPGW cable, an element indicated as (7) in Fig. 3b. These aluminum alloy wires are made of 1350 aluminum-coated steel and support the OPGW's cable structure. The samples were tested according to regulations and were 0.30 m long. The failed OPGW was a 36-fiber cable with a diameter of 16 mm and an energy transfer capacity of 50 Coulomb (C). Details are shown in Fig. 3b.

(a) **(b)**

Figure 3. 36-wire OPGW. (a) Analyzed samples, sections A and B. (b) Guard cable with OPGW optical fibers, 36 single-mode fibers of class 0 for atmospheric discharge, category A for thermal dissipation. (1) Dielectric central element. (2) Thread to block water penetration. (3) Single-mode optical fibers. (4) Three thermoplastic tubes filled against water, each with 12 fibers. (5) Threads for blocking water penetration. (6) Aluminum tube. (7) 12 aluminum-coated steel wires, $\varnothing$=2.92 mm

3. Results

As per regulations and standards, mechanical, optimal performance, and inspection tests are necessary to validate the quality and/or conditions of OPGWs. In this work, the physical, mechanical, and electrical characteristics of the individual wires in the cable samples were determined according to the specifications of the ASTM B230 (14) and ASTM B232 (15) standards. This specification covers the standard requirements for aluminum-alloy round wires for electrical purposes. Aluminum-alloy wires must be made from drawing stock and be free of brittleness, as evidenced by their ability to be coiled or looped around their diameter with or without a mandrel, as per the ASTM B232 standard. The tests described herein were selected according to their relevance in evaluating the studied cable type. As previously described, these standardized and regulated tests were based on visual inspection, dimensional inspection, mechanical stress assessment, and chemical analysis.

3.1. Visual inspection

Visual inspection was carried out at the macro and micro levels with the help of a microscope.

Gross observation:

Section A comprises steel wires clad with aluminum, with deposits of corrosive agents exhibiting whitish and brown colorations due to the oxidation of the localized base material. In addition to the loss of material on the wire surface, the OPGW's 12 crown wires show melting of the material and loss of coating from the point of failure up to distances of 0.40 m. A visual inspection was carried out before cutting the 0.30 m sections for the tension test. The ends of the wires showed a reduced cross-section in the failure zone, and 11 out of the 12 wires had sharp tips due to the loss of material and the type of failure. Moreover, the aluminum tube where the optical fibers were located exhibited a transverse reduction in the affected area. Fig. 4 shows the steel wires with aluminum coating in the crown, which exhibit wear and melting of the base material as well as sharp points. For section A, the aluminum tube containing the fibers showed a reduced diameter in the affected area – the reader should recall that this section includes three filaments with 12 optical fibers each (Figs. 5c and 5d). As observed in a close-up of the OPGW, there are fractures in some of the wires in the fault zones, mostly ductile faults and smelting due to atmospheric discharge, in addition to wires and material detachment in the fault zone, with some elements of oxidation and coating loss (Figs. 5a and 5b). Oxidation is observed in Figs. 5a, 5b, and 5c, as well as pitting of the coating and loss of material. Fig. 5d shows the failed core tubing, which contains the optical fibers, in addition to a reduced cross-section due to mechanical stress. In the failed OPGW, clear signs of warming, short circuits, and cross-section reduction are also observed.

Section B of the failed sample indicates the loss of the aluminum-coated crown, which may be due to material melting. The tips of the wires have a reduced cross-section in the failure zone, and 10 of them have sharp points. One of the wires does not exhibit loss of area in it is cross-section due to brittle fault, and one more suggests a tool cut.

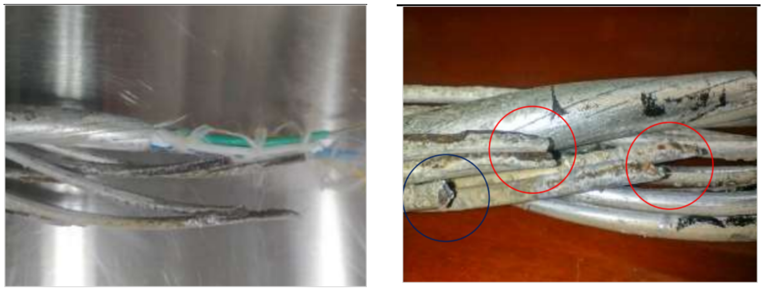

Figure 4. Left: failed section; right: fracture and material melting zone. Marked in red, sharp points can be observed

(a) (b) (c) (d)

Figure 5. Affected area of the wires: a) oxidation and loss of material, b) loss of aluminum coating, c) oxidation and pitting of the coating as well as material loss, d) core tubing failure due to mechanical stress

Fig. 6 shows the 12 failed OPGW wires. The visual analysis of each wire is summarized below:

- Wire 1 has a reduced cross-section as well as a fragile fracture footprint.
- Wire 2 has a reduced cross-section and whitish deposits.
- Wire 3 has a material release on the tip, and a lack of aluminum coating can be observed.
- Wire 4 exhibits a fragile fracture pattern and temperature-induced material melting.
- Wire 5 has a reduced cross-section and an almost completely melted tip.
- Wire 6 exhibits a reduced cross-sectional area and fragile fault; coating loss is observed.
- Wire 7 shows a reduced cross-section, and the tip shows signs of brittle failure. Signs of aluminum coating loss and temperature melting are also observed.
- The cross-section and fragile footprint of wire 8 were minimally reduced, with minor deformation, but almost all of the aluminum coating was lost.
- Wire 9 exhibits a reduced cross-section, leaving the tip sharp. It shows whitish deposits and signs of material loss due to casting.
- Wire 10 shows a reduced cross-section area and a sharp tip. The observed material loss corresponds to more than 50 % of its section. There is also a lack of coating, and even the loss of much of the base material.

(1) (2) (3) (4) (5) (6) (7) (8) (9) (10) (11) (12)

Figure 6. Failed OPGW crown wires, section B

- Wire 11 exhibits signs of tool cutting.
- Wire 12 shows a minimal reduction of its cross-section area and fragile footprint, with minor deformation, but it shows signs of material detachment caused by high temperatures.

The darker wires suggest the effect of atmospheric discharge and thermal dissipation, as well as loss of coating and adhesion of polluting agents.

Microscopic inspection

Corrosion zones were identified in the steel wires coated with aluminum, as well as embedded deposits of elements unrelated to the composition of the material. We also observed the melting and loss of material in the fault zone due to atmospheric discharge. Figs. 7a, 7b, and 14 show the close-up and microscopic inspection of the OPGW's critical zones.

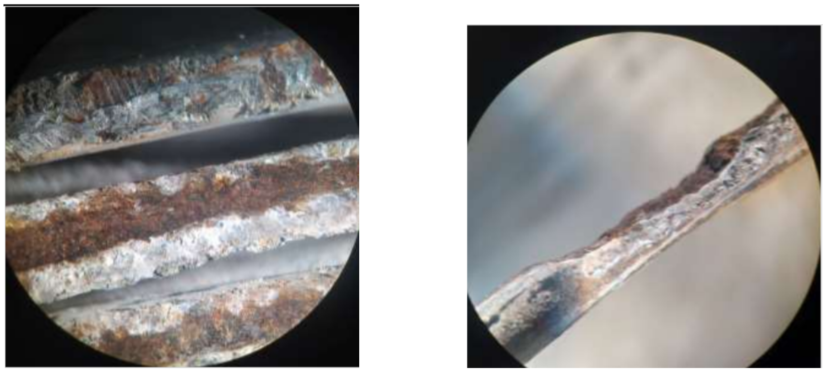

(a) **(b)**

Figure 7. a) Crown wires with wear areas; b) total loss of aluminum layer and oxidation of the steel core

3.2. Dimensional inspection

Table I shows the dimensional inspection data of the crown wires in one of the samples, specifically in the failure zone. The diameter was measured to be nominal on outside and for each of the 12 wires

Table I. Dimensional inspection of the crown wires of the OPGW in the failure zone. The initial diameter corresponds to the cable in good condition. NA: wire core, DC: full cable, and TA: aluminum tubing.

	Initial diameter $[mm]$	Measured diameter $[mm]$	Loss %		Initial diameter $[mm]$	Measured diameter $[mm]$	Loss %
CC	14,54	14.13	2.9	NA 7	2.91	2.54	12.8
NA 1	2.90	2.66	8.3	NA 8	2.90	2.78	4.2
NA 2	2.88	2.57	10.8	NA 9	2.89	2.67	7.7
NA 3	2.90	2.44	15.9	NA 10	2.92	2.70	7.6
NA 4	2.91	2.62	10	NA 11	2.91	2.65	9
NA 5	2.88	2.66	7.7	NA 12	2.90	2.58	11.1
NA 6	2.92	2.61	10.7	TA	8.79	7.25	17.6

in the crown of the OPGW. For some manufacturers in the country, the nominal outer diameter is 14.65 mm, and the nominal weight is 0.575 kg/m. If storage time or conditions are to be considered, mass loss due to the reduction of the cross-section area constitutes a sign of the natural corrosion process. According to the manufacturer's technical data, the average cable corrosion rate over 720 is 0.072 $kg/m^2 \times year$.

Table II shows the dimensions of the cables located in areas close to the rupture in sections A and B. Through the dimensional inspection of each element, diameter loss was observed, highlighting the need to corroborate the operating conditions of the cable in order to evaluate its mechanical behavior and determine its properties.

In addition, the tests conducted in this work allowed noting that the mechanical forces induced by the cable's weight produce permanent deformations, and that temperature variations cause thermal deformations. Salinity, corrosion, and cable galloping also cause this type of deterioration. Although the properties were good in regions close to the failure zone, this deterioration was already noticeable.

3.3. Mechanical stress

Fig. 8 shows two cable sections (class 0, 0.30 m in length, as stipulated by the E1000_21 specification for stress testing). The elastic modulus (E) of the analyzed cable is around 116 Gpa. Table II analyzes the

Figure 8. 0.30 m long OPGW cable for tension tests, aluminum tube containing the optical fibers and their 12 test wires

Table II. Results of the mechanical stress test for sections A and B, exterior crown

Wire number	**Measured diameter** [mm] **A-B**	**Cross section** [mm^2] **A-B**	**Breaking load** [N] **A-B**	**Maximum effort** [MPA] **A-B**	**Failure** **A-B**
1	2.71-2.89	5.768-6.56	6230-7870	1080.08-1199.74	Ductile-Ductile
2	2.84-2.89	6.335-6.20	7810-8190	1232.89-1320.63	
3	2.80-2.78	6.158-6.07	8030-7870	1304.09-1296.56	
4	2.84-2.85	6.335-6.38	7700-8130	1215.52-1274.41	
5	2.82-2.81	6.246-6.20	7980-7570	1272.65-1220.65	
6	2.81-2.80	6.202-6.16	8010-7820	1291.60-1269.99	
7	2.82-2.83	6.246-6.30	7960-7840	1274.45-1246.38	
8	2.82-2.84	6.242-6.33	8070-8020	1292.00-1264.46	
9	2.83-2.85	6.290-6.38	8200-7940	1303.62-1244.63	
10	2.84-2.82	6.235-6.24	7940-7740	1253.41-1239.23	
11	2.80-2.83	6.158-6.30	8200-7940	1331.70-1262.00	
12	2.83-2.82	6.290-6.24	8030-7740	1276.62-1240.38	

results of the mechanical tension tests, where each of the 12 wires was brought to break. On the left side, the results for section A show that the resistance to mechanical stress is maintained, with ductile failure under a very homogeneous load. It was expected that, due to its proximity to the fault, the material would be brittle and exhibit fragile faults as well as very uneven and lower load resistance results. In contrast, excellent cable quality was observed even after failure. The values on the right correspond to section B, and the results are similar.

Among the results obtained in the stress tests, homogeneity was found between samples of sections A and B, with both preserving their mechanical properties and failing under similar values on average. Therefore, the cable was still in good condition before the sudden failure. The mechanical properties of the elements were slightly affected by the failure zone due to heating or specific corrosion. Fig. 12c shows the breaking load distribution in section A and B wires. The average breaking load of section A was $\mu_A = 7846N$, with a standard deviation of $\sigma_A = 528{,}22N$, while, for section B, these values were $\mu_B = 7889N$ and $\sigma_B = 171N$.

The test sequence was carried out using the JAUS universal machine (Fig. 9), applying a constant load at a speed of 5000 N/min. Test runs were performed for each of the wires from sections A and B. Fig. 9b shows one of the OPGW cable wires, which fails upon reaching the limit of its mechanical resistance to tension. The 30 ton JAUS vertical machine was located in a mechanical testing lab, and it had been calibrated by the laboratory of metrology.

Test runs were performed for each of the wires that make up sections A and B. The mechanical stress results show the behavior of some of the outer wires in the OPGW cable crown upon applying a point load at a given time. Fig. 10 shows the load *vs.* time graph for cables 1 and 11 of section A. The graph for section B is presented in Fig. 11. These rupture values can be verified in Table II.

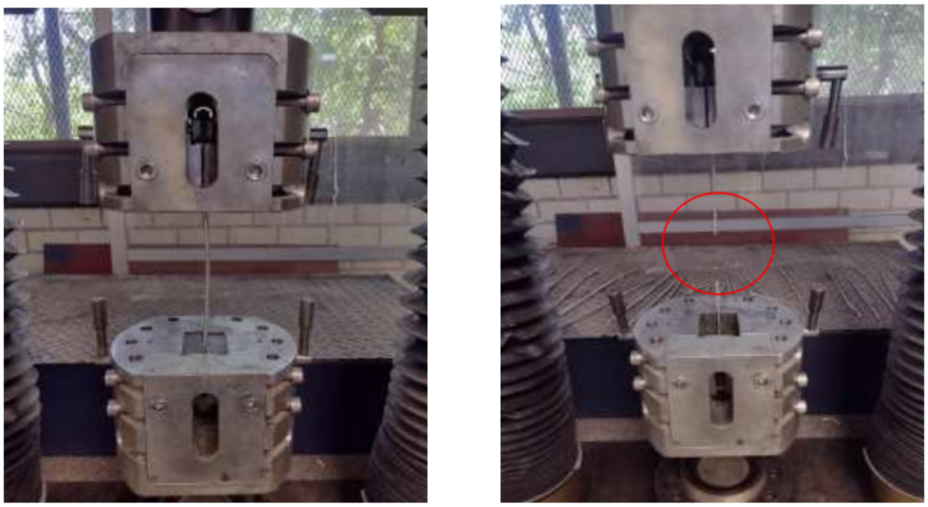

(a) **(b)**

Figure 9. OPGW cable wire tension test: a) universal tension machine at the start of the test; b) end of test upon failure

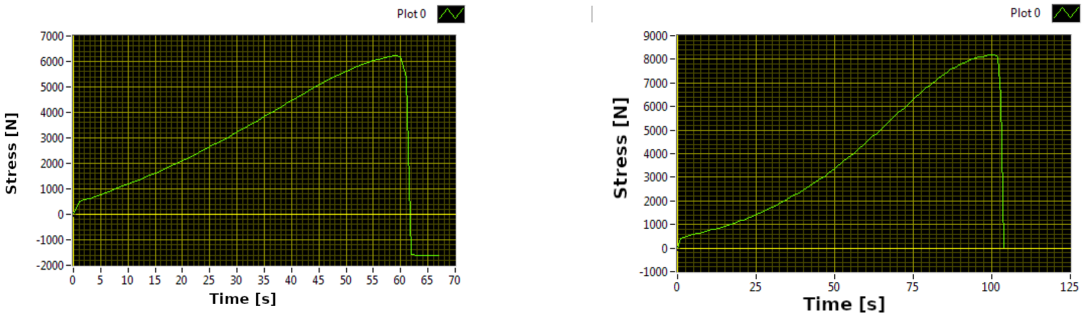

(a) **(b)**

Figure 10. Point load *vs.* time graph for a) wire 1 and b) wire 11 of section A

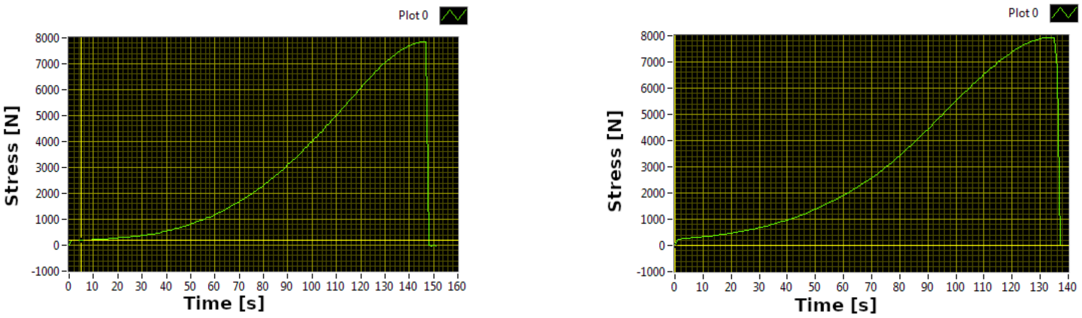

(a) **(b)**

Figure 11. Point load *vs.* time graph for a) wire 1 and b) wire 11 of section B.

The time until failure in most of the wires of sections A and B is close to 120 or 140 s, with some exceptions, such as wire 1 of section A, which failed within 60 s of applying the load according to the established parameters and execution speed. In both sections, a ductile and homogeneous failure behavior was observed, validating the quality of the analyzed cable.

3.3.1. Mechanical characterization

Figs. 12a and 12d present the stress *vs.* time graphs for the 12 cables in sections A and B, respectively. As part of the characterization of the cables' behavior, we tested several polynomials, concluding that the fourth-order one best fitted the data. To determine the polynomial representation of the curves, this work proposes an algorithm that repeatedly computes a polynomial approximation using 12 distinct curves. To this effect, a fourth-order polynomial is generated for each curve. The algorithm then calculates the Euclidean distances from each curve point to the corresponding polynomial. Specifically, the average Euclidean distance for each curve is computed. The polynomial that best represents the set of curves is the one that minimizes said average distance. Ultimately, we used the polynomials within two times the standard deviation of the minimal distance and computed the entire section's polynomial. This corresponds to the best representation of the curves, leaving those that have been physically affected aside. The detailed steps of the algorithm are outlined in 1.

Algorithm 1 Polynomial computation using a set of curves, where $T_{A,B}[N]$ is a polynomial equation for A or B

```
Input: $A_i = \{a_i^1, a_i^2, \dots a_i^j\}$, $B_i = \{a_i^1, b_i^2, \dots b_i^j\}$ or $A \cup B, i = 1 \dots N. N = 12$, 12 wires
Output: $\{T_{A,B}[N] = (c_1, c_2, c_3, c_4, c_5) \mid c_2 * x^3 + c_3 * x^2 + c_4 * x + c_5 = 0\}$
RepresentativeData ← 0
$VD[i = 1, 2, \dots, N] \leftarrow [\infty, \infty \dots \infty]$
for $i \leftarrow 0$ to $N$ do
    Data1 ← $A_i$ or $B_i$
                                                        ▷ compute the fourth-degree polynomial
    $(c_1, c_2, c_3, c_4, c_5) \leftarrow$ polyfit(Data1)
    for $j \leftarrow 0$ to $N$ do
        Data2 ← $A_j$ or $B_j$
                                                        ▷ average distance between the data and the curve
        $dist_j \leftarrow$ distance($(c_1, c_2, c_3, c_4, c_5)$, Data2)
    end for
    if then $\frac{1}{N} \sum_{j=1}^{N} (dist_j) \leq VD[i]$
        $VD[i] \leftarrow \frac{1}{N} \sum_{j=1}^{N} (dist_j)$
        RepresentativeData ← $i$
    end if
end for
$Mean \leftarrow \frac{1}{N} \sum_{i=1}^{N} VD[i]$
                                                        ▷ see Figs. 12b and 12e
SetRepresentative ← $\{i \mid VD[i] \leq \text{mín}(VD[i]) + \frac{2}{N} \times \sum_{i=1}^{N} (VD[i] - Mean)^2\}$
                                                        ▷ see Eqs. (1) and (2) and Fig. 12f
$T_{A,B}[N] = (c_1, c_2, c_3, c_4, c_5) \leftarrow$ polyfit(SetRepresentative)
```

Eqs. (1) and (2) represent the polynomial approximation of stress *vs.* time for sections A and B, respectively. For these equations, we considered the curves shown in Figs. 12b and 12e, which correspond to the *SetRepresentative* variable in Algorithm 1. Fig. 12f shows the polynomial approximation of Eqs. (1) and (2). The behavior of the cables exposed to discharges changes considerably, while those with little exposure maintain a similar behavior.

$$T_A[N] = -8{,}7815^{-5} t^4 + 0{,}0156 t^3 - 0{,}2792 t^2 + 26{,}0504 t + 157{,}9727 \tag{1}$$

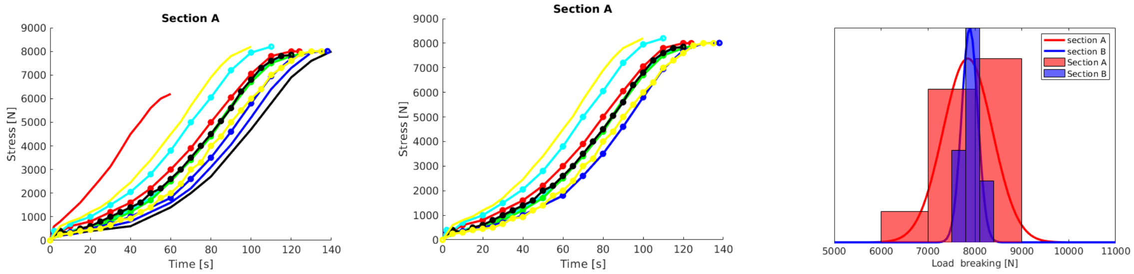

(a) Twelve wires **(b)** Nine wires **(c)** Breaking load

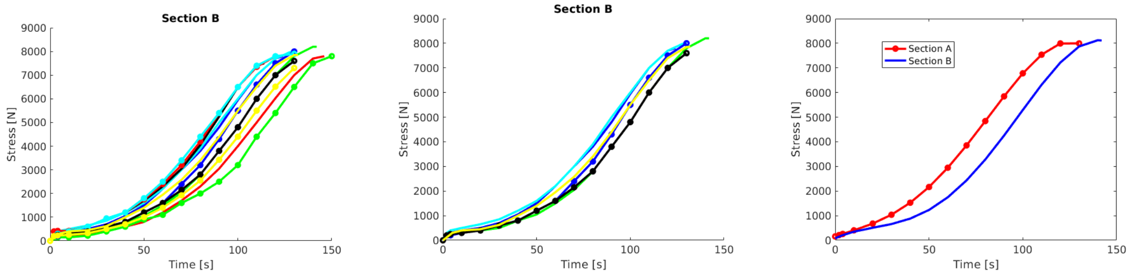

(d) 12 wires **(e)** Seven wires **(f)** Polynomial

Figure 12. Stress *vs.* time graph. (a) and (d) show the 12 wires of section A and B. (b) and (e) were generated by removing the curvy cables at the top and bottom of the graph. (c) corresponds to the breakdown load distribution in section A and B wires, and (f) represents the polynomial approximation using the curves (b) and (e)

$$T_B[N] = -9{,}6659^{-5}t^4 + 0{,}0231^3 - 1{,}1857t^2 + 36{,}8102t + 77{,}6075 \quad (2)$$

3.4. Chemical analysis

Once the tension tests had been carried out, we performed a chemical analysis. Through dispersive X-ray, the energy of a healthy wire was scanned, validating that the sample corresponded to an aluminum alloy. Fig. 13 shows, as a percentage, the base elements on the surface: Al (96.9 %), Cu (1.7 %), Fe (0.9 %), and Si (0.5 %). The analyzed sample was named *Spectrum 66*.

In the images of Fig. 14, a wire of the OPGW is seen to be visibly affected, with signs of pitting and a reduced cross-section. With prior verification through visual, dimensional, and microscopic inspection, a few bites were analyzed, corroborating the presence of corrosive agents, in addition to quantifying the loss of base material.

The chemical analysis of the pitting area defined as *Spectrum 69* can be observed in Fig. 15. The results indicate a high concentration of oxide due to the amount of oxygen recorded (58.7 %), which suggests an accelerated process regarding the natural oxidation of the base material (Fe), observed in the form of a reddish-brown coloration. In this case, natural oxidation was mostly generated by humidity and environmental conditions. The deposits attached to the wire's aluminum contained highly corrosive elements concentrated in the pitting area, such as sulfur (S), *i.e.*, up to 4 %, which is a large amount of corrosive agent. The percentage of coating on the wire, which should remain above 90 % (Al), was 35 %, indicating losses. Therefore, the health of the element's coating was affected by the operating conditions. The guard wire with optical fibers exhibited reduced electrical properties and mechanics in this area.

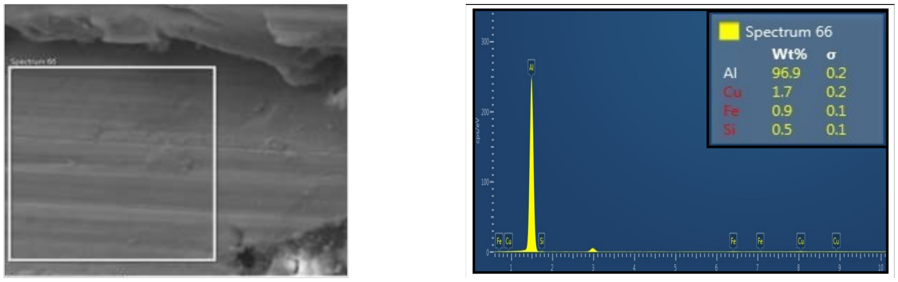

Figure 13. Elemental chemical analysis of the crown that makes up the OPGW

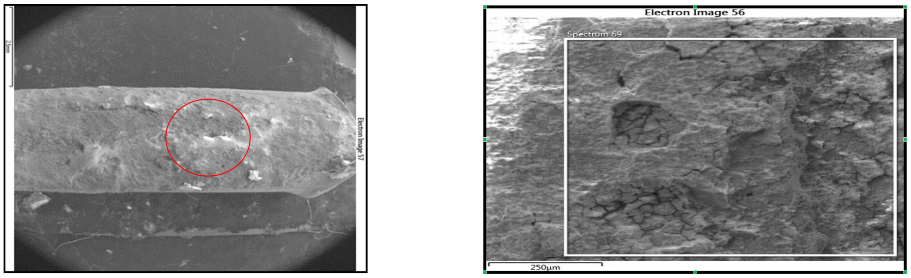

Figure 14. Zoom-in of the red zone of a visibly affected wire, with signs of pitting and corrosion. The chemical analysis of this zone is shown in Fig. 15

The deposits adhered to the wires were also identified. The aluminum coating contained corrosive elements such as S and Na in the zone of base material loss, and we observed the loss of the covering layer and a significant percentage of oxygen due to the oxidation process caused by environmental and industrial impacts. The agents usually come from industrial areas and combine with oxygen and moisture in the environment, leading to the formation of acids and hydroxides that act as corrosive agents and accelerate the degradation of the material. These corrosive agents act mainly on the galvanized steel wires that make up the core of the cable, aggressively deteriorating their Zn layer, penetrating into the base material. With the above, a material loss process takes place, decreasing the wire's diameter and inducing a stress concentration on the driver element. The area decrease generates a temperature increase in the wires, as current is conducted through a smaller cross-section. Under these conditions, wires subjected to combined electromechanical and thermal stress can gradually yield, resulting in rupture.

	Wt%	σ
O	58.7	0.1
Al	35.0	0.1
S	4.0	0.0
Fe	1.1	0.0
Si	0.9	0.0
Ca	0.2	0.0
K	0.1	0.0

Figure 15. Elemental chemical analysis of pitting in the OPGWs

4. Discussion of the results and recommendations

OPGWs must meet standards and requirements based on physical, electric, mechanical, and optical aspects. Recent research in this field has focused on electrical aspects, *e.g.*, the continuous monitoring and maintenance of voltage transmission lines. These studies have used cable samples exposed to atmospheric discharge, which have been reproduced in laboratory settings (2, 3, 10, 16, 17). Multiple consecutive lightning strikes on OPGWs have been achieved using impulse and direct current (11), resulting in conditions such as arc sweep, melting, and ablation damage, affecting the internal optical fiber.

As for the mechanical aspects, the analysis performed involved continuously monitoring thermal behavior and melting in the face of induced atmospheric discharges (1, 3, 18). The mechanical and electrical analyses were directly related (4, 11, 16, 19). To validate the mathematical analysis aimed at predicting cable melting or failure, it was necessary to produce atmospheric discharges. In this research project, the tests were mechanical. In Latin America, there are few certified laboratories for testing OPGWs, where an average of 12 standardized tests are carried out on them, 10 mechanical and two electrical. The laboratory in which our tests took place has the certification, standards, and requirements necessary for development and evaluation.

For (3), as in this research, determining the characteristics (including cable classification and class) of OPGWs is essential for installation in specific regions. The authors of (18) tested various commercial cables while considering critical factors such as their material, thermal properties, and structure. For this project, the type of cable and the arrangement of the wires in the crown and the material were also necessary. With the reference data offered by the manufacturer, the performance and quality after failure of OPGWs in a coastal area were analyzed through mechanical tests. These tests were fundamental to determining the cause of failure and ascertaining whether the type of failed cable was a suitable option for installation.

(2) determined that these cables have greater rigidity, which is suitable for icy conditions or freezing. This causes a phenomenon known as *galloping*, wherein the wires start to deform at 30 kN or below due to creeping. Since some manufacturers consider operating temperature ranges of -40 to 70 ^{o}C

to be correct, it is interesting to analyze this type of cable regarding its degree of affectation by extreme cold. For comparison with the aforementioned value of 30 kN, according to Table II, the breaking load of each of the 12 wires is 8 kN on average. National manufacturers and the Federal Electricity Commission's technical specification indicate that OPGWs' breaking value is around 78 kN, so it is essential to carry out more tests to determine the properties of these cables after failure events.

As technical recommendations, because atmospheric discharges are the cause for many transmission line failures, it is paramount to understand the effect they cause on cable shielding in transmission towers at the national level. Nowadays, atmospheric discharges account for 45 % of failures at voltage levels of 69-400 kV (13). Therefore, using good shielding in electrical systems helps to significantly reduce the damage caused by atmospheric discharges. This shielding must be excellent and based on the grounding system design of each tower, and it must consider the recommended design resistivity. According to the CFE 00J00-52 specification, the grounding resistivity must generally be less than or equal to 10 Ω (13).

5. Conclusions

This research addresses the issues caused by lightning strikes on transmission lines, which tend to impact OPGW guard cables.

A sample of failed OPGWs was acquired from a transmission line located in the coastal area of Valladolid, Yucatán, Mexico (DZT-A360-RXXY-LT 400 kV line). The samples were divided into sections, A and B, whose properties and conditions after cable failure were analyzed. The failure zone was also studied. The tests carried out were visual and dimensional inspection and mechanical stress and chemical tests. Some lightning strike points were preliminarily marked as the main causes of OPGW breakage.

For sections A and B, each of the 12 wires behaved similarly, mostly exhibiting ductile failures and a reduced cross-section. The preservation of the mechanical properties in the wires at a minimum distance of 0.40 m from the failure zone indicates that the cable still was in good conditions before the atmospheric discharge. According to the chemical analysis, despite the changes in structure, the cable maintained operational mechanical properties even near the failure zone, demonstrating the quality of the cable. Furthermore, deposits of corrosive agents were found, which were minimal and located in the fault zone. The cable type analyzed failed due to a lightning strike, but, according to the chemical and visual tests, it already had signs of corrosion.

Our zonal analysis concluded that the two main causes for failure were atmospheric discharge and natural, gradual corrosion. The former caused a considerable absorption of the energy produced by the electric arc generated on the OPGW. The rupture occurred when the cable was mechanically weakened by the progressive deterioration of the wires and exposed to corrosive agents that modified their physical characteristics, exhibiting material loss and a reduced cross-section, in addition to initiating a stress concentration. Atmospheric discharge also affected the cable's properties by means of an abrupt temperature rise that modified the molecular structure of some of the wires, stiffening or melting them. The strain exerted by the cable's weight was also influential.

The observed corrosion was caused by deposits of the corrosive agents described in the chemical analysis. These agents originate from natural sources or pollutants generated in industrial areas. When combined with oxygen and moisture from the environment, they produce acids and hydroxides that corrode and accelerate the degradation of the material.

Regarding the mechanical stress tests, it was possible to elaborate stress *vs.* time graphs using a fourth-order polynomial. The polynomial characterization of most wires in sections A and B proved to be uniform. This uniformity confirms the excellent mechanical conditions of these cable sections, even though they were located near the fault zone, and lays the groundwork for the characterization of this type of cables.

The purpose of this analysis methodology was to determine the quality of OPGWs after failure. There are different OPGW qualities, as well as arrangements, materials, and classes. This research provides a basis for future research to categorize region-specific cable characteristics according to already established tests. The selection of the necessary cable characteristics should be based on extreme regions, such as those with prevailing winds, icy climates, highly corrosive environments (*e.g.*, marine, coastal, and industrial areas), or common atmospheric discharges. Thus, despite that the studied site is a coastal area, the evidence allowed concluding that the appropriate cable had been installed.

6. Author contributions

- **Erick-Alejandro González-Barbosa**: conceptualization, formal analysis, supervision, writing (original draft), writing (review & editing)
- **Fernando Jurado-Pérez**: investigation, methodology, software, writing (original draft), writing (review & editing)
- **Julio C Méndez Gutiérrez**: validation, visualization, writing (original draft), writing (review & editing)
- **José-Joel González-Barbosa**: visualization, software, writing (original draft), writing (review & editing)

References

[1] L. Lu, Y. Liang, B. Li, J. Guo, H. Zhang, and X. Zhang, "Experimental study on location of lightning stroke on opgw by means of a distributed optical fiber temperature sensor," *Optics Las. Tech.*, vol. 65, p. 79–82, 01 2015. ↑ 3, 16

[2] L. Lu, Y. Liang, B. Li, and J. Guo, "Maintenance of the opgw using a distributed optical fiber sensor," in *2014 Int. Conf. Power Syst. Tech.*, 2014, pp. 1251–1256. https://doi.org/10.1109/POWERCON.2014.6993536 ↑ 3, 4, 16

[3] M. Iwata, T. Ohtaka, Y. Kuzuma, and Y. Goda, “Development of a method of calculating the melting characteristics of opgw strands due to dc arc simulating lightning strike,” *IEEE Trans. Power Del.*, vol. 28, no. 3, pp. 1314–1321, 2013. https://doi.org/10.1109/TPWRD.2013.2260567 ↑ 3, 16

[4] M. Iwata, T. Ohtaka, and Y. Kuzuma, “Analytical investigation on opgw strands melting due to dc arc discharge simulating lightning strike,” in *2012 Int. Conf. Light. Prot. (ICLP)*, 2012, pp. 1–5. https://doi.org/10.1109/ICLP.2012.6344238 ↑ 3, 4, 16

[5] M. Iwata, T. Ohtaka, and Y. Goda, “Calculation of melting/breaking of gw and opgw strands struck by dc arc discharge simulating high energy lightning,” *Elec. Power Syst. Res.*, vol. 113, pp. 70–78, 2014. ↑ 3

[6] A. Gunday and S. E. Karlık, “Optical fiber distributed sensing of temperature, thermal strain and thermo-mechanical force formations on opgw cables under wind effects,” in *2013 8th Int. COnf. Elec. Electron. Eng. (ELECO)*, 2013, pp. 462–467. https://doi.org/10.1109/ELECO.2013.6713885 ↑ 3

[7] W. Shang, J. Gong, X. Zhi, and H. Wang, “Hffb test and wind-induced vibration analysis on 1 000 kv transformer frame,” *Ing. Invest.*, vol. 43, no. 1, p. e88403, Nov. 2022. https://doi.org/10.15446/ing.investig.88403 ↑ 4

[8] L. Yuqing, C. Xi, L. Chen, W. Yang, and H. Baosu, “Study on a new and high efficient opgw melting ice scheme,” in *2015 2nd Int. Conf. Info. Sci. Control Eng.*, 2015, pp. 480–484. https://doi.org/10.1109/ICISCE.2015.111 ↑ 4

[9] W. Bi, L. Tian, C. Li, Z. Ma, and H. Pan, “Wind-induced failure analysis of a transmission tower-line system with long-term measured data and orientation effect,” *Rel. Eng. Syst. Safety*, vol. 229, p. 108875, 2023. ↑ 4

[10] T. Du, Y. Zhang, and W. Xia, “Study on the problem of lightning strike opgw,” 2006, pp. 1–4. ↑ 4, 16

[11] J. Sun, X. Yao, J. Ren, Y. Le, Y. Wu, and M. Rong, “Analytical investigation of lightning strike-induced damage of opgws based on a coupled arc-electrical-thermal simulation,” *IEEE Trans. Power Del.*, vol. 37, no. 6, pp. 5145–5155, 2022. https://doi.org/10.1109/TPWRD.2022.3171783 ↑ 4, 5, 16

[12] C. R. de Energía, “Reporte de confiabilidad del sistema eléctrico nacional,” 2022, november 27, 2024. https://www.gob.mx/cms/uploads/attachment/file/876900/Anexo_Acuerdo_A-075-2023.pdf ↑ 5

[13] C. F. de Electricidad, “Cable guarda con fibras ópticas. especificación cfe e1000-21,” 2019, november 27, 2024. https://lapem.cfe.gob.mx/normas/pdfs/u/E1000-21.pdf ↑ 5, 17

[14] A. International, *Standard specification for aluminum 1350-H19 wire for electrical purposes*, ASTM Std. B230, 2022. https://www.astm.org/b0230_b0230m-22.html ↑ 7

[15] ASTM, *Standard specification for concentric-lay-stranded aluminum conductors, coated-steel reinforced (ACSR)*, ASTM Std. B232, 2024. https://www.astm.org/b0232_b0232m-24.html ↑ 7

[16] Y. Goda, S. Yokoyama, S. Watanabe, T. Kawano, and S. Kanda, "Melting and breaking characteristics of opgw strands by lightning," *IEEE Trans. Power. Del.*, vol. 19, no. 4, pp. 1734–1739, 2004. https://doi.org/10.1109/TPWRD.2004.832410 ↑ 16

[17] T. Prabakaran, S. Munshi, H. Roy, and S. Pathak, "Failure analysis on opgw cable during short circuit test," *Power Res. J. CPRI*, pp. 81–85, 2023. ↑ 16

[18] L. Jie, L. Gang, and C. Xi, "Study on the thermal stability of opgw under large curren condition," in *2009 Pacific-Asia COnf. Circ. Comm. Syst.*, 2009, pp. 629–635. https://doi.org/10.1109/PACCS.2009.103 ↑ 16

[19] M. Iwata, T. Ohtaka, Y. Goda, S. Yamagami, A. Kato, and K. Nagano, "Melting and breaking characteristics of strands of high-strength and high-corrosion-resistant opgw due to dc arc discharge simulating high-energy lightning strike," *Elec. Eng. Japan*, vol. 214, no. 4, p. e23345, 2021. ↑ 16

Erick-Alejandro González-Barbosa

With a rich academic background, Erick-Alejandro González-Barbosa obtained Bachelor's, Master's, and PhD degrees in Mechanical Engineering from the University of Guanajuato in 2004, 2006, and 2012, respectively. He is a research professor at Tecnológico Nacional de México/Instituto Tecnológico Superior de Irapuato's Division of Electromechanical Engineering. His areas of interest and expertise include the modeling and simulation of electromechanical and mechatronic systems, the kinematics and dynamics of planar mechanisms and industrial robots, and mechanical design.

Email: erick.gb@irapuato.tecnm.mx

Fernando Jurado-Pérez

He holds a Master's degree in Electrical Engineering, as well as in Electromechanical Engineering. He is a research professor at Tecnológico Nacional de México/Instituto Tecnológico Superior de Irapuato's Division of Electromechanical Engineering and as an advisor in the mechanical testing department of the Federal Electricity Commission, where he has contributed to the formulation and development of applied research projects in various areas of the electrical and mechanical sciences. His research focuses on developing mechanical and electrical tests on ACCC, ACSR, and OPGW cables and on cultivating the custom power research line.

Email: fernando.jp@irapuato.tecnm.mx

José-Joel González-Barbosa

He holds an Engineering degree in Communications and Electronics, a Master's degree from the University of Guanajuato, Mexico, and a second Master's and a PhD in Computer Science from the INP of Toulouse, France. He did a research stay at LAAS-CNRS, Toulouse, France (1999-2004) and a sabbatical stay at ISR-Coimbra, Portugal (2018-2019). He is an associate professor at CICATA-IPN, Mexico, where he teaches computer vision, image processing, pattern recognition, and scientific

computing courses. His research interests include multi-camera systems, 3D computer vision, panoramic vision, object recognition, robotics, and augmented and virtual reality.
Email: jgonzalezba@ipn.mx

Julio César Méndez Gutiérrez

He obtained an Electromechanical Engineering degree and is currently a student of the Master's Program in Electrical Engineering at Instituto Tecnológico Superior de Irapuato. He is the leader of the Federal Electricity Commission's Mechanical Testing Laboratory for Transmission and Distribution Systems, where prototype tests are developed and executed based on national and international regulations, including those for OPGWs, ASCR, and ACCC conductors. He has also worked in the private sector, in the design and calculation of medium voltage electrical installations, and in procedures before the Federal Electricity Commission. He also has an interest in electrical power systems.
Email: mip22110015@irapuato.tecnm.mx

UNIVERSIDAD DISTRITAL
FRANCISCO JOSÉ DE CALDAS

Ingeniería

https://revistas.udistrital.edu.co/index.php/reving/issue/view/1241

DOI: https://doi.org/10.14483/23448393.22162

Research

Passivity-Based Model-Predictive Control for the Permanent Magnet Synchronous Machine

Control predictivo basado en pasividad para la máquina síncrona de imanes permanentes

Alejandro Garcés-Ruiz* and Walter Gil-González,

Department of Electric Power Engineering, Universidad Tecnológica de Pereira, Pereira 660003, Colombia.

Abstract

Context: This study focuses on advanced control techniques for permanent magnet synchronous machines (PMSMs), which are crucial in various industrial applications due to their efficiency and precise control requirements. Passivity-based control methods offer stability and performance, addressing these challenges effectively.
Method: A passivity-based model predictive control (MPC) is proposed, integrating port-Hamiltonian representation with optimization. Stability theorems are theoretically explored. The simulation evaluates the performance of our proposal under different prediction horizons and stability constraints.
Results: The proposed MPC is analyzed across several horizons, both including and excluding passivity and exponential stability constraints.
Conclusions: This study presents a novel passivity-based MPC approach for PMSM speed regulation, highlighting the importance of stability constraints. Future research should extend this controller to synchronous machines in power systems and voltage source converters.

Keywords: passivity-based control, Permanent-magnet synchronous machines, model-predictive control, stability

Article history

Received:
14th /May/2024

Modified:
23rd /Jul/2024

Accepted:
10th /Agu/2024

Ing, vol. 29, no. 3,
2024. e22162

---

*[*] **Correspondence:** alejandro.garces@utp.edu.co

Resumen

Contexto: Este estudio se centra en técnicas avanzadas de control para máquinas síncronas de imanes permanentes (PMSM), fundamentales en diversas aplicaciones industriales debido a su eficiencia y requisitos de control precisos. Los métodos de control basados en pasividad ofrecen estabilidad y rendimiento y permiten abordar eficazmente estos desafíos.

Métodos: Se propone un control predictivo basado pasividad (MPC), integrando la representación port-Hamiltoniana con la optimización. Se exploran teoremas de estabilidad teóricamente. La simulación evalúa el rendimiento de nuestra propuesta bajo diferentes horizontes de predicción y restricciones de estabilidad.

Resultados: El MPC propuesto se analiza en varios horizontes, incluyendo y excluyendo restricciones de pasividad y estabilidad exponencial.

Conclusiones: Este estudio presenta un enfoque novedoso de MPC basado en pasividad para la regulación de velocidad de PMSM, destacando la importancia de las restricciones de estabilidad. La investigación futura debería extender este controlador a máquinas síncronas en sistemas de energía y convertidores de fuente de voltaje.

Palabras clave: control basado en pasividad, máquinas síncronas de imanes permanentes, control predictivo basado en el modelo, estabilidad

Table of contents

1. Introduction

1.1. Motivation

The permanent magnet synchronous machine (PMSM) is a classic technology that has been revitalized in recent years. It is commonly used in wind energy (1), hydro-power generation (2), wave and tidal energy systems (3), electric vehicles (4) and microgrids (5), among other industrial applications. The dynamics of this machine are described by nonlinear equations that are sensitive to unknown external disturbances, which complicates the control task. Therefore, nonlinear controls are required to adjust for nonlinearities and drawbacks (6).

A PMSM can be represented in the framework of port-Hamiltonian systems (7). This characteristic is convenient for the use of passivity-based controls, which ensure stability and maintain the natural dynamics of the physical system. However, passivity-based controls may be surpassed by conventional ones in terms of efficiency (8).

On the other hand, model-predictive control has become popular in industrial applications, given its advantages in terms of performance (9). In addition, it is a nonlinear control capable of introducing constraints into the model (10). However, the stability and structural properties of physical systems may be compromised in the design stage (11). Therefore, there is a research gap regarding the interaction between passivity-based and model-predictive control in practical applications such as the speed regulation of PMSMs.

1.2. State of the art

Passivity-based control has been used to control PMSMs in different applications. In (12), a control for small hydro-power generation plant was proposed. The control was stable and preserved structural properties during closed-loop operation. An $H\infty$ robust control based on the Hamilton-Jacobi inequality was presented in (13). This control exhibited a port-controlled Hamiltonian structure with the dissipation form. In addition, a passivity-based control for the speed regulation of a permanent magnet synchronous motor was presented in (14). Experimental results showed that the control was easy to program, as it was reduced to a set of algebraic equations. In all these cases, the goal was the stability and practical implementation of the control, but they lacked a profound study of the improvement in performance.

In recent years, various advanced nonlinear control topologies have been developed to enhance the speed regulation performance of PMSMs across different applications. These approaches include artificial neural network control (15), adaptive control (16), backstepping-fuzzy control (17), neural network control (18), adaptive fuzzy logic control (19), sliding mode control (20), active disturbance rejection control (21), predictive current control (22), synergetic control (23), and adaptive extended-state observer control (24). While recent advancements in nonlinear control techniques (15, 24) have shown promising results in improving the speed regulation performance of PMSMs, each approach also comes with its own set of limitations. For instance, neural network control may require extensive training data and computational resources, while sliding mode control can be sensitive to uncertainties and parameter variations. Adaptive control strategies, although versatile, may face challenges in ensuring robustness across all operating conditions. Additionally, disturbance rejection or synergetic control methods often rely on accurate models, which can be restrictive in practical implementations.

On the other hand, model-predictive control is another nonlinear technique that has been used for controlling PMSMs. For instance, in (25), a finite control set model-predictive control was suggested for speed regulation with improved parameter robustness; a speed-current single-loop was proposed in (26) for electric vehicle applications; a linearized model-predictive control was presented in (27); and a data-driven model-predictive control was introduced in (28). None of these controls preserved the structural properties of the original dynamic system.

Few studies unifying model-predictive and passivity-based control can be found in the scientific literature. Most of them are based on theoretical properties rather than in the applications. (29) proposed a passivity-based model-predictive control inspired by the relationship between optimal control and model-predictive control. Moreover, passivity and dissipativity have been studied to achieve stability in economic models (30), but it is generally difficult to characterize dissipative systems in that context. A passivity-based model-predictive control was proposed in (31) for the regulation of a robot manipulator. The introduction of passive constraints proved to be particularly appealing, as robustness against model uncertainty was inherently ensured. Despite these advantages, the implementation of these controls was particularly challenging, as discussed in (32).

1.3. Contribution

To the best of the authors' knowledge, there is no previous application of passivity-based model-predictive control for speed regulation in PMSMs. This paper proposes an innovative approach that integrates port-Hamiltonian representation into the optimization problem. The contributions of this work include:

- A novel control strategy based on passivity-based model-predictive control, which effectively regulates the speed of PMSMs.
- A detailed analysis of the impact of different time horizons on the performance and execution times of the proposed control strategy.
- An examination of how passivity and exponential stability constraints influence response times and simulation times according to the prediction horizon.

1.4. Outline

The rest of this paper is organized as follows. Section 2 introduces the port-Hamiltonian model of the permanent magnet synchronous generator, as well as the conditions for the existence of the equilibrium point and the incremental model. The proposed model-predictive control is described in section 2, followed by the main stability properties in §3.2. Afterwards, section 4 presents a complete set of numerical experiments, finalizing with the conclusions and proposals for future work (§5).

1.5. Notation

Throughout this document, matrices are represented by capital letters, while vectors and scalars are denoted by low-case letters. The entries of the matrices are also represented by low-case letters. Thus, for a matrix $A \in \mathbb{R}^{n\times n}$, there are entries a_{ij}; for any vector $x \in \mathbb{R}^n$, $\|x\|$ is the Euclidean norm and $\|x\|_Q$ is $\sqrt{x^\top Q x}$ with $Q \succ 0$; and the symbols $\succeq$ and $\succ$ represent the Loewner order of positive semi-definite matrices. The equilibrium point is represented by variables with an overline. The full nomenclature is presented below:

Nomenclature

η	Number of pole pairs
μ_m	Inertia constant
ω_e	Angular speed
ψ_m	Flux in the permament magnents
τ_m	Electrical torque
τ_m	Mechanical torque
i_d	Input current in the direct axis
i_q	Input current in the quadrature axis
l_d	Equivalent inductance in the direct axis
l_q	Equivalent inductance in the quadrature axis
r_s	Stator resistance
v_d	Input voltage in the direct axis
v_q	Input voltage in the quadrature axis

2. Modeling the permanent-magnet synchronous machine

2.1. State-space representation

The model presented in (1) represents a PMSM connected to a constant mechanical load with a torque τ_m:

$$\begin{aligned} l_d \frac{di_d}{dt} &= v_d - r_s i_d + \omega_e l_q i_q, \\ l_q \frac{di_q}{dt} &= v_q - r_s i_q - \omega_e (l_d i_d + \psi_m), \\ \mu_m \frac{d\omega_e}{dt} &= \tau_e - \tau_m. \end{aligned} \tag{1}$$

This model is represented within a $dq0$ reference frame aligned with the q-axis[**]. The state variables are the currents in the stator (i_d, i_q) and the rotor's electrical rotational speed ω_e. The electrical torque is given by (2):

$$\tau_e = \frac{1}{\kappa}(i_q(l_d i_d + \psi_m) - l_q i_d i_q), \tag{2}$$

where $\kappa = 2/(3\eta)$ and η is the number of pole pairs. The rest of the parameters correspond to the stator inductance l_d, l_q, the stator resistance r_s, the permanent magnet flux linkage ψ_m, and the inertia μ_m.

---

[*] *This implies that $v_q = 0$

2.2. Port-Hamiltonian model

Port-Hamiltonian systems constitute a family of dynamic systems with useful structural properties such as passivity and disipativity. This family is a framework used to model and analyze physical systems by incorporating both energy-based methods and network theory. It is especially useful for representing complex interconnected systems with energy exchange, such as mechanical, electrical, hydraulic, or thermal systems. This type of dynamic systems is defined below.

Definition 1. A port-Hamiltonian system with dissipation is a dynamic system that can be described, in local coordinates, by the following input-state-output representation:

$$\begin{aligned} \dot{x} &= (J(x) - R)\nabla H(x) + Gu, \\ y &= G^\top \nabla H(x), \end{aligned} \tag{3}$$

where x represents the state variables, u is the input, y is the output, $J = -J^\top$ is an interconnection matrix, $R = R^\top \succeq 0$ is a dissipation matrix, and H is a Hamiltonian function.

The permanent magnet synchronous generator admits a port-Hamiltonian model with state variables $x_1 = l_d i_d$, $x_2 = l_q i_q$, and $x_3 = \kappa \mu_m \omega_e$ as well as the control input $u = [v_d,\ v_q,\ \kappa\tau_m]$. The input-output model is presented in (3), where the Hamiltonian function is a quadratic form given by (4):

$$H = x^\top Q x. \tag{4}$$

The specific diagonal and positive semi-definite matrices $Q = Q^\top \succeq 0$ and $R = R^\top \succeq 0$ are defined as follows:

$$\begin{aligned} Q &= \operatorname{diag}([1/l_d, 1/l_q, 1/(\kappa\mu)]), \\ R &= \operatorname{diag}([r_s, r_s, 0]), \end{aligned} \tag{5}$$

where R represents the natural damping of the dynamic system. In addition, a bilinear skew-symmetric interconnection matrix $J(x) = -J(x)^\top$ is defined, as given below.

$$J(x) = J_0 + x_1 J_1 + x_2 J_2,$$

where:

$$J_0 = \begin{bmatrix} 0 & 0 & 0 \\ 0 & 0 & -\psi_m \\ 0 & \psi_m & 0 \end{bmatrix},$$

$$J_1 = \begin{bmatrix} 0 & 0 & 0 \\ 0 & 0 & -1 \\ 0 & 1 & 0 \end{bmatrix},$$

$$J_2 = \begin{bmatrix} 0 & 0 & 1 \\ 0 & 0 & 0 \\ -1 & 0 & 0 \end{bmatrix}.$$

Finally, G and $\nabla H(x)$ are given by (6) and (7):

$$G = \operatorname{diag}([1, 1, -\kappa]), \tag{6}$$

$$\nabla H(x) = Qx. \tag{7}$$

In this case, the existence and uniqueness of the solution can be ensured, since the nonlinearities of the model come in the form of the local Lipschitz continuous functions in $x \in \mathbb{X} \subseteq \mathbb{R}^3$.

Conventionally, PMSMs are operated with a unitary power factor in order to reduce power losses[***]. Therefore, the equilibrium point is characterized by $\bar{i}_d = 0$. The desired rotational frequency is $\overline{\omega}_e$, and $\overline{\tau}_e = \tau_m$. Thus, $\bar{i}_q = \kappa\tau_m/\psi_m$.

The equilibrium of the port-Hamiltonian system is $\overline{x} = Q^{-1}[\bar{i}_d, \bar{i}_q, \overline{\omega}_e]^\top$. Likewise, the input in the stationary state is obtained by isolating the variable u in (3), as shown below:

$$\overline{u} = -G^{-1}((J(\overline{x}) - R))Q\overline{x}. \tag{8}$$

Note that (8) is well defined since G is non-singular. Next, new state and input variables are defined: $\Delta x = x - \overline{x}$ and $\Delta u = u - \overline{u}$. These variables allow defining the following incremental model:

$$\Delta\dot{x} = (\Delta x_1 J_1 + \Delta x_2 J_2)Q\overline{x} + (J(\overline{x} + \Delta x) - R)Q\Delta x + G\Delta u. \tag{9}$$

Part of the port-Hamiltonian structure is lost for this incremental model. In fact, the incremental model (9) can be represented by the following Lurie system[****], where the nonlinear part is a port-Hamiltonian system:

$$\Delta\dot{x} = A\Delta x + (J(\overline{x} + \Delta x) - R)Q\Delta x + G\Delta u,$$

where A is a 3×3 matrix that results from horizontally concatenating the column vectors associated with Δx_1 and Δx_2 and a zero vector, as given in (10):

$$A = \left[J_1 Q\overline{x},\ J_2 Q\overline{x},\ 0\right]. \tag{10}$$

It is worth noting that $A = 0$ for $\overline{x} = 0$, resulting in the original system (3). However, $\overline{x} \neq 0$ for most practical applications. Hence, the incremental model is not port-Hamiltonian. This aspect has a direct consequence on the passive structure of the closed-loop system, which will be analyzed below.

2.3. Passivity

Several dynamic systems, such as port-Hamiltonian ones, share a common structural property named *passivity*, which reveals the energy behavior and easily allows to prove stability. The following definition is used in this article:

Definition 2. A dynamic system $\dot{x} = f(x, u)$ with the state variables $x \in \mathbb{X} \subseteq \mathbb{R}^n$, the inputs $u \in \mathbb{U} \subseteq \mathbb{R}^m$, and the output $y = h(x, u) \in \mathbb{R}^m$ is considered to be passive if there is a differentiable storage function $S : \mathbb{X} \to \mathbb{R}$ with $S(x) \geq 0$, satisfying the differential dissipation inequality

$$\dot{S}(x) \leq u^\top y \tag{11}$$

across all solutions $x(t)$ corresponding to the input function u.

[***] Reactive power is given by $q = v_q i_q - v_q i_d$. In this vein, since $v_q = 0$ due to the alignment of the reference frame, the unitary power factor is equivalent to $i_d = 0$. Moreover, the power losses are given by $r_s(i_d^2 + i_q^2)$, so they are reduced as the total current decreases, *i.e.*, when $i_d = 0$.

[****] A Lurie system is a linear time-invariant plant connected to a nonlinearity.

As a port-Hamiltonian system, the model associated with the PMSM is a passive system with a storage function $S(x) = H(x) - H(\tilde{x})$, where $\tilde{x} = \text{arming}(H(x))$ (zero in this case). Unfortunately, the port-Hamiltonian structure is lost for the incremental model given by (9). Therefore, additional conditions are required to maintain passivity[*****].

Lemma 1. *The incremental model given by* (9) *is passive with the storage function* $S = \frac{1}{2}\Delta x^\top Q \Delta x$ *and the output* $y = G^\top Q \Delta x$ *if the following constraint is imposed:*

$$\phi_1(\Delta x) \leq \phi_2(\Delta x), \tag{12}$$

where,

$$\phi_1(\Delta x) = \frac{1}{2}\Delta x^\top (A^\top Q + QA)\Delta x, \tag{13}$$

$$\phi_2(\Delta x) = \Delta x^\top Q^\top R Q \Delta x. \tag{14}$$

Proof. This can be easily proved by calculating $\dot{S}$ as given below:

$$\dot{S} = \frac{1}{2}\Delta \dot{x}^\top Q \Delta x + \frac{1}{2}\Delta x^\top Q \Delta \dot{x}.$$

Then, (9) is substituted, considering that J is skew symmetric, in order to obtain the following:

$$\dot{S} = \frac{1}{2}(A\Delta x - RQ\Delta x + G\Delta u)^\top Q\Delta x + \frac{1}{2}\Delta x^\top Q(A\Delta x - RQ\Delta x + G\Delta u).$$

Now, (13) and (14) are used to obtain the following:

$$\dot{S} = \phi_1(\Delta x) - \phi_2(\Delta x) + \Delta u^\top G^\top Q \Delta x,$$

which satisfies (11) with the output $y = G^\top Q \Delta x$ if inequality (12) holds. □

Note that $\phi_2(\Delta x) \geq 0$ for any Δx, given that $R \succeq 0$. However, $\phi_1(\Delta x)$ may be a saddle; for example, for $\overline{x}_1 = 0$, the following holds:

$$\phi_1(\Delta x) = q_3\overline{x}_3(q_1 - q_2)\Delta x_1 \Delta x_2 + q_2 q_3 \overline{x}_2 \Delta x_1 \Delta x_3,$$

where $q_1 = 1/l_d, q_2 = 1/l_q$ and $q_3 = 1/(\kappa\mu)$, as previously defined in (5). Eq. (12) holds in a stationary state since, in that case, $\Delta x = 0$. The constraint is easily satisfied for small values of Δx. However, it may be challenging for large deviations from the equilibrium point. Hence, (12) defines a feasible region for the optimization problem, as presented in the next section.

Fig. **1** shows ϕ_1 for a non-salient machine. There are regions in the state space where (12) is naturally satisfied, *e.g.*, in the points where $\phi_1 \leq 0$. Other regions require imposing this passivity constraint, as proposed in the next section.

[*****] See (33), chapter 7, for more details about the passivity of port-Hamiltonian systems

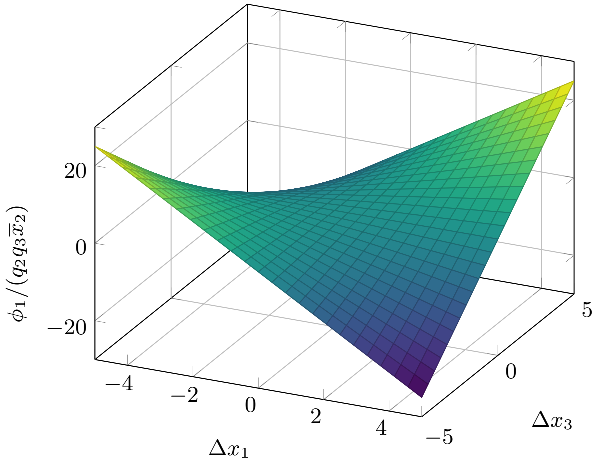

Figure 1. 3D representation of $\phi(\Delta x)$ for $l_d = l_q$ (non-salient rotor)

3. Proposed model-predictive control

3.1. The optimal control problem

Model-predictive control can be considered as a variant of an optimal control problem applied in a receding horizon. The concept is based on four simple steps: measurement or estimate of the state x_t (step 1) and the solution of the optimal control problem in a finite horizon T (step 2). This optimization problem yields a sequence of optimal inputs $\{u_t, u_{t+1}, u_{t+2}, \dots\}$ over the entire horizon. However, we only execute the control command u_t (step 3) and wait until the next step to take the measurements of the state x_{t+1} and solve the optimization model once again (step 4). These steps are schematically shown in Fig. 2.

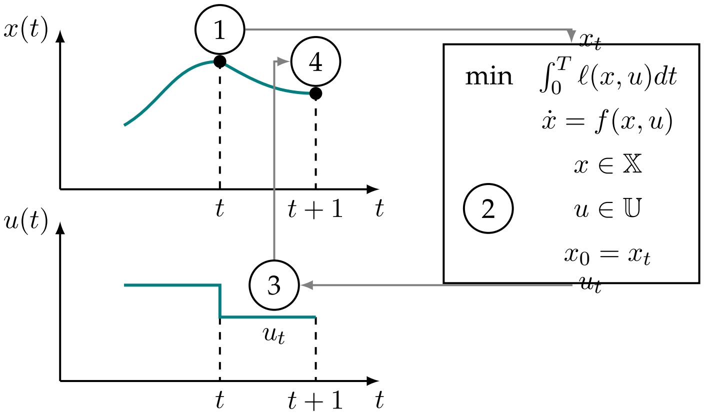

Figure 2. Schematic representation of the model-predictive control

In the case of the permanent magnet synchronous generator, the state space is assumed to be $\mathbb{X} = \mathbb{R}^3$, and the input space is defined by the set of feasible inputs. The external torque is known, making $u_3 = \overline{u}_3 = \tau_m$. This entails the following input set:

$$\mathbb{U} = \left\{\Delta u \in \mathbb{R}^3 : \ \Delta u_3 = 0\right\}$$

The passivity condition given by Lemma 1 is incorporated into the optimization to ensure structural properties in closed-loop operation.

This work proposes the following optimal control problem, which is translated, without loss of generality, from $t = 0$ into $t = T$:

$$\begin{aligned}
\text{mín} \int_0^T & \Delta x^\top Q \Delta x + \Delta u^\top M \Delta u + \alpha_p z_p^2 + \alpha_e z_e^2 \, dt, \\
& \Delta \dot{x} = A\Delta x + (J(\overline{x} + \Delta x) - R)Q\Delta x + G\Delta u, \\
& \Delta y = G^\top Q \Delta x, \\
& \phi_1(\Delta x) - \phi_2(\Delta x) \leq z_p, \\
& \Delta y^\top \Delta u \leq -\frac{\epsilon}{2}\Delta x^\top Q \Delta x + z_e, \\
& \Delta u \in \mathbb{U}, \\
& \Delta x \in \mathbb{X},
\end{aligned} \tag{15}$$

where $M \succ 0$ is a weight matrix related to the inputs, and (z_p, z_e) are slack variables that allow defining soft constraints. Note that, the rest of the variables were already defined in the previous section.

Soft constraints are used to ensure the feasibility of the optimization problem, allowing for some degree of violation, which is penalized in the cost function through a quadratic form with weights α_p and α_e. Unlike hard constraints, which must be satisfied at all times, soft constraints provide the control optimization process with a certain degree of flexibility. However, it is expected that $z_p = z_e = 0$ for most of the control execution time. In this case, ϵ is a small positive constant used to ensure exponential stability, as presented in the next section.

3.2. Stability analysis

Proving stability in nonlinear controls is challenging. In particular, stability in model-predictive control is usually obtained by adequately selecting the terminal conditions (34). These conditions include a penalization factor or a constraint associated with the time $t = T$. In this case, a different approach was employed, wherein stability is imposed by the passivity conditions. Next, some of the basic concepts required for stability analysis are reviewed.

Theorem 1 (See (35) §3.1)**.** *Consider a nonlinear dynamic system* $\dot{x} = f(x)$ *and assume that there is a continuously differentiable function* $V : \mathbb{X} \to \mathbb{R}$*, such that*

$$\begin{aligned}
& V(0) = 0 \\
& V(x) > 0, \ \forall x \neq 0 \\
& \dot{V}(x) \leq 0, \ \forall x.
\end{aligned}$$

Then, the zero solution is stable in the sense of Lyapunov. If the last inequality is strictly satisfied, then the system is asymptotically stable. Finally, the system is exponentially stable if V *satisfies*

$$\begin{aligned} \alpha \left\| x \right\|^p \leq V(x) \leq \beta \left\| x \right\|^p \\ \dot{V}(x) \leq -\epsilon V(x). \end{aligned}$$

It is important to recall that exponential stability is a stronger result than asymptotic stability. Exponential stability implies that the deviations from the equilibrium state decay at an exponential rate. This means that the system returns to a stable equilibrium state more quickly in comparison with systems that only exhibit asymptotic stability. A faster decay is often crucial in practical applications, in order to ensure a swift recovery from perturbations. Moreover, exponential decay provides a predictable and well-defined rate at which the system returns to equilibrium. This rate can be used in practice for further stability analysis of the entire system.

In our case, the passivity condition imposed on the optimal control problem allows easily proving exponential stability, as presented below:

Theorem 2. *Consider the incremental model* (9)*, where the input* Δu *is calculated through the optimal control problem* (15)*. Suppose that the feasibility of the optimization problem is ensured in every state along the closed-loop trajectory with* $z_p = z_e = 0$*. Then, the resulting closed-loop system is exponentially stable.*

Proof. First, the conditions for the passivity of the incremental model are established. Note that inequality (12) holds when $z_p = 0$. In that case, the system is passive, so it holds that $\dot{S} \leq \Delta y^\top \Delta u$. Moreover, when $z_e = 0$, $\dot{S} \leq -\epsilon S$, with $\epsilon > 0$ and $S = \frac{1}{2}\Delta x^\top Q \Delta x$. Finally, exponential stability is proved by invoking Theorem 1. □

4. Simulations and results

Numerical experiments were performed using Casadi in the Matlab-Simulink environment (36) in order to validate our proposal. All the parameters of the PMSM are presented in Table I

Table I. Parameters of the permanent magnet synchronous machine

Parameter	Variable	Value	Unit
Permanent magnet flux linkage	ψ_m	0.03	Wb
d-axis inductance	l_d	0.20	mH
q-axis inductance	l_q	0.20	mH
Stator resistance	r_s	13.0	$m\Omega$
Electrical rotational speed	ϖ_e	100π	rad/s
Inertia	μ_m	$0.2/\varpi_e$	kg/m^2
Pole pairs	η	6	

Direct collocation with multiple shooting was employed to solve the optimal control problem. Discretization was carried out using an implicit Runge-Kutta method to ensure numerical stability. Three numerical simulations were performed, aiming to evaluate different features of the control, namely:

- S_1 : An analysis under different horizons was considered for the optimal control problem.
- S_2 : The effects of the passivity and the exponential stability constraint were evaluated.
- S_3 : The performance of the proposed control was compared against those of the passivity-based speed (PBS) control presented in (14).

The tuning parameters for the passivity-based model predictive control were $Q = \mathrm{diag}([1/l_d, 1/l_q, 1/(\kappa\mu)])$ and $M = \mathrm{diag}([1., 1, 1]) \times 10^{-3}$.

4.1. Results of simulation S_1

This subsection studies the effect of different step horizons on the proposed control strategy. Fig. 3 illustrates the dynamic responses of the stator currents (Figs. 3a and 3b) and the rotor's electrical rotational speed (Fig. 3c) for the proposed control applied to the PMSM under different horizons. The reference of the electrical rotational speed $\bar{x}_3$ varies by $\pm\overline{\omega}_e$. Fig. 3d presents the simulation times for each of the prediction horizons analyzed.

By analyzing Fig. 3, it can be noted that, for the various prediction horizons employed, the motor achieves the desired references in less than 30 ms (Fig. 3c). Additionally, after five prediction horizons, the dynamic responses of the permanent magnet synchronous motor exhibit a similar behavior. Meanwhile, for a one-step horizon, the response time takes 10 ms longer on average to stabilize, albeit with the shortest simulation time, reporting reductions of 42.74 and 88.71 % when compared to the seven- and 19-step horizons (Fig. 3d). This indicates that, in a larger system, a longer horizon will be the best option.

4.2. Results of simulation S_2

This section analyzes the effect of including (or not) the passivity or the exponential stability constraint for the step horizons $h = 1$ and $h = 19$. The first constraint analyzed is passivity, whose effect is determined by whether it is eliminated from the optimization model presented in (15). Fig. 4 shows the dynamic responses of the stator currents (Figs. 4a and 4b) and the rotor's electrical rotational speed (Fig. 4c) for the proposed control applied to the PMSM under various horizons. The reference of the electrical rotational speed $\bar{x}_3$ remained between $\pm\overline{\omega}_e$. Fig. 4d depicts the simulation time under the prediction horizons $h = 1$ and $h = 19$ with and without the passivity constraint.

In Fig. 4, note that, when the prediction horizon is equal to one ($h = 1$), the impact of the passivity constraint on the proposed control's performance becomes evident, as the simulation times increase (Figs. 4a and 4c). When the prediction horizon is set to $h = 19$, the passivity constraint has minimal impact on the performance of the proposed control. This suggests that, for extended prediction horizons, the proposed control exhibits a passive behavior. Fig. 4d shows that the simulation times

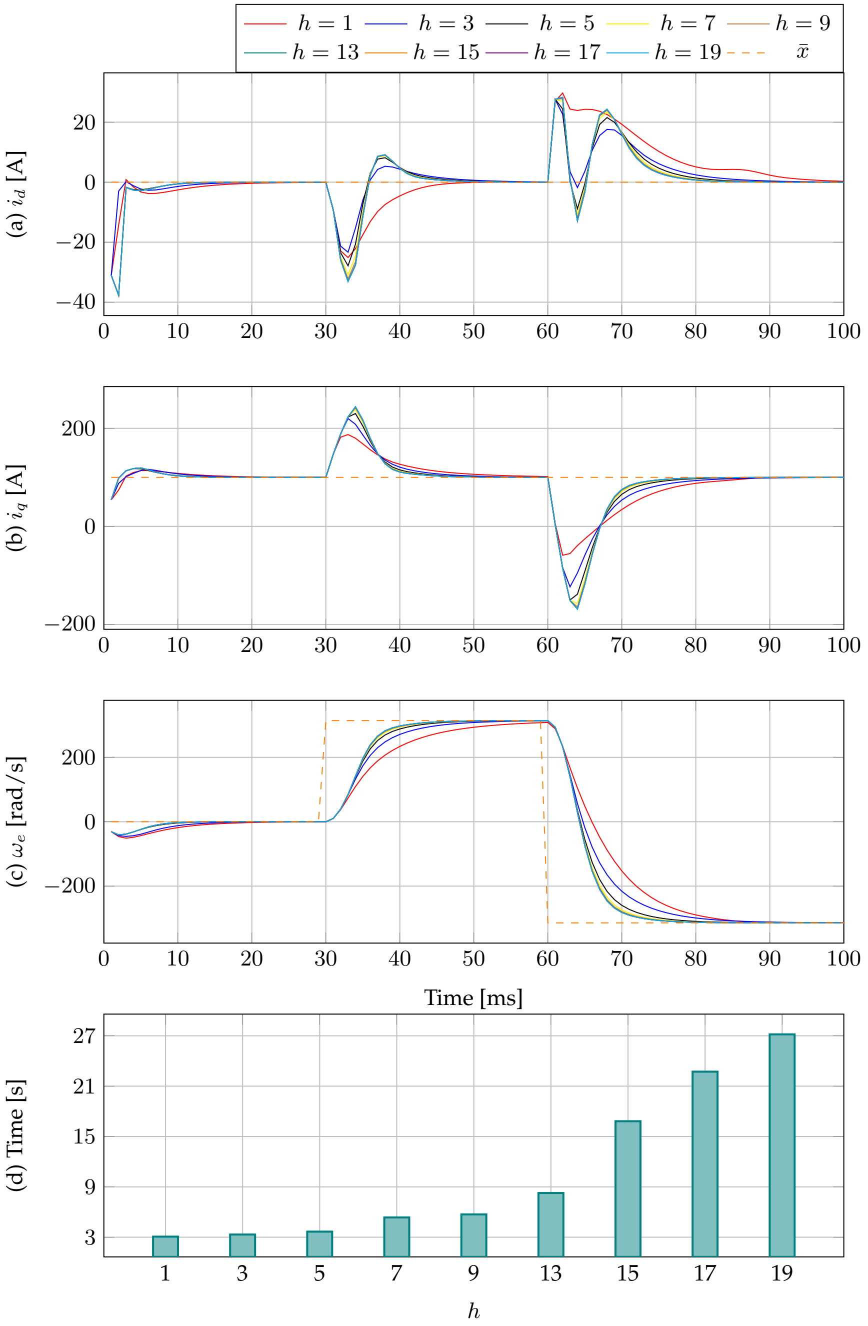

Figure 3. Transient behavior of the proposed control applied to the PMSM under different horizons

increase by about 3.08 and 3.80 times with the inclusion of the passivity constraint in the optimization model for $h = 1$ and $h = 19$, respectively.

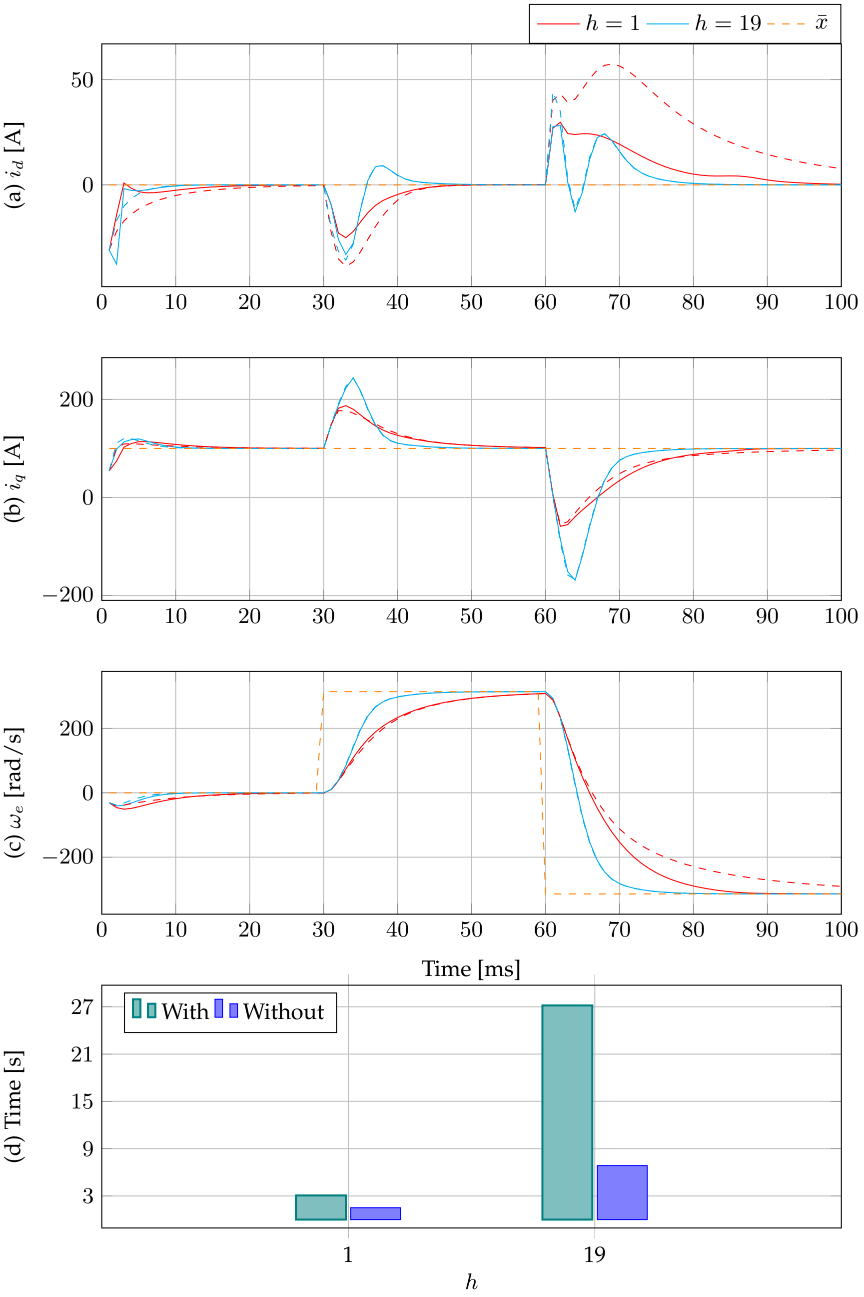

Figure 4. Effect of applying (solid line) or not applying (dashed line) the passivity constraint

Next, the effect of the exponential stability constraint on the optimization model (15) will be analyzed. Fig. 5 presents the dynamic responses of the proposed model with and without the constraint. Figs. 5a and 5b illustrate the stator currents i_d and i_q, respectively. Fig. 5c shows the rotor's electrical rotational speed, and Fig. 5d depicts the simulation times for the prediction horizons $h = 1$ and $h = 19$ with and without the constraint.

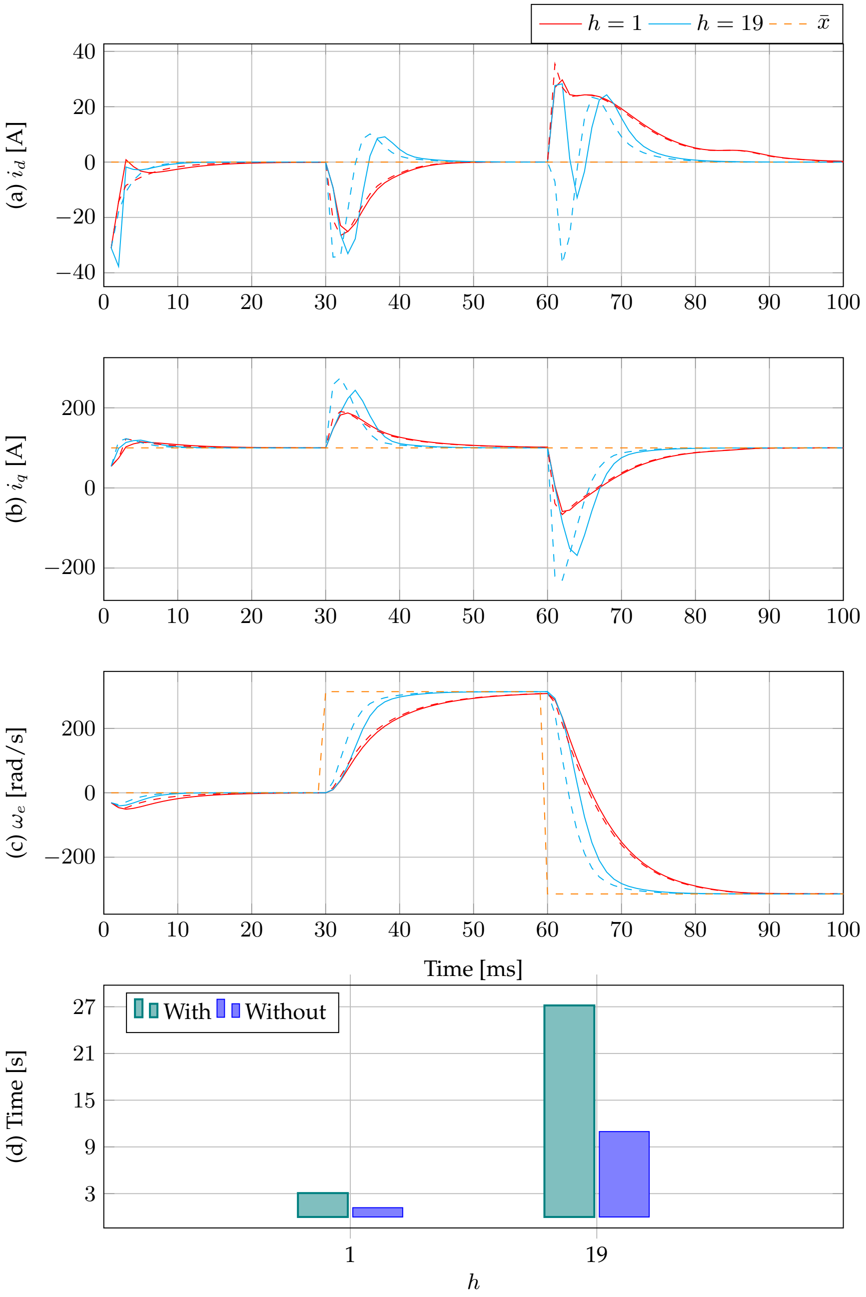

Figure 5. Effect of applying (solid line) or not applying (dashed line) the exponential stability constraint

By analyzing Fig. 5, it can be concluded that the effect of the exponential stability constraint on the proposed control is an increase in simulation times. This effect becomes more pronounced as the prediction horizon increases (Figs. 5b and 5c). Fig. 5d shows that including the constraint increases the simulation time by factors of 2.57 and 2.69 for $h = 1$ and $h = 19$, respectively.

4.3. Results of simulation S_3

This subsection compares the performance of the proposed control against that of the PBS control described in (14). Fig. 6 depicts the dynamic responses of the stator currents (Figs. 6a and 6b) and the rotor's electrical rotational speed (Fig. 3c) for the proposed control and the PBS approach applied to the PMSM. Our proposal was analyzed with the step horizons $h = 1$ and $h = 19$.

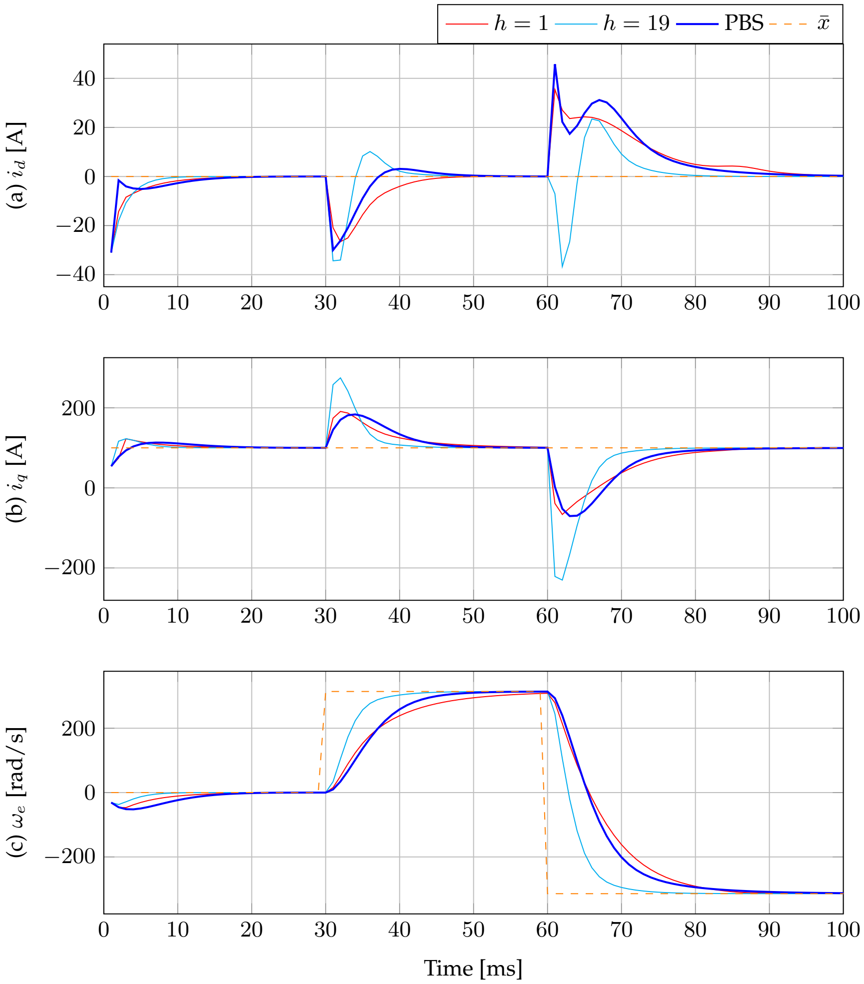

Figure 6. Results of the comparison between the proposed control with $h = 1$ and $h = 19$ and the PBS control

Note that, with $h = 1$, our proposal exhibited a similar performance to that of the PBS control in regulating the motor's speed. However, when the step horizon was increased to $h = 19$, the proposed control reported a faster response time and a quicker settling, indicating a superior performance.

5. Conclusions

This paper presented a valuable contribution to the field of control for permanent magnet synchronous machines. The proposed approach, based on passivity modeling and model-predictive control, represents an innovative and effective method for speed regulation in PMSMs. The results demonstrate that our strategy achieves the desired references in less than 30 ms under various prediction horizons. Furthermore, after five prediction horizons, the dynamic responses of the permanent magnet synchronous motor maintain a similar behavior. However, with a prediction horizon of $h = 1$, the response time takes 10 ms longer on average to stabilize when compared to the other horizons considered. Still, the simulation time for the one-step horizon is the shortest, showing reductions of 42.74 and 88.71 % compared to $h = 7$ and $h = 19$, respectively. This demonstrates that a longer prediction horizon can be more effective in larger systems.

We analyzed the impact of including or excluding the passivity and exponential stability constraints on the proposed control. The results indicated that, for the prediction horizon of one step, the passivity constraint significantly affects the response time of our proposal, slowing down its performance. Conversely, for $h = 19$, the passivity constraint has minimal impact, suggesting that, for longer prediction horizons, the proposed control exhibits a passive behavior. Additionally, including this constraint leads to increased simulation times, *i.e.*, approximately 3.08 and 3.80 times longer for $h = 1$ and $h = 19$, respectively.

On the other hand, the exponential stability constraint decelerated the proposed control, with this effect becoming more noticeable as the prediction horizon grew longer. The inclusion of this constraint increased the simulation times by a factor of 2.57 and 2.69 for $h = 1$ and $h = 19$, respectively.

These findings contribute to the understanding of the factors influencing control performance and provide guidance for the practical implementation of efficient PMSM control systems. In summary, this study underscores the importance of integrating passivity and exponential stability constraints in the advancement of sophisticated control strategies for industrial applications. Finally, a comparison between our proposal and PBS control was conducted, with the former demonstrating a superior performance.

As a future endeavor, the controller could be expanded to various applications, including the regulation of synchronous machines in power systems and voltage source converters. Expanding the controller's scope to these domains would further validate its effectiveness and broaden its practical applicability in various industrial contexts.

6. CRediT author statement

All authors contributed equally to the research.

7. Acknowledgments

This work is a partial result of research project no. 6-24-2, funded by the Research, Innovation, and Extension Vice-Principalship of Universidad Tecnológica de Pereira.

References

[1] V. Yaramasu, B. Wu, P. C. Sen, S. Kouro, and M. Narimani, ”High-power wind energy conversion systems: State-of-the-art and emerging technologies,” *Proc. IEEE*, vol. 103, no. 5, pp. 740-788, 2015. `https://doi.org/10.1109/JPROC.2014.2378692`

[2] I. Sami, N. Ullah, S. M. Muyeen, K. Techato, M. S. Chowdhury, and J.-S. Ro, ”Control methods for standalone and grid connected micro-hydro power plants with synthetic inertia frequency support: A comprehensive review,” *IEEE Access*, vol. 8, pp. 176313-176329, 2020. `https://doi.org/10.1109/ACCESS.2020.3026492`

[3] D. Ramirez, J. P. Bartolome, S. Martinez, L. C. Herrero, and M. Blanco, ”Emulation of an OWC ocean energy plant with PMSG and irregular wave model,” *IEEE Trans. Sustainable Energy*, vol. 6, no. 4, pp. 1515-1523, 2015. `https://doi.org/10.1109/TSTE.2015.2455333`

[4] R. S. Kaarthik, K. S. Amitkumar, and P. Pillay, ”Emulation of a permanent-magnet synchronous generator in real-time using power hardware-in-the-loop,” *IEEE Trans. Transp. Electrification*, vol. 4, no. 2, pp. 474-482, 2018. `https://doi.org/10.1109/TTE.2017.2778149`

[5] K.-W. Hu and C.-M. Liaw, ”Incorporated operation control of DC microgrid and electric vehicle,” *IEEE Trans. Ind. Electron.*, vol. 63, no. 1, pp. 202-215, 2016. `https://doi.org/10.1109/TIE.2015.2480750`

[6] Y. Belkhier *et al.*, ”Interconnection and damping assignment passivity-based non- linear observer control for efficiency maximization of permanent magnet synchronous motor,” *Energy Rep.*, vol. 8, pp. 1350-1361, 2022. `https://doi.org/10.1016/j.egyr.2021.12.057`

[7] X. Liu, H. Yu, J. Yu, and Y. Zhao, ”A novel speed control method based on port-controlled Hamiltonian and disturbance observer for PMSM drives,” *IEEE Access*, vol. 7, pp. 111115-111123, 2019. `https://doi.org/10.1109/ACCESS.2019.2934987`

[8] R. Ortega and E. Garcia-Canseco, ”Interconnection and damping assignment passivity-based control: A survey,” *Eur. J. Control*, vol. 10, no. 5, pp. 432-450, 2004. `https://doi.org/10.3166/ejc.10.432-450`

[9] S. Vazquez *et al.*, ”Model predictive control: A review of its applications in power electronics,” *IEEE Ind. Electron. Mag.*, vol. 8, no. 1, pp. 16-31, 2014. `https://doi.org/10.1109/MIE.2013.2290138`

[10] M. Schwenzer, M. Ay, T. Bergs, and D. Abel, ”Review on model predictive control: An engineering perspective,” *Int. J. Adv. Manuf. Technol.*, vol. 117, no. 5, pp. 1327- 1349, 2021. `https://doi.org/10.1007/s00170-021-07682-3`

[11] M. Khanchoul, M. Hilairet, and D. Normand-Cyrot, ”IDA-PBC under sampling for torque control of PMSM,” *IFAC Proc. Volumes*, vol. 46, no. 11, pp. 15-20, 2013. `https://doi.org/10.3182/20130703-3-FR-4038.00059`

[12] W. Gil-Gonzalez, A. Garces, and O. B. Fosso, ”Passivity-based control for small hydro-power generation with PMSG and VSC,” *IEEE Access*, vol. 8, pp. 153001-153010, 2020. `https://doi.org/10.1109/ACCESS.2020.3018027`

[13] W. Wang, H. Shen, L. Hou, and H. Gu, ”H robust control of permanent magnet synchronous motor based on PCHD,” *IEEE Access*, vol. 7, pp. 49150-49156, 2019. `https://doi.org/10.1109/ACCESS.2019.2893243`

[14] F. Ramirez-Leyva, E. Peralta-Sanchez, J. Vasquez-Sanjuan, and F. Trujillo-Romero, ”Passivity-based speed control for permanent magnet motors,” *Procedia Technol.*, vol. 7, pp. 215-222, 2013. `https://doi.org/10.1016/j.protcy.2013.04.027`

[15] M. Aijaz and K. Sakthivel, ”Neural network based voltage source converter for power management of hybrid energy system,” in *Proc. 2024 Third Int. Conf. Intelligent Tech. Control, Optimization Signal Process. (INCOS)*, pp. 1-7, 2024. `https://doi.org/10.1109/INCOS59338.2024.10527574`

[16] Y. Cao and J. Guo, ”Research on characteristic model-based adaptive control of high-speed permanent magnet synchronous motor with time delay,” *Int. J. Control Autom. Syst.*, vol. 22, no. 2, pp. 460-474, 2024. `https://doi.org/10.1007/s12555-021-0968-1`

[17] Y. Zhang *et al.*, ”Backstepping control of permanent magnet synchronous motors based on load adaptive fuzzy parameter online tuning,” *J. Power Electron.*, pp. 1-12, 2024. `https://doi.org/10.1007/s43236-024-00790-9`

[18] Z. Yin *et al.*, ”Plant-physics-guided neural network control for permanent magnet synchronous motors,” *IEEE J. Sel. Topics Signal Process.*, pp. 1-14, 2024. `https://doi.org/10.1109/JSTSP.2024.3430822`

[19] W. Sun *et al.*, ”Research on efficiency of permanent-magnet synchronous motor based on adaptive algorithm of fuzzy control,” *Sustainability*, vol. 16, no. 3, p. 1253, 2024. `https://doi.org/10.3390/su16031253`

[20] K. Li, J. Ding, X. Sun, and X. Tian, ”Overview of sliding mode control technology for permanent magnet synchronous motor system,” *IEEE Access*, vol. 12, pp. 71685- 71704, 2024. `https://doi.org/10.1109/ACCESS.2024.3402983`

[21] Z. Huang *et al.*, ”Improved active disturbance rejection control for permanent magnet synchronous motor,” *Electronics*, vol. 13, no. 15, p. 3023, 2024. `https://doi.org/10.3390/electronics13153023`

[22] J. Zhu *et al.*, ”Model predictive current control based on hybrid control set for permanent magnet synchronous motor drives,” *IET Power Electron.*, vol. 17, no. 3, pp. 450-462, 2024. `https://doi.org/10.1049/pel2.12657`

[23] D. B. Tchoumtcha, C. T. S. Dagang, and G. Kenne, ”Synergetic control for stand- alone permanent magnet synchronous generator driven by variable wind turbine,” *Int. J. Dyn. Control*, pp. 1-15, 2024. `https://doi.org/10.1007/s40435-024-01384-w`

[24] L. Chen *et al.*, ”Sensorless control of permanent magnet synchronous motor based on adaptive enhanced extended state observer,” *Int. J. Circuit Theory Appl.*, vol. 52, pp. 4303-4322, 2024. `https://doi.org/10.1002/cta.3983`

[25] F. Xiao *et al.*, ”A finite control set model predictive direct speed controller for PMSM application with improved parameter robustness,” *Int. J. Electr. Power Energy Syst.*, vol. 143, p. 108509, 2022. `https://doi.org/10.1016/j.ijepes.2022.108509`

[26] Y. Wang *et al.*, ”Adaptive observer-based current constraint control for permanent magnet synchronous motors,” *IEEE Access*, vol. 11, pp. 91415-91426, 2023. `https://doi.org/10.1109/ACCESS.2023.3289586`

[27] M. Graf, L. Otava, and L. Buchta, ”Simple linearization approach for mpc design for small pmsm with field weakening performance,” *IFAC-PapersOnLine*, vol. 48, no. 4, pp. 159-164, 2015. `https://doi.org/10.1016/j.ifacol.2015.07.025`

[28] Y. Li, C. Zhao, Y. Zhou, and Y. Qin, ”Model predictive torque control of pmsm based on data drive,” *Energy Reports*, vol. 6, pp. 1370-1376, 2020. `https://doi.org/10.1016/j.egyr.2020.11.019`

[29] T. Raff, C. Ebenbauer, and P. Allgower, *Nonlinear Model Predictive Control: A Passivity-Based Approach*. Berlin, Heidelberg, Germany: Springer, 2007.

[30] L. T. Biegler, ”A perspective on nonlinear model predictive control,” *Korean J. Chem. Eng.*, vol. 38, pp. 1317-1332, Jul 2021. `https://doi.org/10.1007/s11814-021-0791-7`

[31] P. Falugi, ”Model predictive control: a passive scheme,” *IFAC Proc*. Vol., vol. 47, no. 3, pp. 1017-1022, 2014. `https://doi.org/10.3182/20140824-6-ZA-1003.02165`

[32] A. Tahirovic and G. Magnani, ”Some Limitations and Real-Time Implementation,” in *Nonlinear Model Predictive Control*, London, UK: Springer, 2013, pp. 41-51. `https://doi.org/10.1007/978-1-4471-5049-7_4`

[33] A. van der Schaft and D. Jeltsema, *Port-Hamiltonian Systems Theory: An Introductory Overview*, vol. 1. London, UK: Now, 2014. `https://doi.org/10.1561/9781601987877`

[34] D. Mayne, J. Rawlings, C. Rao, and P. Scokaert, ”Constrained model predictive control: Stability and optimality,” *Automatica*, vol. 36, no. 6, pp. 789-814, 2000. `https://doi.org/10.1016/S0005-1098(99)00214-9`

[35] W. Haddad and V. Chellaboina, *Nonlinear Dynamical Systems and Control: A Lyapunov-Based Approach*, 2nd ed., Princeton, NJ, USA: Princeton Univ. Press, 2008. `https://doi.org/10.1515/9781400841042`

[36] J. A. E. Andersson, J. Gillis, G. Horn, J. B. Rawlings, and M. Diehl, ”CasADi - A software framework for nonlinear optimization and optimal control,” *Math. Program. Comput.*, vol. 11, no. 1, pp. 1-36, 2019. `https://doi.org/10.1007/s12532-018-0139-4`

Alejandro Garcés-Ruiz

He received his Bachelor (2004) and Master's (2006) degrees in Electric Engineering with on emphasis in Power Systems Optimization from Universidad Tecnológica de Pereira (UTP). After that, he received his PhD in Electrical Engineering from the Norwegian University of Science and Technology (NTNU) in Trondheim, Norway, where he developed a new control for the HVDC integration of offshore wind farms. He currently serves as an associate professor at UTP's Department of Electric Power Engineering. He participated in the study *Smart Grids Colombia, Vision 2030*, which defined the roadmap for implementing smart grids in Colombia. He participates in several groups of CIGRE-Colombia that are related to microgrids and power electronics, as well as in the Colombian Chapter of the Society for Industrial and Applied Mathematics (CoSIAM). His current research interests include mathematical optimization and control for power and energy applications. In 2020, he was awarded the Georg Forster Research Fellowship for Experienced Researchers from the Von Humboldt Foundation in Germany to continue his research about optimization in active distribution systems.

Email: alejandro.garces@utp.edu.co

Walter Gil-González

He received his BSc, MSc, and PhD degrees in Electrical Engineering from UTP (Colombia) in 2011, 2013, and 2019, respectively. He also holds a PhD degree in Renewable Energy from the University of Jaén, Spain, which he obtained in 2024. He worked as an adjunct professor at Institución Universitaria Pascual Bravo. He is currently working as a professor at UTP's Department of Electric Power Engineering. He is a senior member of IEEE and a senior researcher in the National Research System of Colombia. His research interests include power systems control and stability, as well as their optimization and operation.

Email: wjgil@utp.edu.co

UNIVERSIDAD DISTRITAL
FRANCISCO JOSÉ DE CALDAS

Ingeniería

https://revistas.udistrital.edu.co/index.php/reving/issue/view/1241

DOI: https://doi.org/10.14483/23448393.22049

Research

Comparative Analysis of the Julia and AMPL Computational Tools Used in the Radial Distribution Network Optimization Problem

Análisis comparativo de las herramientas computacionales Julia y AMPL utilizadas en el problema de optimización de redes de distribución radiales

Juan Camilo Hoyos Vallejo[1]* and Jaime Quintero Restrepo[1]

[1]Universidad Autónoma de Occidente, Santiago de Cali, Colombia.

Abstract

Context: Research on the development of mathematical models to optimize electric power distribution systems has become increasingly important in recent years. Choosing the right optimization tools and solvers to address optimization problems in these systems has therefore become fundamental.
Method: Nonlinear and mixed-integer nonlinear mathematical models addressing optimal capacitor placement and the allocation of distributed generation were implemented in the AMPL and Julia platforms. These models together with the Ipopt, Knitro, and Bonmin solvers, were tested and compared using 33-, 69-, and 83-bus test systems.
Results: The comparative analysis shows that AMPL allows for a more direct and adequate implementation of this type of optimization problem, while Julia requires more elaborate constructions. The experimental results show significant reductions in system losses through optimal capacitor and distributed generation placement.
Conclusions: AMPL offers a faster learning curve and a syntax that is more suitable for mathematical modeling. On the other hand, Julia provides superior versatility and access to a wider diversity of solvers. Although the evaluated nonlinear solvers proved to be suitable for the non-convex models and reached equivalent solutions, Knitro, a commercial solver, exhibited shorter processing times. In this sense, choosing between free or commercial alternatives involves a compromise between processing times and the available budget. Furthermore, solving the aforementioned optimization problems effectively minimized losses in the test systems. These models are basic versions that can be extended to more complex optimization problems.
Keywords: mathematical optimization, power distribution networks, solvers, optimal capacitor placement, optimal allocation of distributed generation

Article history

Received:
10th /Apr/2024

Modified:
8th /Jul/2024

Accepted:
3rd /Oct/2024

Ing, vol. 29, no. 3, 2024, e22049

---

* **Correspondence:** juan_camilo.hoyos@uao.edu.co

Resumen

Contexto: La investigación sobre el desarrollo de modelos matemáticos para optimizar los sistemas de distribución de energía eléctrica ha cobrado cada vez más importancia en los últimos años. La selección de las herramientas de optimización y *solvers* adecuados para resolver los problemas de optimización en estos sistemas se ha vuelto fundamental.
Método: Se implementaron modelos matemáticos no lineales y no lineales de enteros mixtos para abordar la ubicación óptima de capacitores y generación distribuida en las plataformas AMPL y Julia. Estos modelos, junto con los solvers Ipop, Knitro y Bonmin, fueron evaluados y comparados utilizando sistemas de prueba de 33, 69 y 83 barras.
Resultados: El análisis comparativo evidencia que AMPL permite una implementación más directa y adecuada para este tipo de problemas de optimización, mientras que Julia requiere construcciones más elaboradas. Los resultados experimentales evidencian reducciones significativas en las pérdidas del sistema mediante la ubicación optima de capacitores y generación distribuida.
Conclusiones: AMPL ofrece una curva de aprendizaje más rápida y una sintaxis más adecuada para el modelado matemático. Por otro lado, Julia proporciona una versatilidad superior y acceso a una diversidad más amplia de *solvers*. Aunque los *solvers* no lineales evaluados resultaron adecuados para los modelos no convexos y alcanzaron soluciones equivalentes, Knitro, un *solver* comercial, presentó tiempos de procesamiento más cortos. En este sentido, elegir entre alternativas gratuitas o comerciales implica un compromiso entre los tiempos de procesamiento y el presupuesto disponible. Además, la solución de los problemas de optimización mencionados permitió minimizar de manera efectiva las perdidas en los sistemas de prueba. Estos modelos son versiones básicas que pueden ampliarse a problemas de optimización más complejos.

Palabras clave: optimización matemática, redes de distribución eléctrica, solucionadores, colocación óptima de condensadores, asignación óptima de generación distribuida

Table of contents

1. Introduction

In recent years, research on the development of mathematical models for power systems optimization has gained relevance, leading to a significant increase in publications in the field. These publications have focused on the optimization of electrical power systems, using and solving increasingly sophisticated, complex, and realistic mathematical models through commercial or open-source solvers (1).

Within the scope of electrical distribution networks, modeling and solving optimization problems is fundamental to improving efficiency and reliability. Two areas of interest in this field are optimal capacitor placement and the allocation of distributed generation, with the goal of reducing system losses, improving voltage profiles, correcting power factors, and increasing circuit capacity (2). However, there are issues associated with both the modeling and the optimization tools used in these areas.

Regarding modeling, it is crucial to have accurate mathematical formulations that adequately represent the characteristics and constraints of electrical distribution networks. These formulations must consider the relevant input data, as well as the assumptions and limitations of the optimal capacitor and distributed generation placement problem. The lack of an adequate mathematical formulation can lead to suboptimal or unfeasible solutions in practice (1).

Secondly, the optimization tools used to solve the aforementioned mathematical models are a determining factor in the efficiency and effectiveness of the optimization process (3). In this sense, to evaluate and solve optimization problems in this field, it is critical to analyze the characteristics of the available computational tools, *e.g.*, AMPL and Julia. These tools may offer different characteristics, such as ease of use, documentation availability, support, and flexibility.

In this work, Julia was selected as a high-performance open-source alternative to commercial systems, as well as for its JuMP library, which offers significant advances with regard to modeling and extensibility by taking advantage of several features of Julia that are unique among the programming languages used for scientific computing (4). On the other hand, AMPL was chosen because it facilitates experimenting with formulations and simplifies the use of suitable solvers in addressing optimization problems. Moreover, the notation used in AMPL is close to the typical mathematical notation of state variables, objectives, constraints, sets, and parameters (5).

The commercial and open-source solvers used to tackle optimization problems in distribution networks offer different performance characteristics concerning runtime, documentation and support, solution accuracy, and associated costs (6). Comparing and evaluating these solvers will allow determining the most efficient and suitable ones for solving the optimization problems associated with capacitor and generation placement in distribution grids.

Considering the above, this research conducted a detailed analysis of the free computational tools used to solve the studied problem, comparing the AMPL and Julia platforms with regard to mathematical modeling and optimization, as well as different commercial and open-source solvers. This comparison identified the tools' advantages and limitations, as well as their applicability in specific situations.

2. Mathematical model

This section presents the mathematical models implemented in this article: 1) the power flow model adapted for distribution networks, 2) the model for the optimal placement of capacitors, and 3) the model for the optimal placement of distributed generation. The objective function of each model is presented, as well as the assumptions and constraints involved.

2.1. Power flow

To address the optimal capacitor placement and distributed generation allocation problem, a mathematical power flow model must first be implemented, which constitutes the basis for the subsequent models. This model has the following considerations and is based on the one presented in (7), where some modifications are made to the constraints and parameters presented in (8):

1. The electric power distribution system is represented by a single-phase diagram and features a radial topology.
2. The lines' active and reactive power losses are concentrated at the transmitting bus.
3. The loads are modeled as constant powers.
4. The power flow is unidirectional.
5. The PI model's capacitive reactance of the transmission lines is not considered.
6. There is only one energy supply source (*i.e.*, the substation).

The power flow optimization problem is formulated as the following nonlinear problem (7):

$$\text{minimize } f = K_c \sum_{\forall ij \in \Omega_l} R_{ij} I_{ij}^2 \tag{1}$$

The objective function contains a sum representing the energy losses of the system multiplied by a cost constant K_c. Thus, it is possible to determine the total cost associated with the system's energy losses over a period of one year.

Constraints (2) to (7) are technical and operational equations that seek to replicate the limitations and behavior of the analyzed electrical system.

$$\sum_{\forall ki \in \Omega_l} P_{ki} - \sum_{\forall ij \in \Omega_l} \left(P_{ij} + R_{ij} I_{ij}^2\right) + P_i^s = P_i^d, \quad \forall i \in \Omega_b \tag{2}$$

$$\sum_{\forall ki \in \Omega_l} Q_{ki} - \sum_{\forall ij \in \Omega_l} \left(Q_{ij} + X_{ij} I_{ij}^2\right) + Q_i^s = Q_i^d, \quad \forall i \in \Omega_b \tag{3}$$

$$V_i^2 - 2\left(R_{ij}P_{ij} + X_{ij}Q_{ij}\right) - I_{ij}^2\left(R_{ij}^2 + X_{ij}^2\right) - V_j^2 = 0, \quad \forall ij \in \Omega_l \tag{4}$$

$$I_{ij}^2 V_j^2 = P_{ij}^2 + Q_{ij}^2, \quad \forall ij \in \Omega_l \tag{5}$$

$$I_{\text{min}} \leq I \leq I_{\text{max}}, \quad \forall ij \in \Omega_l \tag{6}$$

$$V_{\text{min}} \leq V \leq V_{\text{max}}, \quad \forall i \in \Omega_b \tag{7}$$

Eq. (2) represents the active power flow balance. In it, the first term denotes the active power injected by all the previous k buses that are connected to node i. The second term denotes the active power extracted towards all the subsequent buses j that are connected to node i and the active power losses of the lines ij through which bus i transmits power. The third term is the active power generated by the substation, where $P_i^s = 0$ for all buses $i \neq 1$, and the fourth term is the active power demand at node i.

Eq. (3) represents the reactive power flow balance. Here, the first term denotes the reactive power injected by all the previous k buses that are connected to node i. The second term denotes the reactive power extracted towards all subsequent buses j connected to node i and the reactive power losses of the lines ij through which bus i transmits power. The third term is the reactive power generated by the substation, where $Q_i^s = 0$ for all buses $i \neq 1$, and the fourth term is the reactive power demand at node i.

Eq. (4) represents the voltage drop for each line ij of the network.

The apparent power flow constraint imposes a technical limit on the apparent power that can be transported by each conductor of the distribution network. Eq. (5) represents this constraint for each line ij.

The inequality constraints represent the permissible technical operating limits of the conductors and equipment in the distribution grid. Eq. (6) models the current constraint in each line ij of the system, aiming to prevent the conductors from overheating above their nominal capacities. Similarly, Eq. (7) defines the permissible voltage standards (9) at each node i, within which the connected equipment can operate safely and reliably.

2.2. Optimal capacitor placement

Capacitor placement optimization can be formulated as the following mixed-integer nonlinear

$$\text{minimize } f = f_1 + f_2 + f_3 \tag{8}$$

problem (2):

where f_1 is Eq. (1) and

$$f_2 = D \sum_{\forall i \in \Omega_b} K_i W_i^{ca} \tag{9}$$

$$f_3 = D \sum_{\forall i \in \Omega_b} K_r Q_i^{ca} \tag{10}$$

The expression in (9) accounts for the installation cost of the capacitor banks K_i. Here, the binary variable W_i^{ca} indicates whether or not the capacitor bank is located at a node i. Eq. (10) describes the cost of each capacitor bank K_r. The variable Q_i^{ca} indicates the reactive power injected by the capacitor at node i, thus providing the acquisition cost of the capacitor banks as a function of the reactive power injected. These two sums are multiplied by a depreciation factor D applied to the installation and acquisition costs of the capacitor banks for a period of one year, respectively.

Considering the reactive power introduced by the fixed capacitor banks in the system, the reactive power balance equation in (3) may be modified as follows:

$$\sum_{\forall ki \in \Omega_l} Q_{ki} - \sum_{\forall ij \in \Omega_l} \left(Q_{ij} + X_{ij} I_{ij}^2\right) + Q_i^s + Q_i^{ca} = Q_i^d, \quad \forall i \in \Omega_b \tag{11}$$

The term Q_i^{ca} in Eq. (11) denotes the reactive power injected by the fixed capacitor banks at each node i of the network.

Finally, constraints are added to the model for optimal capacitor placement.

$$\sum_{\forall i \in \Omega_b} W_i^{ca} \leq N_{\text{max}}^{ca} \tag{12}$$

$$0 \leq N_i^{ca} \leq N_{\text{maxunit}}^{ca} W_i^{ca}, \quad \forall i \in \Omega_b \tag{13}$$

$$Q_i^{ca} = N_i^{ca} Q_{\text{base}}^{ca}, \quad \forall i \in \Omega_b \tag{14}$$

Here, Eq. (12) limits the maximum number of capacitor banks allowed in the distribution network, Eq. (13) stipulates the maximum number of capacitive units that can make up each capacitor bank at a specific node i, and Eq. (14) quantifies the reactive power injected by each capacitor bank at each specific node i.

2.3. Optimal allocation of distributed generation

The problem regarding the optimal allocation of distributed generation can be formulated as the following mixed-integer nonlinear model (2):

$$f = \sum_{\forall ij \in \Omega_l} K_c R_{ij} I_{ij}^2 + D \sum_{\forall i \in \Omega_b} \text{Cost}^{gd} P_i^{gd} \tag{15}$$

The objective function of this model contains two sums: Eq. (1) and the investment cost of distributed generation $Cost^{gf}$ as a function of the active power injected into the system Pi^{gd}. An annual depreciation factor of D is applied to the investment costs, with the purpose of conducting a financial analysis in annualized terms over an evaluation period of ten years.

The following modification is made to the active and reactive power balance of Eqs. (2) and (3), respectively:

$$\sum_{\forall ki \in \Omega_l} P_{ki} - \sum_{\forall ij \in \Omega_l} \left(P_{ij} + R_{ij} I_{ij}^2\right) + P_i^s + P_i^{gd} = P_i^d, \quad \forall i \in \Omega_b \tag{16}$$

$$\sum_{\forall ki \in \Omega_l} Q_{ki} - \sum_{\forall ij \in \Omega_l} \left(Q_{ij} + X_{ij} I_{ij}^2\right) + Q_i^s + Q_i^{gd} = Q_i^d, \quad \forall i \in \Omega_b \tag{17}$$

The terms Pi^{gd} in Eq. (16) and Q_i^{gd} in Eq. (17) denote the active and reactive power injected by the distributed generators at each node i of the network. This modification expands the previous mathematical model by incorporating a new source of active and reactive power into the system. Additionally, constraints are added to the model for the optimal allocation of distributed generation.

$$\sum_{\forall i \in \Omega_b} W_i^{gd} \leq N_{\text{max}}^{gd} \tag{18}$$

$$P_i^{gd} \leq P_{\text{max}}^{gd} W_i^{gd}, \quad \forall i \in \Omega_b \tag{19}$$

$$|Q_i^{gd}| = P_i^{gd} \tan\left(\cos^{-1}(fp)\right), \quad \forall i \in \Omega_b \tag{20}$$

Eq. (18) limits the maximum number of distributed generation units in the network, Eq. (19) quantifies the active power injected by each distributed generation unit into each node i, and Eq. (20) quantifies the reactive power injected by each distributed generation unit into each node i.

The following values, obtained from (8), were considered in 33-, 69-, and 83-bus test systems: K_c was equal to 168 \$USD/kW-year, K_i was 1600 \$USD/bus, K_r was 25 \$USD/kvar, D was 10 %, N_{maxunit}^{ca} was 5, Q_{base}^{ca} was 50 kvar, N_{max}^{ca} and N_{max}^{gd} were 3 for the 33- and 69-bus systems and 5 and 6 for the 83-bus feeder, Cost^{gd} was 1105 \$USD/kW, P_i^{gd} was 100 kW, and fp was 0.92.

3. Computational Implementation

To computationally solve the proposed mathematical models, AMPL and Julia were used. These platforms allow translating the nonlinear equations and constraints of the models into a language that can be processed by a computer in order to find the optimal solution. The implementation process consisted of translating the mathematical formulas of each model into the specific syntax of AMPL and Julia. Due to their characteristics, and although the procedure was similar in both software platforms, some notable differences were observed for each model. The code may be accessed at (10).

3.1. Available documentation

Documentation is essential to guide the user during the implementation of a model. Julia and AMPL provide documentation but differ in approach and content. In Julia, the relevant documentation is in JuMP, a specific library for mathematical modeling, whereas, in AMPL, it is integrated. Therefore, Julia modeling requires consulting JuMP at (11) rather than the general documentation. JuMP's documentation has a collaborative focus that encourages community participation but may cause inconsistencies between versions. AMPL, on the other hand, provides formal documentation developed by its creators. This ensures complete and reliable information, although it limits user feedback. The content focuses on using the platform (12). Moreover, JuMP focuses on language syntax and application, while AMPL also delves into mathematical optimization concepts.

3.2. Data management

Data management in AMPL and Julia coincides in the use of sets to organize information. However, there is a relevant difference in code structuring. While Julia programming is done in a single file, AMPL uses three separate files: one for data, one for the model, and one for program execution. Both software platforms define line and bus sets with associated parameters to manage the input data of the modeled power system (Figs. **1** and **2**). This helps to simplify programming in both AMPL and Julia.

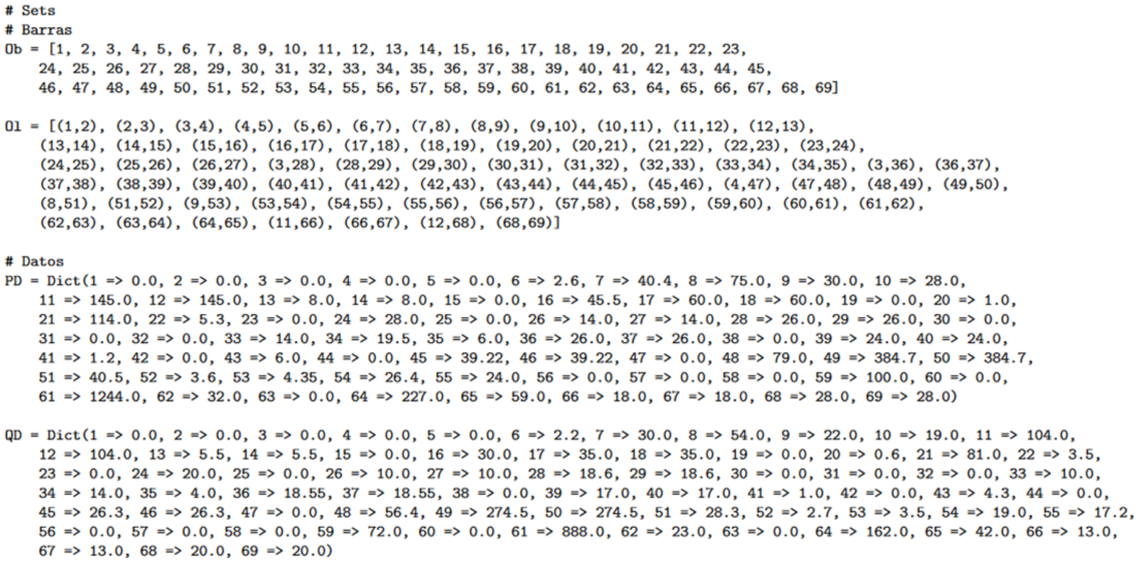

```
# Sets
# Barras
Ob = [1, 2, 3, 4, 5, 6, 7, 8, 9, 10, 11, 12, 13, 14, 15, 16, 17, 18, 19, 20, 21, 22, 23,
    24, 25, 26, 27, 28, 29, 30, 31, 32, 33, 34, 35, 36, 37, 38, 39, 40, 41, 42, 43, 44, 45,
    46, 47, 48, 49, 50, 51, 52, 53, 54, 55, 56, 57, 58, 59, 60, 61, 62, 63, 64, 65, 66, 67, 68, 69]

Ol = [(1,2), (2,3), (3,4), (4,5), (5,6), (6,7), (7,8), (8,9), (9,10), (10,11), (11,12), (12,13),
    (13,14), (14,15), (15,16), (16,17), (17,18), (18,19), (19,20), (20,21), (21,22), (22,23), (23,24),
    (24,25), (25,26), (26,27), (3,28), (28,29), (29,30), (30,31), (31,32), (32,33), (33,34), (34,35), (3,36), (36,37),
    (37,38), (38,39), (39,40), (40,41), (41,42), (42,43), (43,44), (44,45), (45,46), (4,47), (47,48), (48,49), (49,50),
    (8,51), (51,52), (9,53), (53,54), (54,55), (55,56), (56,57), (57,58), (58,59), (59,60), (60,61), (61,62),
    (62,63), (63,64), (64,65), (11,66), (66,67), (12,68), (68,69)]

# Datos
PD = Dict(1 => 0.0, 2 => 0.0, 3 => 0.0, 4 => 0.0, 5 => 0.0, 6 => 2.6, 7 => 40.4, 8 => 75.0, 9 => 30.0, 10 => 28.0,
    11 => 145.0, 12 => 145.0, 13 => 8.0, 14 => 8.0, 15 => 0.0, 16 => 45.5, 17 => 60.0, 18 => 60.0, 19 => 0.0, 20 => 1.0,
    21 => 114.0, 22 => 5.3, 23 => 0.0, 24 => 28.0, 25 => 0.0, 26 => 14.0, 27 => 14.0, 28 => 26.0, 29 => 26.0, 30 => 0.0,
    31 => 0.0, 32 => 0.0, 33 => 14.0, 34 => 19.5, 35 => 6.0, 36 => 26.0, 37 => 26.0, 38 => 0.0, 39 => 24.0, 40 => 24.0,
    41 => 1.2, 42 => 0.0, 43 => 6.0, 44 => 0.0, 45 => 39.22, 46 => 39.22, 47 => 0.0, 48 => 79.0, 49 => 384.7, 50 => 384.7,
    51 => 40.5, 52 => 3.6, 53 => 4.35, 54 => 26.4, 55 => 24.0, 56 => 0.0, 57 => 0.0, 58 => 0.0, 59 => 100.0, 60 => 0.0,
    61 => 1244.0, 62 => 32.0, 63 => 0.0, 64 => 227.0, 65 => 59.0, 66 => 18.0, 67 => 18.0, 68 => 28.0, 69 => 28.0)

QD = Dict(1 => 0.0, 2 => 0.0, 3 => 0.0, 4 => 0.0, 5 => 0.0, 6 => 2.2, 7 => 30.0, 8 => 54.0, 9 => 22.0, 10 => 19.0, 11 => 104.0,
    12 => 104.0, 13 => 5.5, 14 => 5.5, 15 => 0.0, 16 => 30.0, 17 => 35.0, 18 => 35.0, 19 => 0.0, 20 => 0.6, 21 => 81.0, 22 => 3.5,
    23 => 0.0, 24 => 20.0, 25 => 0.0, 26 => 10.0, 27 => 10.0, 28 => 18.6, 29 => 18.6, 30 => 0.0, 31 => 0.0, 32 => 0.0, 33 => 10.0,
    34 => 14.0, 35 => 4.0, 36 => 18.55, 37 => 18.55, 38 => 0.0, 39 => 17.0, 40 => 17.0, 41 => 1.0, 42 => 0.0, 43 => 4.3, 44 => 0.0,
    45 => 26.3, 46 => 26.3, 47 => 0.0, 48 => 56.4, 49 => 274.5, 50 => 274.5, 51 => 28.3, 52 => 2.7, 53 => 3.5, 54 => 19.0, 55 => 17.2,
    56 => 0.0, 57 => 0.0, 58 => 0.0, 59 => 72.0, 60 => 0.0, 61 => 888.0, 62 => 23.0, 63 => 0.0, 64 => 162.0, 65 => 42.0, 66 => 13.0,
    67 => 13.0, 68 => 20.0, 69 => 20.0)
```

Figure 1. Power demand dataset of the 33-bus test system in Julia

3.3. Programming the mathematical model

The main difference between AMPL and Julia lies in their model implementation. Julia is a general programming language with various uses, while AMPL belongs to the family of algebraic modeling and is designed for optimization and mathematical models. This is reflected in its syntax, which can directly and easily translate mathematical models. In contrast, as a complete programming language, Julia has a more complex syntax and requires solid programming foundations for effective use. Figs. **3** and **4** show an example of the computational implementation of Eq. (17) in AMPL and Julia.

Note that the translation of the mathematical model in AMPL is closer to the mathematical formulation of the model, whereas, in Julia, the implementation requires adjusting to its syntax.

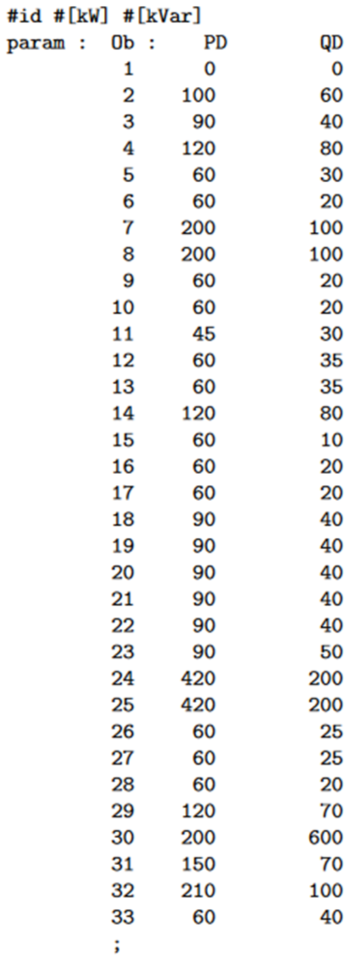

```
#id #[kW] #[kVar]
param :  Ob :    PD        QD
          1      0          0
          2    100         60
          3     90         40
          4    120         80
          5     60         30
          6     60         20
          7    200        100
          8    200        100
          9     60         20
         10     60         20
         11     45         30
         12     60         35
         13     60         35
         14    120         80
         15     60         10
         16     60         20
         17     60         20
         18     90         40
         19     90         40
         20     90         40
         21     90         40
         22     90         40
         23     90         50
         24    420        200
         25    420        200
         26     60         25
         27     60         25
         28     60         20
         29    120         70
         30    200        600
         31    150         70
         32    210        100
         33     60         40
         ;
```

Figure 2. Power demand dataset of the 33-bus test system in AMPL

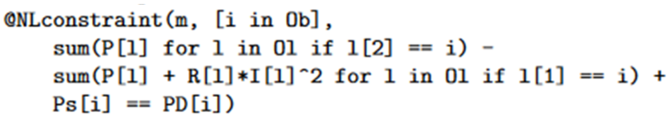

```
@NLconstraint(m, [i in Ob],
    sum(P[l] for l in Ol if l[2] == i) -
    sum(P[l] + R[l]*I[l]^2 for l in Ol if l[1] == i) +
    Ps[i] == PD[i])
```

Figure 3. Computational implementation of Eq. (17) in Julia

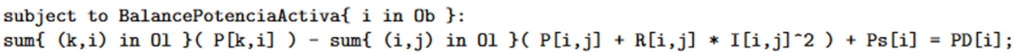

```
subject to BalancePotenciaActiva{ i in Ob }:
sum{ (k,i) in Ol }( P[k,i] ) - sum{ (i,j) in Ol }( P[i,j] + R[i,j] * I[i,j]^2 ) + Ps[i] = PD[i];
```

Figure 4. Computational implementation of Eq. (17) in AMP

3.4. Code length

The code length required for computational implementation is another substantial difference between AMPL and Julia. The structure of AMPL (*i.e.*, one file for data, another for the model, and another for program execution) makes the code length increase considerably. Furthermore, in AMPL, it is mandatory to declare all parameters in an initial section before being able to use them in the data and model specifications. Julia does not have this limitation; as a programming language, it enables more compact programming, keeping all the logic in a single script, without requiring prior declarations or distribution across multiple files. Nevertheless, of required, the user also has this possibility.

3.5. Solver installation

AMPL and Julia differ in solver management. As shown in Fig. 5, AMPL has a centralized portal to install commercial solvers according to the license type and problem, with integrated descriptions to facilitate selection by the user. Open-source solvers come by default. Julia does not have an analogous portal: commercial solvers are obtained from independent pages and open-source solvers as downloadable libraries. This decentralized diversity implies greater complexity in solver selection, as one must investigate the available alternatives online to evaluate features and limitations on an individual basis. Although the process is more complex, it provides access to a broader diversity of solvers. In AMPL, centralized management facilitates selection but limits the available options.

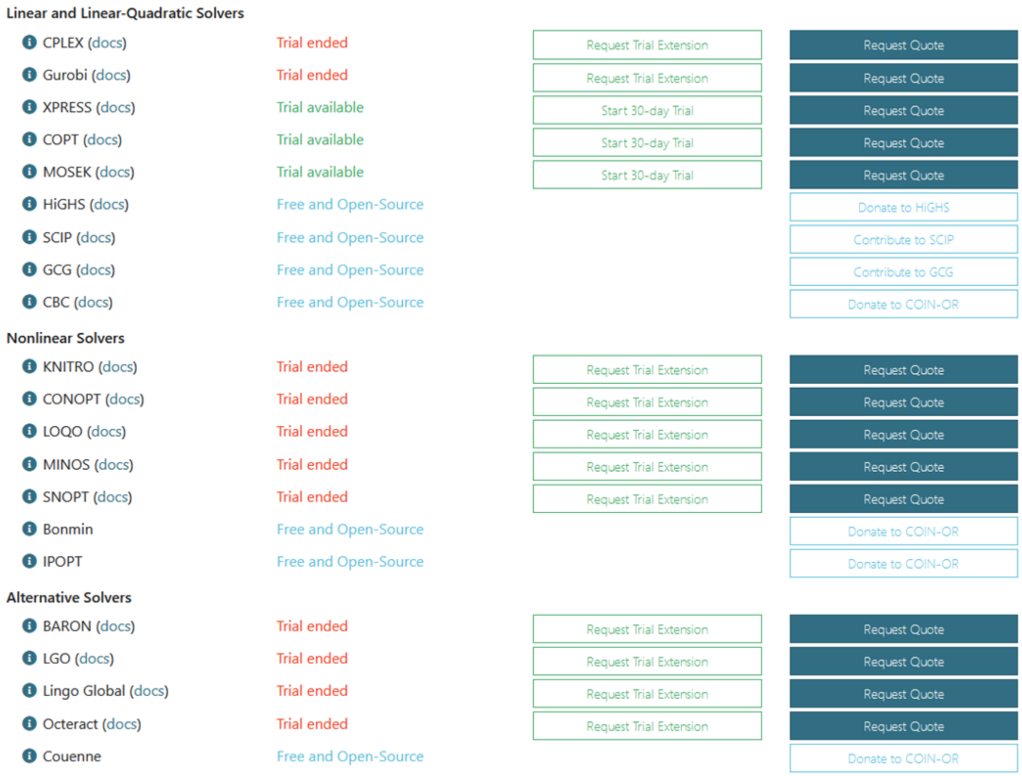

Linear and Linear-Quadratic Solvers			
CPLEX (docs)	Trial ended	Request Trial Extension	Request Quote
Gurobi (docs)	Trial ended	Request Trial Extension	Request Quote
XPRESS (docs)	Trial available	Start 30-day Trial	Request Quote
COPT (docs)	Trial available	Start 30-day Trial	Request Quote
MOSEK (docs)	Trial available	Start 30-day Trial	Request Quote
HiGHS (docs)	Free and Open-Source		Donate to HiGHS
SCIP (docs)	Free and Open-Source		Contribute to SCIP
GCG (docs)	Free and Open-Source		Contribute to GCG
CBC (docs)	Free and Open-Source		Donate to COIN-OR
Nonlinear Solvers			
KNITRO (docs)	Trial ended	Request Trial Extension	Request Quote
CONOPT (docs)	Trial ended	Request Trial Extension	Request Quote
LOQO (docs)	Trial ended	Request Trial Extension	Request Quote
MINOS (docs)	Trial ended	Request Trial Extension	Request Quote
SNOPT (docs)	Trial ended	Request Trial Extension	Request Quote
Bonmin	Free and Open-Source		Donate to COIN-OR
IPOPT	Free and Open-Source		Donate to COIN-OR
Alternative Solvers			
BARON (docs)	Trial ended	Request Trial Extension	Request Quote
LGO (docs)	Trial ended	Request Trial Extension	Request Quote
Lingo Global (docs)	Trial ended	Request Trial Extension	Request Quote
Octeract (docs)	Trial ended	Request Trial Extension	Request Quote
Couenne	Free and Open-Source		Donate to COIN-OR

Figure 5. AMPL's centralized portal

4. Testing and results

For computational experimentation, three optimization algorithms were selected: Knitro, which is commercial in nature, and Bonmin and Ipopt, which are open-source. This choice was based on the fact that these three solvers are available in both Julia and AMPL, and they all implement nonlinear optimization techniques. Therefore, they allow for a comparison between platforms in equivalent non-convex problems. The simulations were performed on a personal computer with an Intel Core™ i-3 1215U CPU @ 1.20 Ghz, 8GB RAM, and the default configuration of the solvers.

4.1. Comparison of results

Tables **I**, **II**, and **III** show the results obtained in the test systems with the selected solvers. Differences were observed in the computational time required by the models' execution, being considerably longer in Julia. This occurs in most of the test systems and proposed optimization problems, except for the 83-bus system's optimal capacitor placement. The above denotes the greater computational efficiency of AMPL over Julia when solving the proposed mathematical models.

Table I. Computation times for the power flow model

Test system	Solver	AMPL computation time (s)	Julia computation time (s)
33-bus	Knitro	0,046875	0,82812500
	Bonmin	0,015625	2,10599995
	Ipopt	0,0625	3,96000004
69-bus	Knitro	0,187	0,48437500
	Bonmin	0,265	3,92599988
	Ipopt	0,109	4,21000004
83-bus	Knitro	0,781	1,60937500
	Bonmin	0,11	3,52600023
	Ipopt	1,625	4,31200036

According to Tables **IV**, **V** and **VI**, across all feeders and optimization models tested for optimal capacitor and distributed generation placement, a decrease in active power losses was observed compared to the initial state of the analyzed electrical networks. Likewise, the results indicate economic viability, as reductions were observed in the total annualized costs, which consider both investment and technical losses.

Additionally, the implementation of the proposed mathematical models made it possible to improve the voltage profiles at the system buses, bringing the values closer to the nominal magnitude as well as mitigating voltage drop issues. This was achieved in both AMPL and Julia, confirming the equivalence of the selected solvers regarding operation and accuracy.

Table II. Computation times for the optimal capacitor placement model

Test system	Solver	Capacitor bank (kvar)	Nodal location	AMPL computation time (s)	Julia computation time (s)
33-bus	Knitro	250	14, 30, 32	1,67188	1,375
	Bonmin	250	14, 30, 32	4,9375	8,77300002
69-bus	Knitro	250	61, 62, 64	0,25	1,078125
	Bonmin	250	61, 62, 64	3,422	3,98300004
83-bus	Knitro	250	8, 9, 10, 11, 72	2,39	1,828125
	Bonmin	250	8, 9, 10, 11, 72	26,172	15,53499985

Table III. Computation times for the model concerning the optimal allocation of distributed generation

Test system	Solver	Distributed generation capacity		Nodal location	AMPL computation time (s)	Julia computation time (s)
		P (kW)	Q (kvar)			
33-bus	Knitro	100	42,5	18, 32, 33	1,64	2,245678
	Bonmin	100	42,5	18, 32, 33	5,098	6,359
69-bus	Knitro	100	42,5	63, 64, 65	0,171	0,5
	Bonmin	100	42,5	63, 64, 65	2,359	4,83699989
83-bus	Knitro	100	42,5	5, 6, 7, 8, 9, 10	0,187	0,53125
	Bonmin	100	42,5	5, 6, 7, 8, 9, 10	2,156	5,33300018

Table IV. Power losses and investment costs for the power flow model

Case	Active power losses (kW)	Total cost per year $USD	$V_{\min}$(p.u)
33-bus	202,5994151	34.036,7017	0,91339845
69-bus	224,828	37.771,1	0,90985
83-bus	423,609	71.166,3	0,943849

Based on the results, it should be noted that the Ipopt solver cannot solve optimization problems with binary variables, since it is designed exclusively for continuous nonlinear programming, where decision variables are continuous in nature. Given that the problems regarding optimal capacitor and distributed generation placement involve binary variables related to the installation of capacitor banks and generators, Ipopt is unable to find a feasible solution.

5. Conclusions

- AMPL, as an algebraic modeling language, exhibits a faster learning curve compared to Julia, a general programming language, since its syntax is specifically designed for a direct and straightforward computational representation of mathematical models.
- It is essential to determine the properties of mathematical models before their computational implementation, including characteristics such as linearity and convexity, among others, in order to select solvers that provide optimal and efficient solutions.
- As the size of the test system increased, the evaluated open-source solvers (Bonmin and Ipopt) exhibited longer execution times compared to the Knitro commercial solver. This indicates the superior scalability of the latter. However, since Bonmin and Ipopt are open source, they do not incur licensing costs, unlike Knitro. This makes them viable alternatives based on the available budget, since solution accuracy was not affected. Thereupon, choosing between free or commercial solvers involves a compromise between processing times and the available economic resources.
- The active power losses observed in the analyzed electrical systems were effectively minimized by implementing the proposed mathematical models for optimal capacitor bank placement and distributed generation allocation. It should be noted that these models can be extended to advanced complexity levels as required. In any case, the accuracy of the solutions largely depends on correctly adjusting the mathematical models according to the particularities of the analyzed electrical system.

Table V. Power losses and investment costs for the optimal capacitor placement model

Case	**Active power losses (kW)**	**Total cost per year $USD**	$V_{\min}$**(p.u)**	**Reduction in active power losses (%)**
33-bus	151,713	27.842,8	0,929413	25,1001618
69-bus	165,187	30.106,4	0,923717	26,52738983
83-bus	392,184	69.811,8841	0,959071	7,42796257

Table VI. Power losses and investment costs for the optimal distributed generation placement model

Case	**Active power losses (kW)**	**Total cost per year $USD**	$V_{\min}$**(p.u)**	**Reduction in active power losses (%)**
33-bus	155,529	26.162,1	0,928202	23,2626297
69-bus	166,535	28.011	0,926195	25,9278204
83-bus	391,631	65.860,3	0,952438	7,55905944

Nomenclature

Table VII. Sets and indices of the models

Ω_l	Sets of lines
Ω_b	Sets of nodes
i	Index of current node
ij	Index of lines
k	Index of the previous node
j	Index of the next node

Table VIII. Model parameters

R_{ij}	Resistance of the network branch ij
X_{ij}	Reactance of the network branch ij
I_{ij}	Current flowing through the network branch ij
I_{max}	Maximum current flowing through the network branch ij
V_{min}	Minimum voltage of node i in the network
V_{max}	Maximum voltage of node i in the network
P_i^d	Active power demanded at node i of the network
Q_i^d	Reactive power demanded at node i of the network
Q_{base}	Base power of the capacitive units
N_{max}^{ca}	Maximum number of capacitor banks in the system
N_{maxunit}^{ca}	Maximum number of capacitive units at each bus
P_{max}^{gd}	Maximum power of the distributed generation unit
fp	Power factor of the distributed generation unit
N_{max}^{gd}	Maximum number of distributed generation units
Cost^{gd}	Investment cost of a distributed generation unit in \$US/kW
K_c	Cost in \$US per kW-year
K_i	Capacitor bank installation cost in \$US
K_r	Cost of each capacitor bank in \$US per kVAr
D	Depreciation factor

Table IX. Model variables

I_{ij}	Minimum current flowing through branch ij
P_{ij}	Active power in branch ij
Q_{ij}	Reactive power in branch ij
V_i	Voltage at node i of the network
P_i^s	Active power generated at the substation
Q_i^s	Reactive power generated at the substation
Q_i^{ca}	Reactive power injected by the capacitor at node i
W_i^{ca}	Binary variable indicating whether a capacitor is installed at node i
N_i^{ca}	Integer variable indicating how many units can be installed at node i
P_i^{gd}	Active power injected by a distributed generation unit at node i
Q_i^{gd}	Reactive power injected by a distributed generation unit at node i
W_i^{gd}	Binary variable indicating whether distributed generation units are installed at node i

6. CRediT author statement

Jaime Quintero Restrepo: conceptualization, investigation, supervision, writing (review and editing)
Juan Camilo Hoyos Vallejo: investigation, software, writing (original draft)

References

[1] R. Dos Reis Gonçalves, "Modelos de programação linear inteira Mista para resolver problemas de Otimização de sistemas de distribuição de Energia elétrica radiais," PhD thesis, Dept. Electrical Eng., Universidade Estadual Paulista, Ilha Solteira, BRA, 2013. [Online]. Available: https://repositorio.unesp.br/items/bd089af3-8e0b-4ee7-a33b-d7f7a42a4170 ↑3

[2] L. A. Gallego Pareja, J. M. Lopez Lezama, and O. Gomez Carmona, "Optimal placement of capacitors, voltage regulators, and distributed generators in electric power distribution systems," *Ingeniería*, vol. 25, no. 3, pp. 334-354, Oct. 2020. https://doi.org/10.14483/23448393.16925 ↑3, 5, 6

[3] A. Karbowski and K. Wyskiel, "Comparative study of AMPL, Pyomo and JuMP optimization modeling languages on a flood control problem example," *Pomiary Automatyka Robotyka*, vol. 25, no. 4, pp. 19-24, Dec. 2021. https://doi.org/10.14313/par_242/19 ↑3

[4] I. Dunning, J. Huchette, and M. Lubin, "JuMP: A Modeling Language for Mathematical Optimization," *SIAM Rev.*, vol. 59, no. 2, pp-295-320, Sep. 2017. https://doi.org/10.1137/15M1020575 ↑3

[5] M.-B. Lucioograndinetti and A. Editors, "Springer proceedings in mathematics & statistics," 2014. [Online]. Available: http://www.springer.com/series/10533 ↑3

[6] R. Anand, D. Aggarwal, and V. Kumar, “A comparative analysis of optimization solvers,” *J. Stat. Manag. Syst.*, vol. 20, no. 4, pp. 623-635, Jul. 2017. `https://doi.org/10.1080/09720510.2017.1395182` ↑3

[7] L. A. Gallego, J. M. López-Lezama, and O. G. Carmona, “A mixed-integer linear programming model for simultaneous optimal reconfiguration and optimal placement of capacitor banks in distribution networks,” *IEEE Access*, vol. 10, pp. 52655-52673, 2022. `https://doi.org/10.1109/ACCESS.2022.3175189` ↑4

[8] J. C. Hoyos Vallejo, “Análisis de herramientas computacionales libres utilizadas en el modelado y en la solución del problema de optimización en la ubicación de capacitores y de la generación en redes de distribución radiales,” Undergraduate Thesis, Dept. Engineering, Universidad Autónoma de Occidente, Cali, Colombia, 2023. [Online]. Available: `https://red.uao.edu.co/handle/10614/15108` ↑4, 7

[9] *Norma Técnica: Calidad de la potencia de redes de distribución*, Empresas Públicas de Medellín, Colombia, 2019, pp.11-12. ↑5

[10] J. C. Hoyos, “Repositorio código AMPL - JuMP.” [Online]. Available: `https://github.com/camilohoyos0499/Code` ↑7

[11] “Documentation for JuMP,” JuMP. [Online]. Available: `https://jump.dev/JuMP.jl/stable/` ↑7

[12] R. Fourer, D. M. Gay, and B. W. Kernighan, “*AMPL: A modeling language for mathematical programming, second edition*,” 2003. [Online]. Available: `https://vanderbei.princeton.edu/307/textbook/AMPLbook.pdf` ↑8

Juan Camilo Hoyos Vallejo

Born in Cali (Valle del Cauca, Colombia). Electrical engineer from Universidad Autónoma de Occidente. His research interests include power systems analysis, optimization, and operation.

Email: juan_camilo.hoyos@uao.edu.co

Jaime Quintero Restrepo

PhD in Electrical Engineering from Washington State University (2005). He is currently a full professor at Universidad Autónoma de Occidente (Cali, Colombia). His research interests include the integration of renewable electricity and power systems stability, security, operation, planning, dynamics, and modeling.

Email: jquintero@uao.edu.co

UNIVERSIDAD DISTRITAL
FRANCISCO JOSÉ DE CALDAS

Ingeniería

https://revistas.udistrital.edu.co/index.php/reving/issue/view/1241

DOI: https://doi.org/10.14483/23448393.21091

Research

Hand Tremor Characterization from a Spatiotemporal Convolutional Representation

Caracterización del temblor de manos a partir de una representación espaciotemporal de carácter convolucional

Jessica Fernanda Pedraza Cadena[1], John Edinson Archila Valderrama[1], Franklin Sierra-Jerez[1], Alejandra Moreno Tarazona[1], and Fabio Martínez Carrillo[1]✉*

[1]Biomedical Imaging, Vision, and Learning Laboratory (BIVL^2 ab), Universidad Industrial de Santander, Bucaramanga, Colombia

Abstract

Context: Parkinson's Disease (PD) is a neurodegenerative disorder related to dopamine deficiency that mainly entails motor conditions such as slowness of movement, postural instability, limb tremor, rigidity, and a decreased range of motion. Tremor, defined as a rhythmic and uncontrolled movement of limbs, is the most prevalent symptom in PD. In the clinical routine, tremors are assessed and quantified by observing the hands following postural and resting patterns. These configurations include voluntary muscular contractions and tremor perception reduction, which leads to noisy signals. The assessments are also subjective and depend on the expertise of professionals to determine whether the tremor is associated with PD.
Method: This work introduces a deep volumetric representation that characterizes PD tremor patterns in resting and postural recording conditions. The strategy includes a convolutional architecture that extracts spatiotemporal patterns correlated with tremor, propagated through different layers until dis- crimination between PD and control subjects is achieved. Moreover, a set of explainability maps is computed by backpropagating output gradients into convolutionally learned spatio-temporal maps.
Results: The method was evaluated on 80 videos (five PD patients and five control subjects), reporting an average accuracy of 92.5 % and a perfect sensitivity score in the postural configuration. As for the resting scheme, the proposed method obtained an average accuracy of 90 % and sensitivity of 80 %.
Conclusions: This approach showed efficacy regarding the localization of tremor patterns, recovering movement information while preserving the spatial and temporal representation. The strategy allows visualizing movement patterns from explainability maps of control subjects and PD patients.

Keywords: tremor, explainability maps, volumetric convolution, resting tremor, postural tremor

Article history

Received:
31fs/Jul/2023

Modified:
23th/Jun/2024

Accepted:
5th/Aug/2024

Ing, vol. 29, no. 3, 2024, e21091

---

*✉ **Correspondence:** famarcar@saber.uis.edu.co

Resumen

Contexto: La enfermedad de Parkinson (EP) es un trastorno neurodegenerativo relacionado con la deficiencia de dopamina que conlleva principalmente afecciones motoras como lentitud de movimientos, inestabilidad postural, temblor de las extremidades, rigidez y disminución del rango de movimiento. El temblor, definido como un movimiento rítmico e incontrolado de las extremidades, es el síntoma más prevalente de la EP. En la rutina clínica, los temblores se evalúan y cuantifican observando las manos siguiendo patrones posturales y de reposo. Estas configuraciones incluyen contracciones musculares voluntarias y reducción de la percepción del temblor, lo que conduce a señales ruidosas. Las evaluaciones también son subjetivas y dependen de la experiencia de los profesionales para determinar si el temblor está asociado a la EP.

Método: Este trabajo introduce una representación volumétrica profunda que caracteriza los patrones de temblor en la EP en condiciones de registro en reposo y posturales. La estrategia incluye una arquitectura convolucional que extrae patrones espaciotemporales correlacionados con el temblor, los cuales se propagan a través de diferentes capas hasta lograr la discriminación entre sujetos con EP y sujetos control. Además, se calcula un conjunto de mapas de explicabilidad retropropagando los gradientes de salida hacia los mapas espaciotemporales aprendidos de forma convolucional.

Resultados: El método fue evaluado en 80 videos (cinco pacientes con EP y cinco sujetos control), reportando una precisión promedio del 92.5 % y una puntuación de sensibilidad perfecta en la configuración postural. En cuanto al esquema en reposo, el método propuesto obtuvo una precisión promedio del 90 % y una sensibilidad del 80 %.

Conclusiones: Este enfoque mostró eficacia en la localización de los patrones de temblor, recuperando información de movimiento mientras preservaba la representación espacial y temporal. La estrategia permite visualizar los patrones de movimiento a partir de mapas de explicabilidad tanto de sujetos control como de pacientes con EP.

Palabras clave: temblores, mapas de explicabilidad, convolución volumétrica, temblor en reposo, temblor postural

Table of contents

Page

1. Introduction

Parkinson's disease (PD) is the second most prevalent neurodegenerative disorder, marked by a deficit in dopamine and impacting about 1 % of individuals aged 60 and older (1). In Colombia, PD has an estimated prevalence of 4.7 per 1000 inhabitants, being more frequent in people over 60 years old (2). Physiologically, PD is associated with a progressive loss of dopamine, a neurotransmitter responsible for optimal and synchronized locomotion processes. Due to this dopamine deficit, motor alterations affect coordinated movements and balance. For instance, postural instability, muscle rigidity, slowness of movement, tremors, and voice involvement constitute the typical symptoms of PD. Tremor is a dominant symptom of this disease. It is a rhythmic and involuntary movement caused by a muscle's reciprocal innervations, which vary in intensity and frequency (3). In approximately 50 % of patients, the cardinal motor is tremor, and only 10 % do not have this symptom. Tremor patterns also vary in frequency and amplitude. Consequently, they can be identified depending on the posture of the limbs and the presence or absence of force. Hence, the detection and characterization of tremors are key to establishing complementary mechanisms to the standardized protocols that allow diagnosing PD.

In clinical practice, resting and postural tremors are commonly evaluated, primarily focusing on amplitude and persistence (4). In the resting configuration, the arms are supported by the muscles or a stable surface, and the tremor is observed during relaxation. Alternatively, the arms are held against gravity at a 90° angle from the body in the postural configuration. In this sense, the physical effort caused by maintaining the arms in this unnatural posture guarantees motion exaggeration. The unnatural position of the arms causes this overload; therefore, these schemes include noisy signals limiting the adequate quantification of hand tremor patterns. Every kind of tremor shows a different range of motion frequency, with resting tremors usually between 4 and 6 Hertz. Meanwhile, postural tremors correspond to the broader range, *i.e.*, between 5 and 12 Hertz (5). Additionally, the movement frequency can be augmented for stress or anxiety and can reduce involuntary movements.

The quantification of tremors is usually performed using technological tools that integrate electronic devices and portable systems (inertial-type sensors), such as accelerometers, gyroscopes, and magnetometers (6). For instance, systems based on inertial sensors placed on the hands and arms quantify velocity and acceleration rates in postural and tremor configurations. Similarly, inertial sensors based on kinematic measures can separate Parkinsonian patterns from control subjects. Complex systems based on the Doppler effect can measure upper limb movements showing frequencies, tremors, and the direction of signal tremors in the range of 0-8 Hz (7). In addition, (8) quantified the acceleration data into a deep learning scheme to quantify the tremor severity. However, these systems require fine calibration to reduce the signal noise, but, in some cases, motion pens reduce the movement amplitude and can be challenging to detect slight motions.

Some works have exploited video techniques to quantify tremor features through non-invasive strategies. Specifically, video has been used indirectly to measure tremors. In this kind of method, the participant holds the camera with their hands in a postural position and places it in front of a common background, which helps to characterize kinematic trajectories (9). However, this method has several drawbacks: it is highly dependent on maintaining a static position of the arm extended at 90 degrees relative to the trunk, which is challenging for healthy participants, and even more so for patients. These additional movements not associated with tremors make it difficult to distinguish between patients and control subjects.

Another example of video techniques involves recording the hands and identifying landmarks, which allows quantifying kinematic characteristics related to amplitude and frequency (10). However, this approach is quite sensitive to noise, as the location of points of interest between frames can vary throughout the video without being associated with tremors. These slight errors add noise to subtle tremors. Additionally, the number of landmarks may lead to a simplification of tremor; a reduced number of landmarks can affect the identification of tremor-associated patterns.

Interestingly, (11) proposed a convolutional neural network (CNN) scheme to codify the tremor severity through a wearable wrist device equipped with an accelerometer and a gyroscope. Here, the collected signals are transformed into the frequency domain and then mapped to the deep net. Furthermore, (8) demonstrated the feasibility of using acceleration data in three directions to quantify tremor severity. This approach measured the arm movements of 20 people performing daily actions like drinking, extending their arms, touching their noses, stacking glasses, drawing, and writing. All the captured signals were then filtered in order to identify voluntary human movements and the severity of tremor patterns through activity classification models (ACM) and tremor assessment models (TEM). Despite these advantages, all these strategies still rely on physical devices that might introduce difficulties associated with sophisticated calibration processes and external noise sources that may bias the recorded measures. Moreover, sensibility is also compromised due to the anti-natural movement caused by the invasive devices.

This work introduces a convolutional spatiotemporal representation able to encode hand tremor patterns associated with PD, which allows distinguishing between Parkinsonian and control patients. This distinction was made separately for both resting and postural configurations. To this effect, hand video sequences were magnified to highlight associated tremors. The hand tremor patterns were then encoded via a hierarchical architecture involving 3D convolutions and embedded dense vectors with motion information. The results showcase the capabilities of this architecture, which provides indices correlated with PD. In addition, explainability maps were computed to support clinical decisions, enabling the visualization of the regions that, according to the network, are associated with a specific prediction.

2. Proposed approach

This work quantifies the spatiotemporal information through a 3D convolution strategy to classify Parkinsonian hand tremors in video sequences. Furthermore, as previously mentioned, explainability maps were computed as a visual tool to support clinical decisions within the deep representation strategy. Fig. **1** illustrates the proposed methodology.

2.1. Deep convolutional 3D architecture

The proposed architecture considers spatial and temporal convolutions to identify spatiotemporal features from video sequences and capture tremor patterns in postural and resting configurations. Specifically, for each layer L, linear transformations are progressively computed, followed by contractive nonlinearities that project the information onto a set of q learned filters expressed as $\Psi_L = \{\Psi\}_{i=1}^{q}$. In this model, $\mathbf{I}(\mathbf{x})_t$ represents a video sequence projected to the first layer by Ψ_1. Then, a representation $\Phi_1(\mathbf{x}) = \sum_{g=1..q} \mathbf{I}(\mathbf{x})_t * \Psi_g$ is obtained, with Ψ_g denoting independently learned convolutional filters. The resulting representation is successively convolved with the filters of the next $N-1$ layers, *i.e.*, $\{\Psi_i\}_{i=2}^{N}$. The convolutional representation $\Phi_1(\mathbf{x})$ is given by the representations of each layer: $\{\Phi_i(\mathbf{x})\}_{i=2}^{N}$. The responses of the first layers yield volumetric low-level features, such as edges and textures. These low-level features build more complex representations in the last convolutional layers. The input to this convolutional network corresponds to video sequences of hand tremors that are densely correlated in successive layers, allowing for the robust modeling of motion patterns. Fig. 1 illustrates the proposed convolutional scheme.

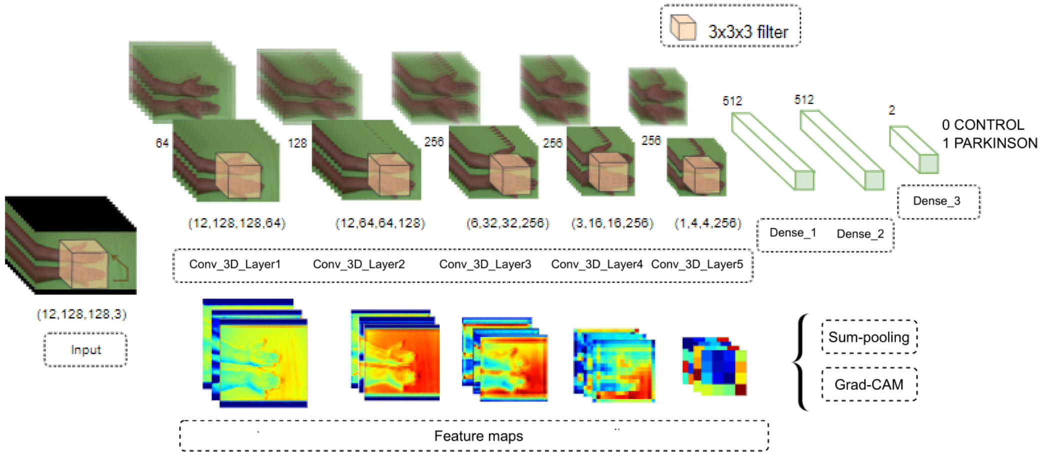

Figure 1. Representation of the proposed methodology. The upper part shows the 3D convolutional architecture, where each row represents different inputs in the network, and the bottom part presents the feature maps of the model

2.2. Explanability maps

Predictive capabilities in clinical settings face challenges associated with the poor interpretability of output predictions. To overcome such limitation, this work implemented a spatio-temporal gradient-weighted class activation mapping (Grad-CAM) approximation as an alternative visualization tool to support PD predictions (Fig. 2). Particularly, Grad-CAM maps were adapted to the volumetric responses of the different 3D convolutional layers in the proposed architecture. This strategy generates a heat map, highlighting the critical regions in a specific network input by means of the gradient information that flows from a certain output probability to a specific convolutional layer in the proposed CNN. To obtain the discriminant location map regarding the class c and an input video, the gradient of the probability score of that class (y^c) is first computed with respect to the A^k feature maps of a convolutional layer. These backward-flowing gradients are spatially averaged to obtain the weights α_k^c.

$$\alpha_k^c = \frac{1}{Z}\sum_i \sum_j \frac{\partial y^c}{\partial A_{ij}^k} \tag{1}$$

Where $\frac{1}{Z}\sum_i \sum_j$ is the global average pooling, and $\frac{\partial y^c}{\partial A_{ij}^k}$ denotes the gradients via backpropagation. After calculating the weights for the target class c, a weighted combination of activation maps is followed by a rectified linear unit (ReLU). The ReLU is applied to the linear combination since only the features that positively influence the class are of interest, and it highlights the associated regions as follows:

$$L_{Grad-CAM}^c = ReLU(\sum_k \alpha_k^c A^k) \tag{2}$$

where $(\sum_k \alpha_k^c A^k)$ is the linear combination. Finally, an upsampling guarantees the same resolution as the original image.

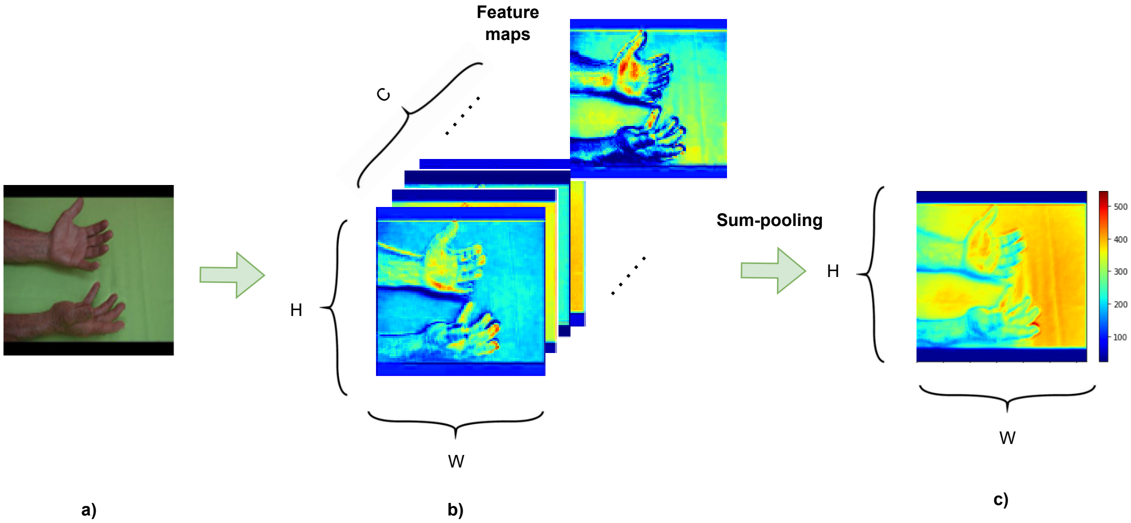

Figure 2. Sum-pooling strategy for feature maps in a convolutional layer: a) input image, b) feature maps of a given convolutional layer, c) sum-pooling

3. Experimental setup

3.1. Data

This study included a total of ten participants: five control subjects (average age: 72,2 ± 8 years) and five patients with PD (average age: 72,3 ± 9 years). The patients had been diagnosed at the second stage of the disease by a physician who used the standard protocols of the Hoehn-Yahr scale. The

Ethics Committee of Universidad Industrial de Santander approved this study, and a written informed consent was obtained from all the participants. Data recording was made possible thanks to Fundación del Adulto Mayor y Parkinson en Santander (FAMPAS) and the Biomedical Imaging, Vision, and Learning Laboratory (BIVL^{2}ab research group). The protocols followed for the tremor configuration are detailed below.

A camera was placed on a tripod at a 45° angle, and a green background was used to highlight the hands. Additionally, a semi-controlled environment was used to avoid external brightness artifacts. The participant was seated in a comfortable position to prevent any additional movements that were not associated with tremors. The test configurations are detailed below.

- In the resting configuration, the hands were supported by a table with a green background, and the palms were relaxed in an upward position. During the recording, some questions were asked to the participants, diverting their focus from tensing their hands to prevent the tremor.
- In the postural configuration, the hands were held above the surface without touching it, with the palms facing downward.

3.2. Parameter tuning

The proposed approach was adjusted at different stages in order to optimize the representation with regard to the description and quantification of PD patterns. According to each stage, the following parameters were set:

Temporal Sequences: Different temporal sequence lengths (F) were considered, where $F = \{8, 12, 16, 24\}$ frames per video. Considering that each video lasts between 12 and 15 seconds, the number of frames taken represents different frequencies associated with the motion.

Spatio-temporal network: The spatio-temporal contribution was considered with three and five 3D convolutional layers. Additionally, the performance of one or two dense layers was considered. The fully connected layers were ReLU-activated. A dropout rate of 0.5 was established, which is an effective mechanism to avoid over-fitting.

Training configuration: The model was trained using the Adam optimizer, with an initial learning rate of 0.001. A scheduler was employed to reduce the learning rate by a factor of 0.1 if the validation losses did not improve for five consecutive epochs. The loss function used was the categorical cross-entropy, with L2 regularization to prevent over-fitting. The training lasted 20 epochs, with early stopping based on validation loss, applying a patience of eight epochs. A batch size with the same number of frames per video was selected (*i.e.*, $8, 12, 16, 24$).

3.3. Experimental configuration

To evaluate the performance of the proposed approach, leave-one-patient-out cross-validation was carried out with the hand tremor dataset. At each iteration, one patient was left out for testing, and the remaining ones (nine subjects in this case) were used for training. For these experiments, the correctly classified Parkinsonian patients were counted as true positives (TP), and the control patients were identified as true negatives (TN). Then, the following set of metrics was used to fully understand the performance of the approach in its different configurations: sensitivity ($sen = \frac{TP}{TP+FN}$), accuracy ($acc = \frac{TP+TN}{TP+FP+FN+TN}$), precision ($prec = \frac{TP}{TP+FP}$), and the F1 score ($F_1 = \frac{2\times prec\times sen}{prec+sen}$).

4. Evaluation and results

The proposed approach aims to achieve proper differentiation between control and PD patient groups regarding hidden tremor patterns in standard video sequences recorded in postural and resting hand configurations. For validation, the videos were projected in two different versions: raw and magnified sequences. The latter were obtained after applying a temporal filter that highlights key frequencies related to PD. Particularly, classical Euler magnification (12) was employed as a pre-processing stage.

A first validation was carried out with the aim of selecting the best temporal sequence length to discriminate between PD and control patients. Fig. 3 illustrates the model's performance in terms of accuracy and the F1 score. To perform an ablation study, the video clips were downsampled to $F = [8, 12, 16, 24]$ frames per video. As expected, a low frame representation level led to poor spatiotemporal video patterns. On the other hand, through a medium frame representation (12), the model achieved the best results, given its compact tremor feature characterization. It is important to note that these videos were recorded within a range of 12-15 seconds and at a typical PD tremor frequency (13). Consequently, the proposed approach shows potential in distinguishing between control subjects and patients with mild tremors in the early stages of the disease. The differentiation capabilities of full video frames were limited due to redundancy between frames.

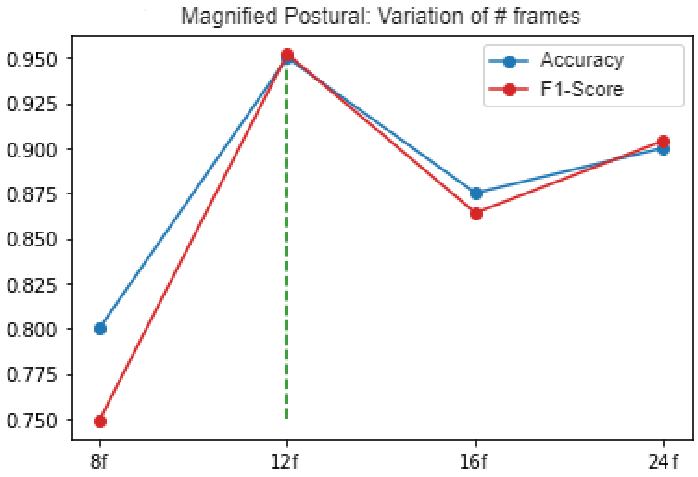

Figure 3. Frame variation for the best architecture configuration. The x-axis shows the frame variation, while the y-axis shows the accuracy values and the F1 score (blue and red lines, respectively)

Secondly, the spatiotemporal network's contribution was analyzed while considering three and five 3D convolutional layers, varying the number of dense layers and their corresponding number of units. Fig. 4 illustrates the network's performance concerning accuracy and the F1 score in standard and magnified video sequences for both configurations. As expected, the best model performance was achieved through the deepest configuration (five convolutional layers and two dense layers with 2048 units). This behavior reinforces the hypothesis that hidden hand tremors could be properly coded along the temporal dimension. Nevertheless, it is important to note that a deeper configuration alone is not enough: the 5C+Dense net configuration always reports the worst performance and is even surpassed by the standard 3C setup. In this vein, an additional dense layer offers a suitable spatiotemporal representation.

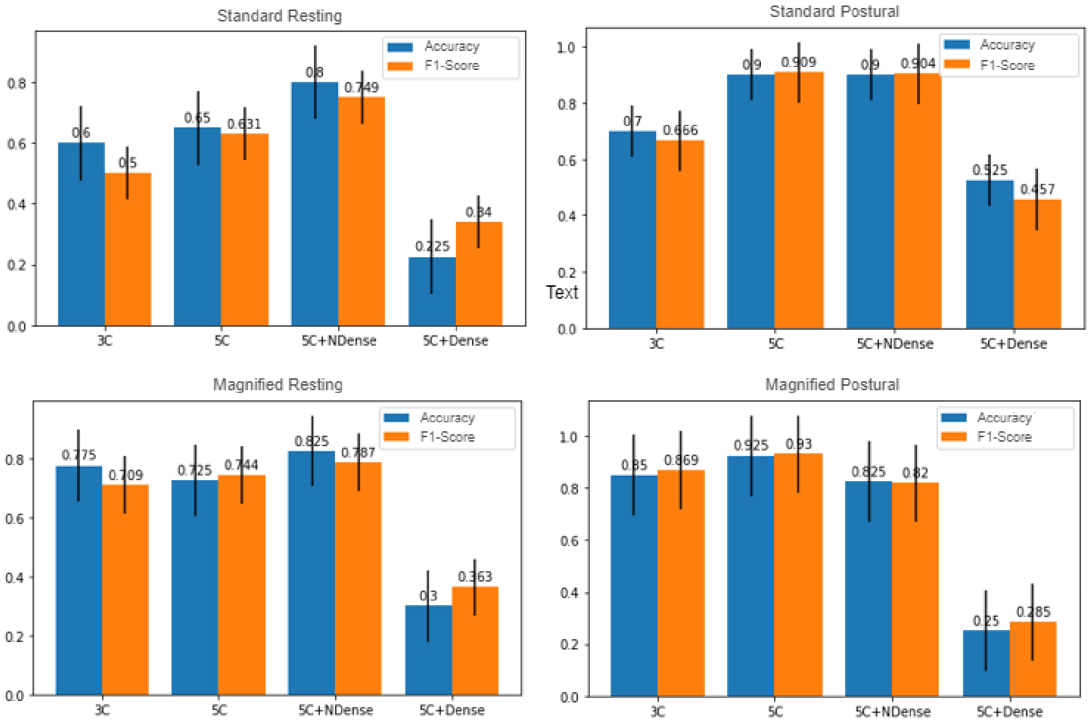

Figure 4. Model performance with respect to variations in the number of convolutional and dense layers. From left to right, model performance for the resting and postural configurations. From top to bottom, model performance concerning standard and magnified video sequences

Additionally, Table I shows a detailed metric evaluation of the best model configuration for each type of video sequence. As expected, the magnified postural configuration obtained the highest F1, sensitivity, and accuracy scores. In such cases, a major effort of the limbs increases the physical effort required to keep the arms in a fixed position, which contributes to a natural exaggeration of the tremor, which may even reveal patterns that cannot be observed in the resting configuration. Particularly, tremors are more constant in the postural configuration, given the muscular effort required to maintain a posture against gravity. Thus, amplifying these standard movements significantly improves the model's performance.

Interestingly enough, a perfect precision score was obtained under the resting hand configuration without magnification. This may be associated with the digital noise introduced by the synthetic exaggeration caused by optical magnification, *i.e.*, control movements not associated with Parkinsonian patterns may be exaggerated, resulting in reduced precision and accuracy. Euler magnification is subject to a global constraint that may increase the dynamic noise of video sequences, even surpassing patients' natural tremor. From a clinical perspective, it is important to use video materials that provide a clearer and less ambiguous signal. In this vein, standard resting videos are less prone to model misinterpretation than magnified ones. In light of the above, the proposed scheme yields promising results in distinguishing PD patients from control subjects, minimizing the false positive rate. It could be regarded as a potential clinical tool to support medical decisions while only requiring standard video sequences. Specifically, it could potentially discriminate between two types of tremors observed in clinical practice, *i.e.*, postural and resting tremors. In this context, a differentiated diagnosis of tremors could support the development of more personalized treatments, thereby improving the patient's quality of life (14).

Complementarily, Fig. 5 shows the training adjustment performed for the postural magnified configuration architecture. It can be observed that accuracy increases while losses decrease consistently for all folds until a stable configuration is reached. Also note that, in the first epochs, there are remarkable variations in the results and the stabilization of losses. Nonetheless, as the number of epochs increases, these variations are significantly reduced, showing a greater confidence in the results.

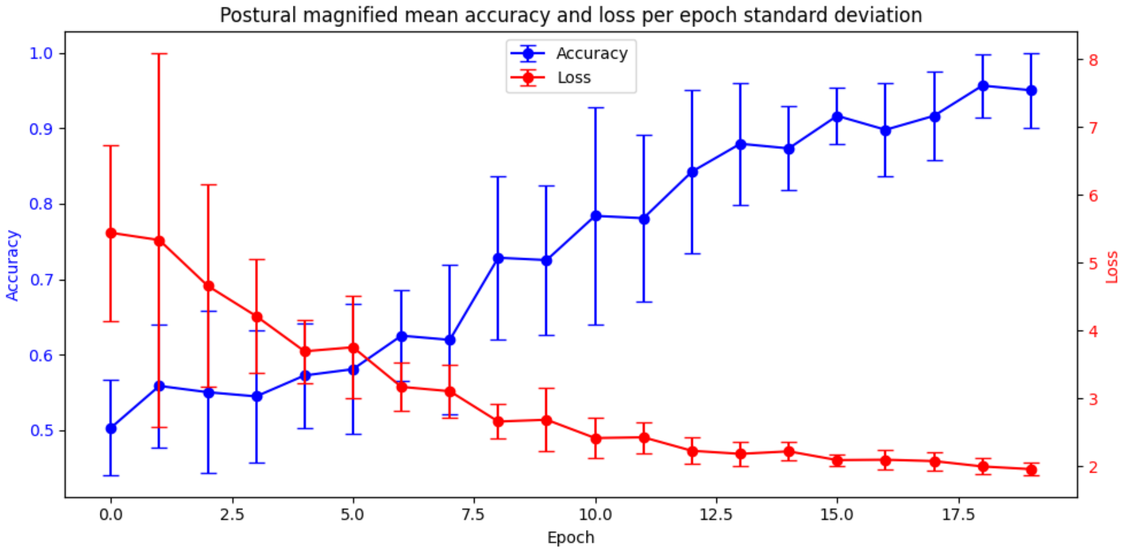

Figure 5. Training for the magnified postural architectures through k-fold cross-validation. This plot shows the mean accuracy and losses values achieved during each epoch, together with their variance (vertical lines).

As a second phase in the validation and evaluation of the proposed methodology, explainability maps were calculated to interpret and support the predictions. Notably, Grad-CAM offers weighted

Table I. Model performance across different video configurations

	Accuracy	**F1 score**	**Precision**	**Sensitivity**
Standard postural	0.700	0.666	0.750	0.600
Standard resting	0.900	0.888	**1**	0.800
Magnified postural	**0.925**	**0.930**	0.869	**1**
Magnified resting	0.675	0.697	0.652	0.750

volumetric visualization across different video regions, with a strong influence on the decision. Fig. 6 shows the Grad-CAM algorithm employed for the same magnified sequences of control and PD patients. Our proposal suggests the palms of the hands as the main regions to achieve control predictions. Even more interesting is the fact that, for the PD patients, the model seems to focus on the boundary regions of the hands, which are prone to slight movements. These regions are associated with a greater perception of tremors (mainly the fingertips). It can thus be assumed that convolutional bank filters computed from 3D convolutional kernels pay attention to the subtle motion of the hand and the arm. In fact, the prediction weighted with such activation shows an association with tremors. In clinical practice, there is a phenomenon called *pill-rolling*, wherein the patient's tremor is predominantly observed in the thumb and forefinger (15). Notably, with an early diagnosis of this condition, the symptoms of PD can be alleviated through medication and physical therapy, helping the patient to regain independence. In this vein, the proposed approach exhibits a robust behavior in codifying hidden hand tremors in regions that are most sensitive to the patient's movement in both resting and postural configurations.

5. Conclusions and future work

Nowadays, PD diagnosis strongly depends on tremor observations based on medical expertise. These observations only consider strong changes in motion, which hinders the monitoring of PD progression given the high variance in the amplitude and frequency associated with the motion of a particular patient (16). To overcome this issue, this work presented a deep volumetric strategy that represents postural and tremor configurations through video sequences, with the purpose of identifying tremors associated with PD. The strategy included a convolutional architecture that extracts spatiotemporal patterns correlated with tremors and propagates them through different layers until PD and control subjects are distinguished from each other. In addition, explainability maps were computed by backpropagating output gradients into convolutionally learned spatiotemporal maps.

This approach was tested with five patients and five control subjects, for a total of 80 video sequences, showing promising results for predicting PD from video. The two studied configurations were seen to be complementary, demonstrating the importance of using both in clinical practice. Magnified postural patterns can contribute to a greater classification sensitivity, and standard resting videos can increase precision. However, some prediction errors were observed, which may be associated with the high variability in the intensity and frequency of the patients' tremors. Particularly, in patients with early signs of the disease, the tremors were less pronounced and less consistent throughout the

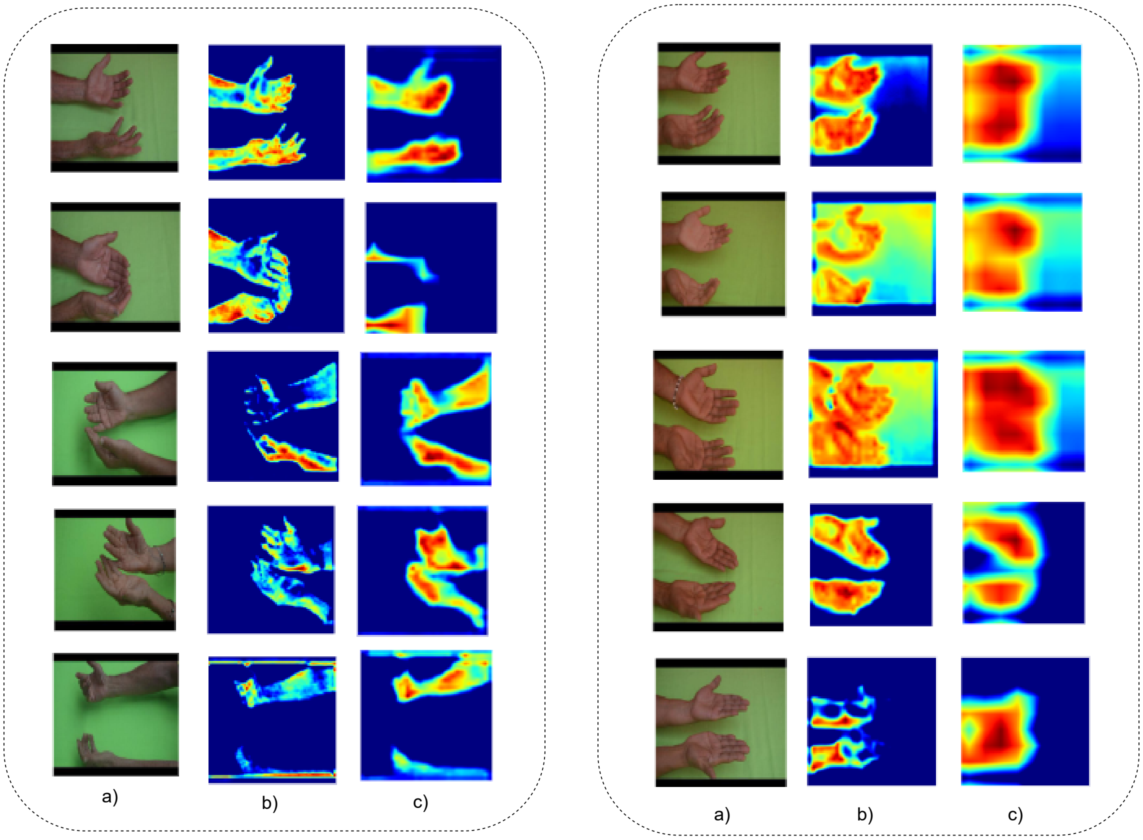

Parkinson's patients

Control patients

Figure 6. Heat maps obtained using the Grad-CAM algorithm. From left to right, PD and control subjects. Columns **a**, **b**, and **c** show the input and the response maps of the third and fourth convolutional layers, respectively

video, especially in resting configurations. In such cases, processing the video samples and adequately classifying the patients concerning the control population become challenging tasks. Despite these limitations, postural effort was seen as appropriate for indicating abnormal patterns associated with PD. Moreover, processing raw videos of the resting configuration tests was more effective than using optical Eulerian magnification. The proposed 3D convolutional network is able to capture localized tremors without any optical exaggeration, providing an accurate and useful representation for the classification model. This is in line with the preference for standard video configurations in the context of medical diagnostics, where precision and reliability are critical.

The results of the proposed approach are very descriptive, highlighting its potential to support observational analysis by enabling the identification of spatiotemporal regions with stronger associations to tremors. Therefore, the explainability maps of the control subjects show a focus on the palm as opposed to those of the patients, which reveal a focus, for instance, on the thumb and the fingertips. The results suggest a potential link between the pill-rolling PD tremor (a tremor of the thumb and the index finger) and the explainability maps. Our approach was validated by studying a reduced number of subjects, given the difficulties in acquiring data from more patients. The main issue concerning data is the ability to quantify populations with comparable demographic characteristics in order to develop approaches that allow representing and classifying disease patterns.

In light of the above, we propose further validation with larger datasets and patients stratified according to the stages of the disease. This may be useful to identify new motion patterns that contribute to the precision of clinical predictions in relation to PD progression or the effectiveness of a particular treatment. Furthermore, the inclusion of new cardinal symptoms might improve the representation and the tool's impact on diagnostic support.

6. Acknowledgements

This work was supported by Vicerrectoría de Investigación y Extensión (VIE) of Universidad Industrial de Santander through the project titled *Quantification of prostate lesions by comparing multi- and biparametric MRI sequences via artificial intelligence tools*, with code 3946.

7. CRediT author statement

All authors contributed equally to the research.

References

[1] Z. Ou, J. Pan, S. Tang, D. Duan, D. Yu, H. Nong, and Z. Wang, "Global trends in the incidence, prevalence, and years lived with disability of parkinson's disease in 204 countries/territories from 1990 to 2019," *Front. Public Health*, vol. 9, p. 776847, 2021, https://doi.org/10.3389/fpubh.2021.776847. 3

[2] A. Castro Toro and O. F. Buriticá, "Enfermedad de Parkinson: criterios diagnósticos, factores de riesgo y de progresión, y escalas de valoración del estadio clínico," *Acta. Neurol. Colomb.*, vol. 30, no. 4, pp. 300–306, 2014, https://www.actaneurologica.com/index.php/anc/article/view/79. 3

[3] J. Pasquini, G. Deuschl, A. Pecori, S. Salvadori, R. Ceravolo, and N. Pavese, "The clinical profile of tremor in parkinson's disease," *Mov. Disord. Clin. Pract.*, vol. 10, no. 10, pp. 1496–1506, 2023, https://doi.org/10.1002/mdc3.13845. 3

[4] B. Kilinc, N. Cetisli-Korkmaz, L. S. Bir, A. D. Marangoz, and H. Senol, "The quality of life in individuals with parkinson's disease: Is it related to functionality and tremor severity? A cross-sectional study," *Physiother. Theory. Pract.*, pp. 1–10, 2023, https://doi.org/10.1080/09593985.2023.2236691. 3

[5] K. P. Bhatia *et al.*, "Consensus statement on the classification of tremors from the task force on tremor of the international parkinson and movement disorder society," *Mov. Disord.*, vol. 33, no. 1, pp. 75–87, 2018, https://doi.org/10.1002/mds.27121. 3

[6] L. P. Sánchez-Fernández, L. A. Sánchez-Pérez, P. D. Concha-Gómez, and A. Shaout, "Kinetic tremor analysis using wearable sensors and fuzzy inference systems in parkinson's disease," *Biomed. Signal Process Control*, vol. 84, p. 104748, 2023, https://doi.org/10.1016/j.bspc.2023.104748. 3

[7] C.-H. Lin, J.-X. Wu, J.-C. Hsu, P.-Y. Chen, N.-S. Pai, and H.-Y. Lai, "Tremor class scaling for parkinson disease patients using an array x-band microwave doppler-based upper limb movement quantizer," *IEEE Sens. J.*, vol. 21, no. 19, pp. 21 473–21 485, 2021, https://doi.org/10.1109/JSEN.2021.3103803. 3

[8] X. Zheng, A. Vieira, S. L. Marcos, Y. Aladro, and J. Ordieres-Meré, "Activity-aware essential tremor evaluation using deep learning method based on acceleration data," *Parkinsonism. Relat. Disord.*, vol. 58, pp. 17–22, 2019, https://doi.org/10.1016/j.parkreldis.2018.08.001. 3, 4

[9] S.-H. Lee, D. Lee, J. Park, J.-M. Shim, and B. Kim, "Quantification of tremor dynamics via video-based analysis," *Multimed. Tools Appl.*, pp. 1–19, 2024, https://doi.org/10.1007/s11042-024-18438-y. 3

[10] M. U. Friedrich *et al.*, "Validation and application of computer vision algorithms for video-based tremor analysis," *NPJ Digit. Med.*, vol. 7, no. 1, p. 165, 2024, https://doi.org/10.1038/s41746-024-01153-1. 4

[11] H. B. Kim *et al.*, "Wrist sensor-based tremor severity quantification in parkinson's disease using convolutional neural network," *Comput. Biol. Med.*, vol. 95, pp. 140–146, 2018, https://doi.org/10.1016/j.compbiomed.2018.02.007. 4

[12] H.-Y. Wu, M. Rubinstein, E. Shih, J. Guttag, F. Durand, and W. T. Freeman, "Eulerian video magnification for revealing subtle changes in the world," *ACM Trans. Graph. (Proc. SIGGRAPH 2012)*, vol. 31, no. 4, 2012, https://doi.org/10.1145/2185520.2335416. 8

[13] A. Gironell, B. Pascual-Sedano, I. Aracil, J. Marín-Lahoz, J. Pagonabarraga, and J. Kulisevsky, "Tremor types in parkinson disease: a descriptive study using a new classification," *Parkinson's Dis.*, vol. 2018, no. 1, p. 4327597, 2018, https://doi.org/10.1155/2018/4327597. 8

[14] E. D. Louis, "Tremor," *Continuum (Minneap. Minn.)*, vol. 25, no. 4, pp. 959–975, 2019, https://doi.org/10.1212/CON.0000000000000748. 10

[15] H. Zach, R. Bloem, and R. C. Helmich, "Parkinson's tremor: Effects of dopamine and cognitive load," Ph.D. dissertation, Radboud Univ., 2023, https://www.researchgate.net/publication/368568080_Parkinson's_tremor-_effects_of_dopamine_and_cognitive_load_HZach. 11

[16] H. Zach, M. Dirkx, B. R. Bloem, and R. C. Helmich, "The clinical evaluation of parkinson's tremor," *J. Parkinson's Dis.*, vol. 5, no. 3, pp. 471–474, 2015, https://doi.org/10.3233/JPD-150650. 11

UNIVERSIDAD DISTRITAL
FRANCISCO JOSÉ DE CALDAS

Ingeniería

https://revistas.udistrital.edu.co/index.php/reving/issue/view/1241

DOI: https://doi.org/10.14483/23448393.21135

Research

Advanced Neural Model for Spanish Spell-Checking

Modelo neuronal avanzado para corrección ortográfica en español

Eduard Gilberto Puerto Cuadros[1]*

[1]Universidad Francisco de Paula Santander, Cúcuta, Colombia.

Abstract

Context: Correcting spelling errors in written content, particularly in Spanish texts, remains a critical challenge in natural language processing (NLP) due to the complexity of word structures and the inefficiency of existing methods when applied to large datasets.

Method: This paper introduces a novel neural model inspired by the brain's cognitive mechanisms for recognizing and correcting misspelled words. Through a deep hierarchical framework with specialized recognition neurons and advanced activation functions, the model is designed to enhance the accuracy and scalability of spelling correction systems. Our approach not only improves error detection but also provides context-aware corrections.

Results: The results show that the model achieves an F-measure of 83 %, significantly surpassing the 73 % accuracy of traditional spell-checkers, marking a substantial advancement in automated spelling correction for the Spanish language.

Conclusions: The features of the neural model facilitate spelling correction by emulating the cognitive mechanisms of the human mind. Our model detects more orthographic error types and reports less false positives. As for its limitations, this proposal requires the supervised definition of the weights assigned to the variables used for recognition.

Keywords: neocortex, deep neural model, spell-checker, pattern recognition

Article history

Received:
12th / Aug / 2023

Modified:
20th / Aug / 2023

Accepted:
7th / Oct / 2024

Ing, vol. 29, no. 3,
2024, e21135

---

* **Correspondence:** eduardpuerto@ufps.edu.co

Resumen

Contexto: La corrección de errores ortográficos en textos escritos, especialmente en textos en español, sigue siendo un desafío crucial en el procesamiento del lenguaje natural (PLN) debido a la complejidad de las estructuras de las palabras y la ineficacia de los métodos existentes cuando se aplican a grandes conjuntos de datos.

Método: Este artículo presenta un novedoso modelo neuronal inspirado en los mecanismos cognitivos del cerebro para reconocer y corregir palabras mal escritas. A través de un marco jerárquico profundo con neuronas de reconocimiento especializadas y funciones de activación avanzadas, el modelo está diseñado para mejorar la precisión y la escalabilidad de los sistemas de corrección ortográfica. Nuestro enfoque no solo mejora la detección de errores, sino que también proporciona correcciones conscientes del contexto.

Resultados: Los resultados muestran que el modelo alcanza una medida F del 83 %, superando significativamente el 73 % de precisión de los correctores ortográficos tradicionales, lo que representa un avance sustancial en la corrección automática de ortografía para el idioma español.

Conclusiones: Las funcionalidades del modelo neuronal computacional facilitan la corrección ortográfica al emular los mecanismos cognitivos de la mente humana. Nuestro modelo detecta más tipos de errores ortográficos y presenta menos falsos positivos. En cuanto a las limitaciones, la propuesta requiere una definición supervisada de los pesos asignados a las variables que se utilizan para el reconocimiento.

Palabras clave: corrector ortográfico, neocórtex, modelo neuronal profundo, reconocimiento de patrones

Table of contents

1. Introduction

Spelling correction is a fundamental task in natural language processing (NLP), with significant implications for various applications, including text composition, writing assistance, and automatic editing. In the literature, (1) suggests four classic misspelled word categories, and (2) analyze around 76K misspellings found in real-life texts produced by humans (Table I). Many errors tend to be insertions, deletions, substitutions, and transpositions of letters. (2) also found that many misspelling errors in Spanish are due to

1. Omissions, mainly of accents or of one character
2. The use of lowercase instead of uppercase at the beginning of a proper noun
3. The addition of a letter
4. The substitution of one character
5. The transposition of a letter

Table I. Common spelling errors by humans (2)

Type of error	Percentage
Insertion or addition of one character (*e.g.*, aereopuerto→aeropuerto)	4,7 %
Omission of diacritics (*e.g.*, dia→día)	51,5 %
Omission of one character (*e.g.*, mostar→mostrar)	6,8 %
Substitution of one character	4,1 %
Transposition or repetition of the same letter (*e.g.*, interpetración→interpretación, movimineto→movimiento, dirrección→dirección)	2,8 %
Cognitive errors (biene→viene)	5,9 %

Table I shows that a full 51 % of the misspellings found are omissions of a diacritic on a vowel. A notable example of this is the prevalence of word errors in millions of tweets and other massive datasets. In the context of Spanish, a language characterized by rich regional and orthographic variability, achieving accurate and efficient spelling correction poses unique challenges.

Various research efforts have focused on improving the accuracy and correctness of written content, using methods such as linguistic analysis, extraction, annotation, and correction based on dictionaries or statistical analysis. These methods have been applied to a range of tasks, including lemmatization, morphosyntactic labeling, syntactic analysis, sentiment analysis, and conceptual annotation (3–6).

On the other hand, large language models (LLMs) have revolutionized various NLP tasks, including spelling correction. Models such as GPT-4 and BERT have shown significant advances in identifying and correcting errors using deep neural networks. These models leverage large volumes of data to learn complex and contextual patterns, enhancing their ability to correct spelling errors in various languages, including Spanish. However, despite these advancements, the current approaches still face significant challenges, particularly in adapting to different contexts and reducing errors in more complex situations within Spanish texts.

Recent studies have indicated that, although modern neural models achieve competitive results, there are still limitations in adapting to regional variations and specific contexts in Spanish. Less common spelling errors and linguistic peculiarities can reduce the effectiveness of current systems. For example, research has shown that LLMs can improve about precision and coverage if trained with more diverse and specific data (7–11).

One innovative approach to addressing these challenges is to computationally simulate the brain's process for recognizing and correcting misspelled words. This paper introduces a novel neural model designed to enhance the accuracy and efficiency of spelling correction systems for Spanish texts. The proposed model employs a deep hierarchical framework with specialized recognition neurons and formal strategies to identify and correct misspelled words. This approach not only enhances the accuracy of error detection and correction but also provides a more nuanced understanding of language processing. The new neural model for detecting misspelled words simulates the process that the human brain, specifically the neocortex, follows by reusing information. This efficient approach is based on the lexical and syntactic analysis of words in Spanish.

Like the brain's neocortex, a neural network uses multiple layers, with each layer handling progressively more complex aspects, starting from character-level analysis to higher-order syntactic structures. Additionally, specialized modules, akin to cortical columns in the brain, are employed to detect and process various spelling errors, from simple typos to more contextually inaccurate words. The model also leverages contextual cues, analyzing surrounding words and the overall context to enhance the accuracy of its corrections, thereby surpassing basic pattern recognition. Moreover, it integrates a mechanism for reusing previously acquired knowledge, analogous to the brain's ability to apply past experiences to novel situations. This adaptability allows the model to accommodate different writing styles and error patterns, making it more versatile and robust.

This new deep neural model emulates certain aspects of human brain function (12–14): memory is organized as a hierarchy of patterns, and, if only part of a pattern is perceived (through sight, hearing, or smell), it can still be recognized. The model also assumes several hypotheses regarding the structure of the biological neocortex, such as the uniformity of the basic neocortical structure, known as the *cortical column*. In addition, pattern recognition neurons are constantly interconnected.

Our model improves upon the state of the art by recognizing input patterns through a process of self-association in a hierarchy of patterns. It enables the decomposition of the pattern recognition problem into simpler patterns, allowing to analyze input patterns regardless of their level of complexity or their nature (a line, a word, a sentence, a paragraph, *etc.*). In addition, the neural model is easily parallelizable, as its calculations, defined in the theorems, are simpler and distributed across a hierarchy. Moreover, computational cost can be improved with respect to other approaches, with more efficient use of memory due to a single abstract data structure that can be instanced by various text patterns. Finally, the model is adaptable since it can learn both the possible changes in pattern descriptors (such as their importance weights) and new neurons (components) if the atomic patterns are known, which is very useful in the context of a language for self-learning of words and idiomatic sentences.

In synthesis, the deep neural architecture is characterized by recognition neuron hierarchies, which increase the levels of complexity, *i.e.*, the pattern recognition neurons that constitute the lowest level levels (or X_{j-1}), will always be less complex than the neurons of the upper level (or X_j, for $j = 1, \ldots, m$). This is an innovative approach with respect to classical recognition models.

The primary contribution of this study lies in an innovative system for recognizing and correcting misspelled words in Spanish texts. This system

- demonstrates high levels of recursion and uniformity;
- operates on a self-associative principle within a hierarchical pattern framework;
- exhibits adaptability, given its ability to assimilate new patterns (words); and
- efficiently analyzes extensive Spanish texts containing words of varying structural complexity.

This method draws inspiration from cognitive neuroscience, particularly from the functioning of the neocortex, which plays a crucial role in complex language processing tasks. The pattern recognition theory of mind (PRTM) describes the basic algorithm of the neocortex, which is characterized by a hierarchy of patterns, uniformity in its basic structure, and continuous connectivity between its pattern recognition modules (14).

This work is organized as follows. Section 2 presents the research trends and related work, providing a comprehensive overview of the existing approaches to spelling correction systems for Spanish texts. Section 3 details the methodology employed, including the formal definition of a neuron within the neuron module and a description of the activation functions used within the neural network model. This section outlines the architecture of the neural model and its optimization, explaining how the model has been tailored for efficient performance in spelling correction. Section 4 presents the experiments conducted, describing the experimental setup, datasets, and performance evaluations for the proposed model in comparison with other existing methods. Finally, Section 5 states the conclusions and proposes directions for future work, highlighting the contributions of this study and discussing potential improvements and extensions of the model.

2. Research trends and related work

The field of NLP has witnessed remarkable advancements in recent years, particularly in the domains of spell-checking, grammatical error correction (GEC), and overall text improvement. These developments have been largely driven by the advent of sophisticated neural network architectures and the increasing availability of large-scale datasets. Transformer-based models have emerged as the dominant paradigm, demonstrating unprecedented performance across various NLP tasks. (15)

introduced GECToR, a transformer-based approach for GEC that achieves state-of-the-art results in several benchmarks. Building upon this work, in (16), the GECToR architecture was adapted for the Russian language (RuGECToR). Furthermore, (17) proposed a unified pre-training approach for monolingual and multilingual GEC. Their method leverages massive amounts of synthetic data and multi-task learning, achieving new state-of-the-art results in standard GEC benchmarks in English and extending well to other languages. (18) expanded the evaluation of GEC systems beyond essays from non-native learners by introducing CWEB, a new benchmark for GEC that comprises website texts written by English speakers of varying proficiency levels. This work highlights how the lower error density in these domains poses significant challenges for current GEC systems, demonstrating the need for models that better generalize across different topics and genres.

The field of spell-checking and GEC has therefore seen substantial advancements in recent years. (19) provided an extensive overview of the field of GEC, which addresses the automatic detection and correction of various errors in texts, including grammatical, orthographic, and semantic discrepancies. Over the past decade, significant advancements have been driven by five major shared tasks, catalyzing the evolution from rule-based methods and statistical classifiers to advanced neural machine translation systems. The integration of deep learning techniques, particularly transformer-based models, has led to significant improvements regarding accuracy and capability. Furthermore, the focus has expanded beyond simple error correction to include context-aware corrections, fluency enhancement, and multilingual support. The emphasis on efficiency and real-time performance demonstrates the field's maturation and its readiness for widespread practical application. As these technologies continue to evolve, we can expect to see more sophisticated, efficient, and widely applicable text improvement systems that not only correct errors but also enhance the overall quality and fluency of written communication across multiple languages and domains.

Some particularly interesting works related to the proposed model include STILUS (20), which distinguishes four types of errors: grammatical, orthographic, semantic, and style. In the case of orthographic revision, STILUS corrects words in three stages: the generation of alternatives to the incorrect word, the weighting of alternatives, and the arrangement of alternatives. Another system is ArText, a prototype automatic help system for writing texts in Spanish in specialized domains (21). The system has three modules: the first module handles aspects of structure, content, and phraseology; the second focuses on format and linguistic revision; and the last allows users to linguistically revise their texts. XUXEN (22) is a spell checker/corrector defined based on two morphological formalisms. It uses a highly inflected standardized language with a broad relationship between nouns and verbs as well as a lexicon that contains approximately 50 000 items across different grammatical categories.

On the other hand, (23) proposed a spelling and grammar checker algorithm for texts where mistakes are not detected through tagging and parsing, but rather through statistical analysis, comparing combinations of two words used in the text against a corpus of one hundred million words. In (24), the JHU FLuency-Extended GUG corpus (JFLEG) aimed at developing and evaluating GEC was presented. It represents a broad range of language proficiency levels and uses holistic fluency edits to not only correct grammatical errors but also to make the original text sound more natural.

Additionally, (3) presented a general approach to various NLP applications, such as translation and recognition, using modern techniques like deep learning. Finally, to date, there are no works based on a hierarchical approach to pattern recognition (in our case, words) as a fundamental mechanism for reusing text patterns, which is an efficient way to recognize many words, some of which may be complex. The next sections detail our proposal.

3. Methodology

This section presents the mathematical formalization of the neural model, including the neuron or recognition module, its activation functions, and its recursive architecture, as well as the computational algorithm that integrates the entire model.

3.1. Formal definition of a neuron within the neuron module

A pattern recognition module (or neuron) is formally defined as a 3-tuple. The $\Gamma\rho$ notation is used to represent the module that recognizes the ρ pattern (ρ: shapes, letters, words, *etc.*). $\Gamma\rho =< E, U, S_o >$, where E is an array composed of the 2-tuple E =<S, C> (Table I), S =<Signal, State>is an array that represents the set of signals that make up the pattern recognized by Γ and their corresponding states, and C is an array that encodes information about the pattern, as defined by the 3-tuple C =<D, V, W>, where D represents the descriptors of Γ, V is the domain vector for each D (*i.e.*, the possible values of each descriptor), and W is the importance weight of the descriptor for the ρ pattern. Additionally, U denotes the thresholds vector used by the module (Γ) to recognize its respective pattern.

Table II shows one artificial neuron, *i.e.*, a neocortical pattern recognition module according to the PRTM theory.

Table II. Neuron: matrix E = <S, C>

E				
S		**C**		
Signal	**State**	**Descriptor (D)**	**Domain (V)**	**Weight (W)**
1	False	Descriptor1	<possible values of the descriptor >	[0,1]
2	False	Descriptor2	<possible values of the descriptor >	[0,1]
3	False	Descriptor3	<possible values of the descriptor >	[0,1]
…	…	…	…	…
n	False	Descriptor	<possible values of the descriptor >	[0,1]
U: <ΔU_1, ΔU_2>				

In the neural model, each neuron/module or pattern recognition module can recognize and observe every aspect of the input pattern $s()$, as well as the way in which the different parts of the data in the input pattern may or may not relate to each other.

There are two types of thresholds: ΔU_1 is the threshold for recognition by key signals, and ΔU_2 is the threshold for recognition by partial or total mapping. ΔU_1 should be stricter than ΔU_2, given that the process of recognition by key signals utilizes only a few signals. Finally, each module produces a recognition or petition signal (S_o) towards lower levels. As petition, S_o becomes the input signal $s()$ for the pattern-matching neurons of the lower levels. When there is a recognition signal, it is diffused to its higher attainable levels, in order to modify the state of the signal to "trueïn the patterns of said levels.

Thus, a pattern is represented as a set of lower-level sub-patterns that conform to it (n descriptors), and it also serves as the sub-pattern of a higher-level pattern. The value of n depends on the pattern to be recognized (the descriptors of the pattern). The values of W are normalized [0,1], and δU_1 or ΔU_2 are thresholds that must be overcome to recognize the pattern. These values are defined in a supervised manner, according to the domain of application. In the context of text analysis, the main patterns to be recognized (ρ) are letters, words, special signs, and numbers.

3.2. Activation functions within the neural network model

Our neural network model uses two strategies for the checking/correction/recognition process, one based on key signals and the other based on partial signals. Both use a threshold of satisfaction and the importance of the signal weights. Thus, the recursive model allows decomposing the pattern recognition problem into simpler patterns, which makes it possible to analyze very complex words.

Particularly, the first strategy defined to recognize and correct text patterns using the aforementioned structures is called *Activation function 1 by key signals*, and the other is the *Activation function 2 by partial pattern matching* (25). The first uses the importance weights of the input signals identified as key, and the second uses the partial or total presence of the signals. A signal is key when it represents information that allows quickly recognizing a pattern. For example, the final letter rïn infinitive verbs could be taken as a key.

Key signal. A s_i signal in the Γ module is key if its importance weight has a value greater than or equal to the average weight of all the signals in Γ.

$$\forall s_i \in S(\Gamma), \text{ if } [w(s_i) \geq w_{average} S(\Gamma)] \rightarrow Key_\Gamma \tag{1}$$

Activation function by key signals. A ρ pattern is recognized by key signals if the average of the weights of the key signals recognized exceeds the ΔU_1 threshold. This type of recognition uses the descriptors (signals or sub-patterns) with greater weight of importance.

$$\frac{\sum_{i=1 \,\cap\, \text{state}(s_i=\text{true}) \,\cap\, s_i \in Key_\Gamma}^{n} w(s_i)}{|Key_\Gamma|} \geq \Delta U1 \rightarrow S_0 \tag{2}$$

Activation function by partial mapping. This strategy consists of validating whether a signal minimum's number in Γ exceeds the δU_2 threshold.

$$\frac{\sum_{i=1 \,\cap\, \text{state}(s_i=\text{true})}^{n} w(s_i)}{n} \geq \Delta U2 \rightarrow S_0 \tag{3}$$

This process of calculation is carried out for each module and each level of recognition X_i (from X_1 until X_m).

3.3. Architecture of the neural model

This section describes the neural network model instanced for the specific case of text analysis. Particularly, the hierarchical system in Fig. 1 represents the recursive and iterative process for the recognition and correction of words. Each layer in the hierarchy is an interpretation space X_i from $i = 1$ to m. X_1 is the level of recognition for atomic patterns (*e.g.*, letters or letterforms), and X_m is the level of recognition for complex patterns (*e.g.*, words and compound words). Each level is composed of γ_{ji} recognition modules (for $j = 1, 2, 3 \ldots$ neurons at level i). X_{ij} is the pattern recognized by module j at level i. The function of each recognition module is to recognize its corresponding pattern.

Fig. 1 shows the architecture of the neural network (*i.e.*, the hierarchical pattern recognition system). The multiple hidden layers are the recognition spaces of level i or the levels of complex pattern recognition (X_i). This is how the neural model can find extremely complex patterns via bottom-up or top-down approaches.

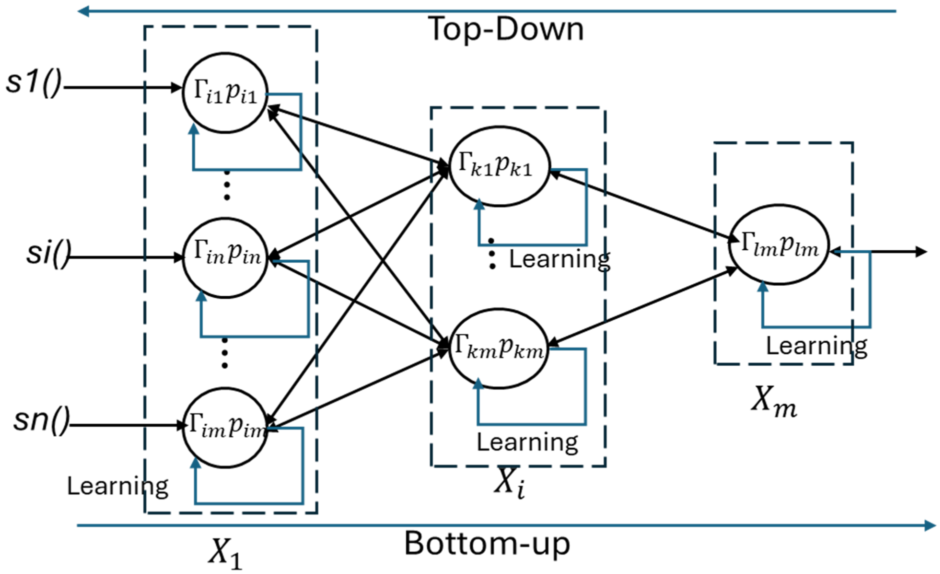

Figure 1. Recursive architecture of the neural model

Here, X_i is the recognition space of the 1-level, Γ_{i1}: is the j-neuron of the 1-level, which recognizes p_{i1}, *i.e.*, the pattern recognized by the neuron j at level 1.

This architecture is marked by hierarchies of recognition neurons that increase in complexity. Lower-level neurons are less complex than those at higher levels, which makes this approach innovative compared to traditional recognition models (26,27).

Two analytical processes characterize the algorithm. The first process, called *top-down*, recognizes the input pattern through decomposition (Fig. 1). The top-level module invokes the recognition neurons of lower-level constituents, and these recursively perform the same function. The second process, called *bottom-up*, is used for recognizing atomic patterns. Here, the output signal of the recognized pattern is sent to the neurons that make up the top-level representation. These top-level neurons will be activated (or not) depending on whether they exceed a recognition threshold.

3.4. Optimized computational neural model

The algorithm works as follows. It receives the input text (y = s(): sentences, words (s)) (line 2). Then, it decomposes this input into its sub-patterns, which are stored in L (lines 4-5). On line 7, it determines the level of the hierarchy where the recognition of the input pattern (y) should start and end. Afterwards, L recognition requests for (y) are created (line 12). The algorithm enters a loop that iterates over each pattern in L (line 13). If the recognition is successful at the current level (line 14), the information is updated using the *updateSubpatterns* function (line 18). If the input pattern is composed of lower-level signals or has recognized atomic signals, a bottom-up process is conducted; otherwise, a top-down procedure is followed (line 16). If the recognition fails at the lowest level (level == 1) and no pattern has been recognized, the algorithm ends (lines 22-24). This process continues until all patterns in L have been processed or their recognition has failed at the lowest level. Finally, the function returns the result of the hierarchical recognition process (line 28).

```
      Algorithm for the implementation of the recursive neural recognition model
1   function hierarchicalRecognition(y)
2       // y is the input pattern
3
4       // Step 1: Decompose y into hierarchical patterns
5       subPatterns = decomposePattern(y)
6
7       // Step 2: Determine the highest-level N of the hierarchy to start recognition
8
9       N = determineInitialLevel(subPatterns)
10      // Steps 3-5: Hierarchical recognition process
11      for level from N to 1 do
12          L = createPatternList(subPatterns, level)
13          for each pattern in L do
14              if recognizePattern(pattern) then
15                  if level == 1 then
16                      return success(pattern)
17                  else
18                      updateSubPatterns(subPatterns, pattern, level)
19                      break // Move to the next lower level
20                  end if
21              end if
22          end for
23
24          if level == 1 and no pattern was recognized then
25              return failure()
26          end if
27      end for
28  end function
```

Figure 2. Algorithm for the implementation of the recursive neural recognition model

4. Experiments

This section presents the results and an evaluation of the neural model in comparison with other works, for which three additional systems were selected: STILUS, SpanishChecker, and Microsoft word. These three systems were chosen because they are tools designed to analyze spelling and find basic grammar and style mistakes in Spanish texts. All of them show errors automatically. For these test scenarios, several paragraphs were artificially made, with misspelled words in Spanish. In these tests, the inputs, *i.e.*, the paragraphs, were introduced into the neural model as an array of words, while, in the other systems, they were entered as a plain text file. The standard precision (P) and coverage (C) metrics, as well as the F-measure (F) (28), were used during these experiments to compare the performance of the evaluated systems.

Table III. Results of applying different systems to various types of spelling errors

	Methods	**Detected errors**	**False negatives**	**False positives**	**P**	**C**	**F**
Added Letters	Neural Model	12	0	0	100 %	100 %	100 %
	SpanishChecker	15	0	3	83 %	100 %	90 %
	STILUS	14	0	2	88 %	100 %	93 %
	Microsoft Word	13	0	2	92 %	100 %	95 %
Omitted letters	Neural Model	10	0	0	100 %	100 %	100 %
	SpanishChecker	14	0	4	77 %	100 %	87 %
	STILUS	10	0	0	100 %	100 %	100 %
	Microsoft Word	10	0	0	100 %	100 %	100 %
Cognitive errors	Neural Model	14	0	0	100 %	100 %	100 %
	SpanishChecker	16	2	5	76 %	88 %	81 %
	STILUS	15	0	2	88 %	100 %	93 %
	Microsoft Word	14	1	0	100 %	92 %	95 %
Exchange of two letters	Neural Model	8	0	3	72 %	100 %	83 %
	SpanishChecker	11	0	6	64 %	100 %	78 %
	STILUS	13	0	8	61 %	100 %	75 %
	Microsoft Word	14	0	9	60 %	100 %	75 %
Digits or special characters	Neural Model	5	0	0	100 %	100 %	100 %
	SpanishChecker	1	4	0	100 %	20 %	33 %
	STILUS	1	3	1	50 %	25 %	33 %
	Microsoft Word	2	3	0	100 %	40 %	57 %
Full text in digital versions	Neural Model	23	0	9	71,5 %	100 %	83 %
	SpanishChecker	56	3	45	57,9 %	95 %	72 %
	STILUS	54	1	41	58,1 %	98 %	73 %
	Microsoft Word	51	2	39	58,6 %	96 %	73 %

The first row of Table III presents the results of applying the neural model to a paragraph containing 205 words, out of which more than 5 % contained errors due to added letters. The neural model effectively detects all real errors caused by the addition of letters, as in ’entrdada’, ’tellevisión’, and ’teléfonoo’. In contrast, SpanishChecker generates three false positives corresponding to the names ’Pantoja’, ’Goya’, and ’Chabelita’. STILUS produces similar results, with two false positives (’Pantoja’ and ’Goya’), while Microsoft Word also flags ’Chabelita’ and ’Goya’ as errors. The neural model recognizes ’Chabelita’, ’Goya’, and ’Pantoja’ as well-written words.

The second row corresponds to a paragraph containing 203 words, with 5 % of the words exhibiting omitted letters. According to these results, the neural model effectively detects all errors related to omitted letters, just like Microsoft Word and STILUS. In contrast, SpanishChecker generates four false positives corresponding to the words ’expresidente’, ’Aznar’, ’populismo’, and ’patrióticamente’ (with the latter being two false positives) while omitting ’Congres’ (resulting in one false negative).

The third row uses a paragraph that contains 203 words, with 20 % of the words exhibiting cognitive errors. The neural model detects 14 errors, and Microsoft Word identifies a false negative: ’Confexionar’. Although SpanishChecker identifies the errors, many of its correction recommendations are syntactically and semantically far from the correct word. For example, for the word ’Confexionar’, SpanishChecker suggests: {conexionar, confinar, confinara, confinare, confinará, confinaré, confinaría, confina}; for ’vioseguridad’, it suggests: {vio seguridad, vio-seguridad, seguridad, esguardad, resguardad, seguridades, *etc.*}; and, for ’varato’, it suggests: {va rato, va-rato, verato, grato, arto, parto, urato, verte, varío, barato, *etc.*}. Among its false positives are ’Cofeccionistas’ {confusionistas, confesionistas, confusionista, cancionista, *etc.*} and ’Cucuteños’ {cicutinas, cacereños, cicateros, etc.}. The two false negatives are ’Crusada’ and ’Biernes’. Finally, STILUS generates the false positives ’Oquendo’ and ’Cucuteña’.

The fourth row corresponds a paragraph that contains 5 % of words with two exchanged letters. In this case, all systems incorrectly detect more errors. The neural model incorrectly detects only three errors, while the other systems detect significantly more.

In the fifth row, the results obtained by the different systems are shown for a paragraph with 5 % of words containing errors related to digits or special characters. In this case, only the neural model correctly detects the errors. The other systems either fail to detect the errors or incorrectly identify more (as is the case with STILUS).

Finally, the last row of the dataset used in the experiment consists of 32 texts from the digital version of El País, dated May 17^{th}, 2001, which were copied into a Word document. Approximately 9000 words were analyzed, with 14 spelling errors. SpanishChecker identifies the fewest errors (11), while Microsoft Word and STILUS are more effective, detecting 13 and 12 errors, respectively. Our approach detects all errors but incorrectly identifies nine additional ones. The other approaches incorrectly detect many more. The main issue with these systems is that they flag errors arising from the inclusion of digits or special characters, which is not applicable in this case, resulting in many false positives. Overall, their results are significantly lower than those achieved by our system.

4.1. Comparison with an n-gram language model

As a point of reference, we considered the standard n-gram language model algorithm. This spell-checking and auto-correction system uses the Web to infer misspellings, incorporating a term list, an error model, a language model (LM), and a confidence classifier algorithm. For each token in the input text, candidate suggestions are drawn from the term list and scored using the error model. These candidates are evaluated in context using the LM and then re-ranked. A classifier is used for each token to determine the confidence level regarding whether a word has been misspelled, and, if so, whether it should be autocorrected to the best-scoring suggestion available.

The main contribution of this work is that it does not require any manually annotated resources, inferring its linguistic knowledge entirely from the Web. In this sense, we propose a deep neural architecture based on both supervised and unsupervised mechanisms for the discovery and selection of features in classification problems.

Our approach consists of three phases. The first phase, called *feature analysis*, is supported by two feature-engineering approaches to discover or select atomic features/descriptors. This phase should include many well-spelled words as well as a substantial number of non- words or misspellings, which is equivalent to the term list. The second phase, called *aggregation*, creates a feature hierarchy by merging descriptors from the atomic features. Then, the last phase classifies the inputs. This phase employs a supervised learning approach, while the earlier phases combine both supervised and unsupervised learning methods (29). If a word is misspelled, the system utilizes clusters of well-written words for recommendations; if no suitable suggestion exists, it searches the Web (for example, in repositories such as WordReference) and recommends a suitable alternative, including it in the group of well-written words. Future work may involve a quantitative evaluation of the performance of these approaches.

4.2. A final discussion about the characteristics of the neural network model

Our neural network model is highly recursive and uniform. It recognizes input patterns through a process of self-association within a hierarchy of patterns, and it allows decomposing the pattern recognition problem into simpler components, enabling the analysis of input patterns regardless of their complexity or nature (*e.g.*, a line, a word, a sentence, a paragraph, *etc.*).

Moreover, our recognition model is adaptable; it can learn both the potential changes in the pattern descriptors (including their importance weights) and new neurons (patterns) if the atomic patterns are known. This adaptability is particularly useful for the self-learning of words and idiomatic expressions in a language context. Unlike other approaches, the neural model can recognize words with special characters in a manner similar to how the brain does (*e.g.*, = a, E = 3, S = 5, 9 = q), allowing for interpretations like m@ma, p3ra, *etc*.

Additionally, its novelty lies in the way it addresses this problem. While several NLP models have achieved unprecedented performance levels, they often come at high computational costs.

5. Conclusions and future works

The proposed model aims to advance the state of the art in spelling correction for Spanish – and potentially other languages – by offering a solution informed by biological processes and optimized for practical application. This innovative approach could lead to significant improvements in automated text correction systems, benefiting users across various linguistic contexts. The neural model detects a wider range of orthographic errors and generates fewer false positives, although it requires a supervised definition of the weights assigned to the variables used for recognition.

This work presents a new neural model for detecting misspelled words, closely mirroring how the human brain (specifically the neocortex) addresses this problem. The model reuses information to propose an efficient approach based on the lexical analysis of word syntax in Spanish.

This system demonstrates high levels of recursion and uniformity, operating on a self- associative principle within a hierarchical pattern framework. It showcases adaptability by assimilating new patterns (words) and efficiently analyzes extensive Spanish texts containing words of varying structural complexity.

A comparative evaluation indicated that the precision and coverage of the neural model are competitive with those of other spell-checkers. In the experiments, the system outperformed three other tools; it achieved an F-measure of 83 %, surpassing the other spell-checkers' 73 %. Our neural model can detect a broader variety of orthographic errors while producing fewer false positives. As future work, the architecture of the neural model should be extended to incorporate unsupervised learning mechanisms, allowing it to improve its performance by learning new words. Additionally, it must be adapted to handle other languages. The model could also be developed to simultaneously correct texts written in both English and Spanish, which would be valuable in translation tasks. To this effect, the model needs to be expanded with more recognition neurons in different languages, enhancing its lexical basis.

Finally, a comparison with other approaches in the domain of NLP is not presented herein, as our primary focus is on the spell-checking (auto-correction) problem. While there are several NLP approaches for machine translation, cognitive dialogue systems, sentiment analysis, text classification, and text summarization – utilizing techniques from natural language understanding and generation present in state-of-the-art NLP – a future research direction could involve analyzing the application of our approach in these contexts for comparison with existing techniques. By leveraging the capabilities of LLMs like GPT-3.5, researchers can further refine and extend these systems, leading to more accurate, efficient, and sophisticated solutions for spelling correction in Spanish and beyond.

6. CRediT author statement

Puerto Cuadros, E.G: contributed to conceptualization, data collection, formal analysis, and writing – original draft preparation and editing.

References

[1] S. Almurashi, “Analysis of the most common spelling errors in English for Saudi students: A case study of foundation year students,” *Getsempena English Edu. J.*, vol. 10, no. 1, pp. 73-89, 2023. https://doi.org/10.46244/geej.v10i1.2081 ↑3

[2] F. Bustamante and E. Díaz, “Spelling error pattern in Spanish for word processing applications,” in *Proc. 5th Int. Conf. Lang. Res. Eval.*, 2006, pp. 93-98. http://www.lrec-conf.org/proceedings/lrec2006/pdf/119_pdf.pdf ↑3

[3] S. Singh and A. Mahmood, “The NLP cookbook: Modern recipes for transformer based deep learning architectures,” *IEEE Access*, vol. 9, pp. 68675-68702, 2021. https://doi.org/10.1109/ACCESS.2021.3077350 ↑3, 7

[4] A. Ferreira and S. Hernández. “Diseño e implementación de un corrector ortográfico dinámico para el sistema tutorial inteligente”, *Rev. Signos*, vol. 50, no. 95, pp. 385-407, 2017. http://dx.doi.org/10.4067/S0718-09342017000300385 ↑3

[5] A. San Mateo, “Un corpus de bigramas utilizado como corrector ortográfico y gramatical destinado a hablantes nativos de español,” *Rev. Signos*, vol. 49, no. 90, pp. 94-118, 2016. http://dx.doi.org/10.4067/S0718-09342016000100005 ↑3

[6] P. Gamallo and M. Garcia, “LinguaKit: A multilingual tool for linguistic analysis and information extraction,” *Linguamatica*, vol. 9, no. 1, pp.19-28, 2017. ↑3

[7] G. Zomer and A. Frankenberg-Garcia, “Beyond grammatical error correction: Improving L1-influenced research writing in English using pre-trained encoder-decoder models,” in *Find. Assoc. Comp. Ling. EMNLP 2021* , 2021, pp. 2534-2540. https://doi.org/10.18653/v1/2021.findings-emnlp.216 ↑4

[8] B. Ünlütabak and O. Bal, “Theory of mind performance of large language models: A comparative analysis of Turkish and English,” *Comp. Speech Lang.*, vol. 89, art. 101698, 2025. https://doi.org/10.1016/j.csl.2024.101698 ↑4

[9] M. Bijoy *et al.* “A transformer-based spelling error correction framework for Bangla and resource scarce Indic languages,” Comp. Speech https://doi.org/10.1016/j.csl.2024.101703 ↑4

[10] E. Puerto, J. Aguilar, R. Vargas, and J. Reyes, “An Ar2p deep learning architecture for the discovery and the selection of features,” *Neural Process. Letters*, vol. 50, no. 1, pp. 623-643, 2019. https://doi.org/10.1007/s11063-019-10062-4 ↑4

[11] E. Puerto, and J. Aguilar and A. Pinto, “Automatic spell-checking system for Spanish based on the Ar2p neural network model,” *Computers*, vol. 13, no. 13, art. 76, 2024. https://doi.org/10.3390/computers13030076 ↑4, 12

[12] E. Puerto and B. R. Pérez, “Análisis de la teoría de la mente humana basada en el reconocimiento de patrones,” 2014. [Online]. Available: http://hdl.handle.net/20.500.12749/12358 ↑4

[13] E. Puerto Cuadros, “Avances en el conocimiento y modelado computacional del cerebro autista: Una revisión de literatura,” *Cuad. Activa*, vol. 9, no. 2017, pp. 109-125, 2017. https://doi.org/10.53995/20278101.425 ↑4

[14] R. Kurzweil, “How to make mind,” *Futurist*, vol. 47, no. 2, pp. 14-17, 2013. ↑4, 5

[15] K. Omelianchuk, V. Atrasevych, A. Chernodub, and O. Skurzhanskyi, “GECToR – Grammatical error correction: Tag, not rewrite,” in *15th Work. Innov. Use NLP Build. Edu. App.*, 2020, pp. 163- 170. `https://doi.org/10.48550/arXiv.2005.12592` ↑5

[16] I. A. Khabutdinov, A. V. Chashchin, A. V. Grabovoy, A. S. Kildyakov, and U. V. Chekhovich, “RuGECToR: Rule-based neural network model for Russian language grammatical error correction,” *Programm. Comp. Software*, vol. 50, no. 4, pp. 315-321, 2024. `https://doi.org/10.1134/S0361768824700129` ↑6

[17] S. Rothe, J. Mallinson, E. Malmi, S. Krause, and A. Severyn, “A simple recipe for multilingual grammatical error correction,” in *ACL-IJCNLP 2021*, 2021, pp. 702-707. `https://doi.org/10.18653/v1/2021.acl-short.89` ↑6

[18] S. Flachs, O. Lacroix, H. Yannakoudakis, M. Rei, and A. Søgaard, “Grammatical error correction in low error density domains: A new benchmark and analyses,” in *2020 Conf. Empirical Methods Natural Lang. Process.*, 2020, pp. 8467-8478. `https://doi.org/10.48550/arXiv.2010.07574` ↑6

[19] C. Bryant, Z. Yuan, M. R. Qorib, H. Cao, H. T. Ng, and T. Briscoe, “Grammatical error correction: A survey of the state of the art,” *Comp. Ling.*, vol. 49, no. 3, pp. 643-701. `https://doi.org/10.1162/coli_a_00478` ↑6

[20] V. González, B. González, and M. Muriel, “STILUS: sistema de revisión lingüística de textos en castellano,” *Proc. Leng. Nat.*, vol. 29, pp. 305-306, 2002. ↑6

[21] I. da Cunha, M. Montané, and L. Hysa, “The arText prototype: An automatic system for writing specialized texts,” in *Proc. Euro. Chapter Assoc. Comp. Ling.*, 2017, pp. 57-60. `https://aclanthology.org/E17-3015` ↑6

[22] E. Agirre et al., “XUXEN: A spelling checker/corrector for Basque based on two-level morphology,” in *3rd Conf. Applied Natural lang. Process.*, 1992, pp. 119-125. ↑6

[23] A. Valdehíta, “Un corpus de bigramas utilizado como corrector ortográfico y gramatical destinado a hablantes nativos de español,” *Rev. Signos*, vol. 49, pp. 94-118, 2016. ↑6

[24] C. Napoles, K. Sakaguchi, and J. Tetreault, “A fluency corpus and benchmark for grammatical error correction”, in *Proc. Euro. Chapter Assoc. Comp. Ling.*, 2017, pp. 229-234. `https://doi.org/10.48550/arXiv.1702.04066` ↑6

[25] E. Puerto and J. Aguilar, “Formal description of a pattern for a recursive process of recognition,” in *Proc. IEEE Latin American Conf. Comp. Intell.*, 2016, pp. 1-2. `https://doi.org/10.1109/LA-CCI.2016.7885746` ↑8

[26] E. Puerto, J. Aguilar, and D. Chávez, “A new recursive patterns matching model inspired in systematic theory of human mind,” *Int. J. Advance. Comp. Tech. (IJACT)*, vol. 28, no. 9, 2017. ↑9

[27] E. Puerto, J. Aguilar, R. Vargas, and J. Reyes, “An Ar2p deep learning architecture for the discovery and the selection of features,” *Neural Process. Letters*, vol. 50, no. 1, pp. 623-643, 2019. `https://doi.org/10.1007/s11063-019-10062-4` ↑9

[28] D. Powers, “Evaluation: From precision, recall and f-measure to ROC, informedness, markedness & correlation,” *J. Machine Learn. Tech.*, vol. 2, pp. 37-63, 2011. ↑11

[29] E. Puerto and J. Aguilar. "Learning algorithm for the recursive pattern recognition model," *App. Artif. Intell.*, vol. 30, no. 7, pp. 662-678, 2016. `https://doi.org/10.1080/08839514.2016.1213584` ↑13

Eduard Gilberto Puerto Cuadros

Systems engineer, MSc in Computer Science, and PhD in Applied Science and Engineering. Junior Researcher at MinCiencias, with experience as Director of the Artificial Intelligence Research Group (GIA), recognized by MinCiencias (`https://gia.ufps.edu.co/index/`), at Universidad Francisco de Paula Santander (UFPS); and as Director of the Eduardo Cote Lamus Library Division. Full professor at the Department of Systems and Informatics of UFPS, and professor of the Master's program in ICTs Applied to Education. He has supervised multiple Undergraduate and Master's projects and has served as co-researcher in various research groups, *i.e.*, the International Internship of the Department of Computer Science at the University of Miami, the Institute for Research in Applied Mathematics and Systems (IIMAS) in Mexico DF, the Center for Microcomputing and Distributed Systems (CEMISID) at Universidad de los Andes (Mérida, Venezuela), the Robotics and Intelligent Systems Laboratory of Escuela Politécnica Nacional in Quito (Ecuador), and the Computational Sciences Research Group (CICOM) of Universidad de Pamplona (Colombia). He has actively participated in several scientific events and authored numerous articles and book chapters on his areas of interest, which include artificial intelligence, machine learning, deep learning, logic programming, theory of computation, and complex systems.

Email: eduardpuerto@ufps.edu.co

UNIVERSIDAD DISTRITAL
FRANCISCO JOSÉ DE CALDAS

Ingeniería
https://revistas.udistrital.edu.co/index.php/reving/issue/view/1241
DOI: https://doi.org/10.14483/23448393.21059

Research

Development of an Alcoholic Beverage from *Cubio* (*Tropaeolum tuberosum* Ruiz & Pav.) Using *Saccharomyces bayanus* Yeast

Desarrollo de una bebida alcohólica a partir de cubio (*Tropaeolum tuberosum* Ruiz & Pav.) empleando levadura de *Saccharomyces bayanus*

Martha Morantes Triana[1], Alfredo López-Molinello[1]*, Lena Prieto[1], Ismael Povea[1], and Santiago Sáenz[2]

[1]Food Engineering, Faculty of Engineering, Universidad de La Salle, Bogotá, Colombia.
[2]Agronomic Engineering, Faculty of Agribusiness Science, Universidad de La Salle, Yopal campus, Colombia

Abstract

Context: *Cubio (Tropaeolum tuberosum)*, an ancestral tuber cultivated in select regions of Colombia, possesses significant nutritional value but remains a marginalized crop. This study aims to enhance the recognition of *cubio* by diversifying its applications through the production of a fermented alcoholic beverage.
Method: Initially, the *cubio* tuber was characterized. A concentrated and enzymatic pretreatment utilizing alpha-amylase and glucoamylase was employed to release sugars. Afterwards, fermentation was carried out, using *Saccharomyces bayanus* in a carefully controlled bioreactor setting. The fermentation medium was composed of 0.1 % (NH_4) H_2PO_4, 0.3 % $MgSO_4$, 0.5 % peptone, and 0.3 % yeast extract, with the aim of reaching an alcohol content of 15 °GL. The bioreactor was inoculated with *Saccharomyces bayanus* at 25 °C, maintaining a pH of 5.2 and an agitation speed of 100 rpm. Daily monitoring of pH levels, sugar concentrations, and biomass was conducted over a 15-day period. Finally, the physicochemical properties, physical attributes, and sensory qualities of the resulting product were assessed.
Results: The analysis of the *cubio* tuber revealed the presence of 2.18 ± 0.002 % reducing sugars, 4.48 ± 0.064 % proteins, and 1.66 ± 0.015 % starch. Throughout the fermentation process, the yeast exhibited a growth rate of 2.3786 mg.L^{-1}.day^{-1}. As a result, the concentration of reducing sugars decreased to 15.45 mg.L^{-1}.day^{-1}, and an alcohol production of 1.1786 °GL.day^{-1} was observed. The final alcoholic beverage contained 15.24 °GL, with a pH of 4.5 and a total acidity of 7.21 ± 0.029 g. L^{-1}. Additionally, an expert panel positively rated the flavor and aroma of the beverage.
Conclusions: It is technologically possible to produce a fermented alcoholic beverage of adequate quality from the *cubio* tuber, implying an alternative use for this ancestral crop.
Keywords: alcoholic beverage, yeast, fermentation, ancestral tuber

Article history

Received:
24th/Jul/2023
Modified:
25th/Jun/2024
Accepted:
20th/Aug/2024

Ing, vol. 29, no. 3, 2024, e21059

---

* **Correspondence:** alopez@unisalle.edu.co

Resumen

Contexto: Cubio (*Tropaeolum tuberosum*), un tubérculo ancestral cultivado en regiones selectas de Colombia, posee valor nutricional significante pero continúa siendo marginalizado. Este estudio busca expandir el reconocimiento del cubio al diversificar sus aplicaciones mediante la producción de una bebida alcohólica fermentada.

Método: Inicialmente, el tubérculo de cubio fue caracterizado. Se empleó un pretratamiento concentrado y enzimático para liberar azúcares. Después se llevó a cabo el proceso de fermentación, utilizando *Saccharomyces bayanus* en un biorreactor cuidadosamente configurado y controlado. El medio de la fermentación estaba compuesto de 0.1 % de (NH_4) H_2PO_4, 0.3 % de $MgSO_4$, 0.5 % de peptona y 0.3 % de extracto de levadura, a fin de alcanzar un contenido de alcohol de 15 °GL. El biorreactor fue inoculado con *Saccharomyces bayanus* a 25 °C, manteniendo un pH de 5.2 y una velocidad de agitación de 100 rpm. Se monitorearon diariamente los niveles de pH, la concentración de azúcar y la biomasa a lo largo de un periodo de 15 días. Finalmente, se evaluaron las propiedades fisicoquímicas, los atributos físicos y las cualidades sensoriales del producto resultante.

Resultados: El análisis del tubérculo de cubio evidenció la presencia de 2.18 ± 0.002 % de azúcares reductores, 4.48 ± 0.064 % de proteína y 1.66 ± 0.015 % de almidón. A lo largo del proceso de fermentación, la levadura mostró una tasa de crecimiento de 2.3786 $mg.L^{-1}.día^{-1}$. Como resultado, la concentración de azúcares reductores se redujo a 15.45 $mg.L^{-1}.día^{-1}$, y se observó una producción de alcohol de 1.1786 $°GL.día^{-1}$. La bebida alcohólica final contenía 15.24 °GL, con un pH de 4.5 y una acidez total de 7.21 ± 0.029 $g.\ L^{-1}$. Adicionalmente, un panel de expertos calificó positivamente el sabor y el aroma de la bebida.

Conclusiones: Es tecnológicamente posible producir una bebida fermentada alcohólica de calidad adecuada a partir de tubérculo de cubio, lo que implica un uso alternativo para este cultivo ancestral.

Palabras clave: bebida alcohólica, levadura, fermentación, tubérculo ancestral

Table of contents

1. Introduction

In recent years, there has been growing interest in reevaluating and rediscovering ancient foods for their nutritional value, flavors, unique characteristics, and textures. The Food and Agriculture Organization of the United Nations (FAO) has been urging its member countries to explore the technological potential of alternatives categorized as *underutilized and neglected crops, secondary crops, or promising crops*. Colombia has been proactive in this commitment, leading to the enactment of Law 2046 of 2020 by Congress, which promotes the cultivation, consumption, and technological use of ancestral crops. Among these crops, certain tubers have been preserved with the help of indigenous communities and farmers, one of them being the tuber known as *cubio (Tropaeolum tuberosum* Ruiz & Pav. 1802, Brassicales: Tropaeolaceae), which is native to the South American Andes. However, as emphasized by the FAO (1), the limited allocation of resources by governments for the promotion and development of these species has led to missed opportunities. Highlighting the need for political will, this research underscores the potential to promote the consumption and processing of *cubio* through the production of a distilled beverage as a technological alternative that meets the established parameters for such products (2).

Cubio is known by various names, such as *añu, apiñu, cubio, isañu, isaña, isaño, pañí, puel, majua, mauja, mashwa,* or *mashua*, depending on the Andean region where it is cultivated. It has lower commercialization compared to other Andean crops such as potato (*Solanum tuberosum* L.), *oca (Oxalis tuberosa)*, and *ulluco (Ullucus tuberosus)*, among others. One reason for this is that *cubio* is associated with a bitter taste, which is caused by the presence of isothiocyanates. However, these bitter compounds also serve as important phenolic antioxidants, with potential health benefits (3–5). This is why *cubio* is attributed antimicrobial (5,6), hemagglutinating, and anticoagulant properties (6).

Colombian *cubio* exhibits a range of skin colors, from white to dark violet-purple, with additional shades of yellow, orange, red, and pink. Despite its diversity and historical significance as a food source for ancient civilizations, *cubio*, along with other Andean tubers and roots such as *ibia, rubas*, and *yacón*, faces the risk of genetic erosion (7). This poses a threat to their continued existence in the territory. However, efforts to empower low-income communities through the technical knowledge and production management of these species offer a potential solution. Simple and cost-effective processes can transform these tubers into flours, beverages, nectars, jams, sweets, and bakery products, expanding their utilization and market opportunities, particularly among the younger generations, who have reduced their consumption (2).

The effort to contribute to the prevention of *cubio* erosion – note that this tuber is cultivated in undemanding soils – inspires this research to offer alternative products to those traditionally made with it, thereby preserving and expanding the market for alcoholic beverages (8), *e.g.*, in the form of a wine that meets people's expectations (9).

Considering the above, the objective of the research was to evaluate a beverage obtained through the alcoholic fermentation of the *cubio* tuber (*Tropaeolum tuberosum* R&P), specifically focusing on the Colombian variety known as *blanca ojo morado* (white purple-eyed). Winemaking techniques were applied, utilizing wine yeasts, in order to explore *cubio* as a potential raw material for alcoholic beverage production, adapting the practices used in grape wine production.

This study holds significance regarding the preservation and promotion of the use of *cubio*, a valuable yet underutilized tuber, while simultaneously offering an alternative product of good nutritional and sensory quality. By bridging traditional knowledge with modern fermentation practices, our proposal seeks to contribute to the sustainable utilization and commercialization of *cubio*, thereby benefitting local communities and safeguarding the genetic diversity of these important crops.

2. Materials and methods

2.1. Physicochemical characterization of the *cubio* tuber (*blanca ojo morado* variety)

In this study, three samples of *cubio* were analyzed in triplicate, aiming to determine the carbon and nitrogen content present in the tuber, which is utilized by the yeast during fermentation. As a carbon source, the tubers' sugars and starch contents were measured through Miller's acid hydrolysis method (10) and the procedure established in AOAC International's 985.29 method (11). Additionally, its dry matter and moisture were determined via the gravimetric method described in (12), and the protein content (nitrogen source) was measured using AOAC International's 2001.11 method (13).

2.2. Conditioning the *cubio* tuber

The process started by subjecting 2 kg of *cubio* to immersion washing, effectively removing any external impurities. To ensure proper disinfection, a solution of chlorinated alkyl dimethyl benzyl ammonium was prepared with a ratio of 1:10 (disinfectant:water), in order to treat the *cubio* tuber.

To facilitate the interaction between *cubio* nutrients and the yeast during fermentation, the tuber was liquefied. The liquefaction process aimed to break down the tuber, allowing for a better nutrient release. The filtered solids from this extract were washed across several stages, ensuring that the maximum amount of fermentable material was available. This concentration step was crucial in optimizing the fermentation process, as it provided the yeast with a richer source of sugars to convert into alcohol, thereby enhancing the efficiency and yield of the overall process. The resulting liquefied *cubio* was then adjusted to a volume of 2 L to prepare the must, which would serve as the fermentation medium. To further enhance the characteristics of the must, it was heated to 60 °C in a kettle. This heating step helped to fix the color of the *cubio* – this process potentially influences other flavor and aroma components. Following the heating process, the must was cooled down to an appropriate temperature and subsequently transferred to a BioFlo 110 bioreactor, which provided a controlled environment for the fermentation process, enabling the precise monitoring and regulation of various parameters.

By means of these specific procedures, this study aimed to optimize the preparation of cubio must for saccharification and fermentation while ensuring the desired final characteristics and qualities throughout the process.

2.3. Preparing the must for fermentation

For the subsequent steps of the fermentation process, we followed the protocol developed by (14), as modified by (15). The 2 L of liquefied and concentrated *cubio* in the bioreactor underwent pre-liquefaction and post-liquefaction, each performed under specific temperature and pH conditions.

During the pre-liquefaction stage, the liquefied *cubio* was subjected to a temperature of 70 °C and a pH of 7.0 for 60 min. This step helped to further break down the tuber components and prepare them for subsequent processes. Additionally, the enzyme α-amylase BAN 480L (50 g. hL-1 concentration) was added to facilitate the liquefaction process.

During the post-liquefaction stage, the liquefied *cubio* was maintained at a temperature of 70 °C and a pH of 5.2 for 90 min. The modified conditions of this stage helped to optimize the breakdown of starch and other complex carbohydrates present in the *cubio* tuber. The addition of the enzyme α-amylase BAN 480L at a concentration of 50 g. hL^{-1} continued to support the liquefaction process.

After the liquefaction stages, saccharification was carried out. This process was conducted at a temperature of 65 °C and a pH of 5.2. The enzyme used for saccharification was the glucoamylase enzyme Amylase AG 300L, at a concentration of 0.4 %. This glucoamylase enzyme aids in the breakdown of complex sugars such as starch into simpler, fermentable ones, providing a suitable substrate for yeast fermentation.

By following this protocol, this study aimed to optimize the liquefaction and saccharification processes of the *cubio* tuber, ensuring the efficient conversion of complex carbohydrates into fermentable sugars for subsequent fermentation by the yeast.

2.4. Alcoholic fermentation

For the fermentation process, several nutrients were added to the must in order to support yeast growth and fermentation. These nutrients included 0.1 % (NH_4) H_2PO_4, 0.3 % $MgSO_4$, 0.5 % peptone, and 0.3 % yeast extract. These ingredients provided the essential elements and necessary compounds for yeast metabolism and fermentation. Additionally, *Saccharomyces bayanus* yeast (Safale US-05) (14) was introduced into the must to initiate fermentation.

The process was carried out for 15 days at a temperature of 24 °C in a fermentation vessel maintained at 100 rpm, ensuring adequate mixing and contact between the yeast and the must. The final pH of the fermentation medium was maintained at 4.5, creating favorable conditions for yeast activity.

For the fermentation process, we measured the content of reducing sugars derived from the cubio tuber, from the concentrated extract, and from the enzymatic breakdown of starch. The monitoring process helped to assess the progress of sugar consumption by the yeast during fermentation. Furthermore, additional sugar was added to the must in order to achieve the desired alcohol content of 15 °GL (Gay-Lussac). It was determined that 17 g of sugar produces 1° of alcohol (16). Sugar was added to reach 255 g and achieve the desired alcohol content. Daily observations and measurements were recorded during the fermentation process. These included data on reducing sugars [10], biomass (determined through constant drying) (12), pH levels, and alcohol content (°GL). The collected data provided valuable insights into the fermentation behavior and the progress of sugar utilization by the yeast over time. Graphical representations of the data were created to facilitate the analysis and interpretation of the fermentation dynamics.

Upon completion of the fermentation process, the alcoholic beverage was decanted to separate it from any sediment or solids. It was then subjected to filtration to further clarify the beverage and remove any remaining particles. After filtration, the fermented beverage was bottled and stored for subsequent evaluation and analysis.

The above-presented protocol enabled the controlled fermentation of the *cubio* must, resulting in the production of an alcoholic beverage. The recorded data and subsequent analysis provided valuable information on the fermentation kinetics, alcohol production, and the overall quality of the final product.

2.5. Characterization of the obtained alcoholic beverage

To assess the physicochemical properties of the fermented beverage, three samples were taken, and each property was analyzed in triplicate to ensure the accuracy and reliability of the measurements.

The following physicochemical properties were evaluated to verify compliance with the requirements of the Colombian Technical Standard NTC 708 for fruit wines, given that there is no national standard for this type of fermented beverages (22):

- *Alcohol content* (17). The alcohol content of the fermented beverage was determined using a specific method to quantify the percentage of alcohol present. This analysis provided crucial information on the strength of the beverage.
- *pH and total and volatile acidity* (18). The pH level and the total and volatile acidity of the beverage were measured. These parameters helped to assess the acidity and balance of the final product.
- *Methanol content* (19). Methanol, a toxic alcohol, was analyzed to ensure that its concentration in the fermented beverage adhered to safe levels for consumption.
- *Total dry extract* (20). We measured the total dry extract, which represents the concentration of solids in the beverage after removing the water. This parameter gave insights into the overall composition and density of the beverage.

In addition to the physicochemical properties, certain physical characteristics of the beverage were examined, *i.e.*,

- *Color* (21). The color of the beverage was evaluated using the Hunter method and a Konica Minolta colorimeter. This method measured color by analyzing Lab* or CIELAB spatial coordinates, and it provided information on the visual appearance and hue of the beverage.
- *Density* (11). We measured the density of the beverage, which relates to its mass per unit volume. This parameter gave insights into the concentration and overall texture of the beverage.

The collected data on physical and physicochemical characteristics were subjected to statistical analysis using the Statistix software, version 10.0 (23). A completely randomized analysis of variance (ANOVA) was performed to determine significant differences between the samples. If significant differences between specific characteristics were found ($p \leq 0.05$), Tukey's variance comparison test ($p \leq 0.05$) was applied for further analysis.

This comprehensive analysis allowed for a thorough evaluation of the fermented beverage, ensuring compliance with quality standards and providing insights into its physical and chemical properties.

2.6. Sensory evaluation

The flavor, color, and aroma attributes of the *cubio* wine were evaluated in a hedonic acceptance test with five expert wine tasting panelists. The obtained results were analyzed statistically using the Statistix software, version 10 (23). Pearson's correlation coefficient was employed to assess the correlations between the attributes ($p \leq 0.05$).

3. Results and discussion

3.1. Physicochemical characterization of *cubio*

The *blanca ojo morado* variety of *cubio* exhibited an average reducing sugars content of 2.18 ± 0.002 %. This aligns closely with the findings of (24), who reported a range of 2.16-2.83 % for the same variety. The author of (25), as cited by (26), reported a significantly higher value (7.2±0.24 %) for reducing sugars in the Peruvian *cubio* variety known as *zapallo amarillo*, emphasizing the potential differences between *cubio* varieties, which may also be influenced by variations in soil quality and the agricultural practices used during cultivation.

Regarding the starch content, the tubers exhibited an average value of 1.66 ± 0.015 %. This closely aligns with the value reported by (27) for the same *cubio* variety, which was 2.20 %. The presence of starch contributed to fermentation through enzymatic synthesis, providing additional reducing sugars as a substrate for yeast in the must.

As for the protein content, the *cubio* tubers exhibited an average value of 4.48 ± 0.064 %. This value was higher than that reported by (28) for purple *cubio* tubers (1.2±0.041 %). However, it was comparable to the value observed by (27) for the same variety (5.86 %) in a crop without fertilization.

The *cubio* tubers also exhibited an average dry matter content of 14.08 ± 0.002 %, contributing with solids to the fermentation process, including reducing sugars from starch as a carbon source and proteins as a nitrogen source for the metabolic development of yeast in the must. This finding aligns closely with those recorded by (24) for the *blanca ojo morado* variety cultivated with conventional fertilization, with 14.73 % dry matter and 85.27 % water. To preserve the anthocyanins or pigments in the *cubio* tubers, conditioning activities were promptly conducted to minimize degradation (29).

3.2. Alcoholic fermentation of *cubio*

Throughout the course of the alcoholic fermentation process, parameters such as reducing sugars, biomass, alcohol generation, and pH in the must exhibited consistent trends, as illustrated in Fig. 1. These trends showed linear variations over the 15-day fermentation period.

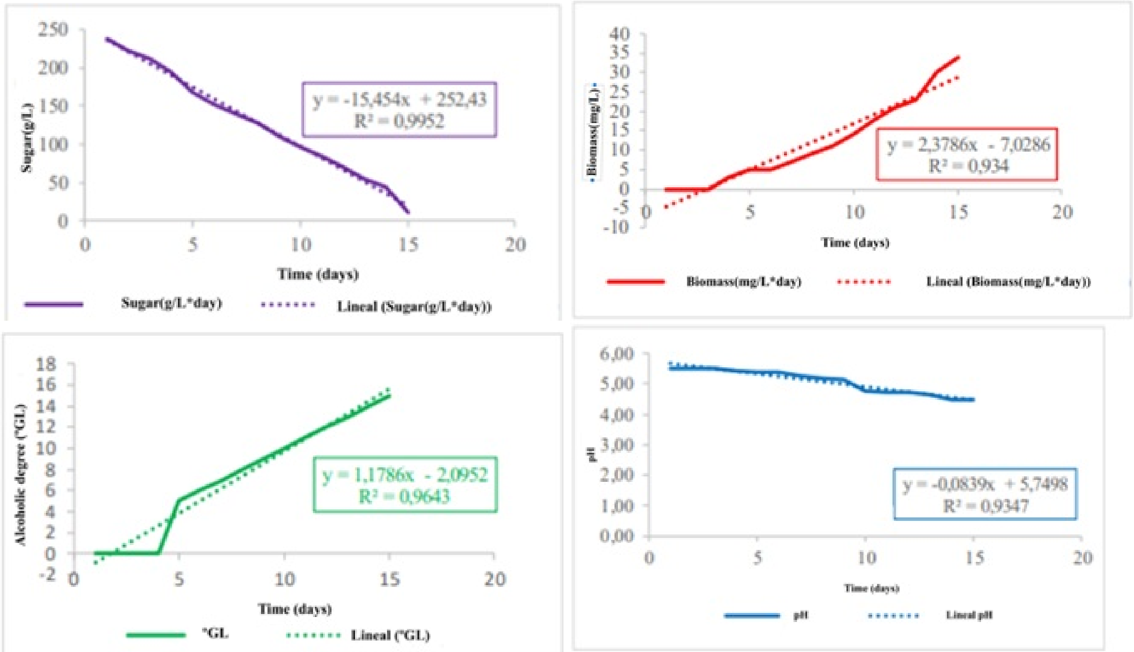

Figure 1. Alcoholic fermentation variables for the *cubio* beverage

Specifically, the *Saccharomyces bayanus* yeast employed in the fermentation process exhibited a growth rate of 2.3786 $mg.L^{-1}.day^{-1}$, given its ability to act from low-acid musts. This type of yeast can synthesize malic and succinic acid, inhibit malolactic fermentation, produce more glycerol than *Saccharomyces cerevisiae*, and generate less acetic acid (30), which indicates its capacity for multiplication and proliferation within the fermentation medium. Simultaneously, the concentration of reducing sugars experienced a gradual decrease, at a rate of 15.45 $mg.L^{-1}.day^{-1}$. This reduction can be attributed to the metabolic activity of the yeast, which utilizes the sugars as a carbon source for energy and growth.

Consequently, the fermentation process led to the production of alcohol at a rate of 1.1786 $°GL.day^{-1}$. This steady production contributed to the gradual increase in the alcohol content of the beverage over the 15-day fermentation period. By the end of the process, the alcoholic beverage had reached a final alcohol content of 15.24 °GL.

These findings highlight the dynamic nature of fermentation, with the yeast exhibiting growth, sugar consumption, and alcohol production over time. The observed trends provide valuable insights into the kinetics and outcomes of the process.

The taste and aroma of alcoholic beverages are mainly influenced by alcohol and organic compounds present in smaller quantities (31). In our work, the pH and density of the must showed changes over time, indicating that alcoholic fermentation was taking place due to yeast metabolism. The pH decreased at a rate of 0.0839 day^{-1}, and the density reached a value of 0.9947 ± 0.002 $g.cm^{-3}$.

Similar values were reported by (15) for alcoholic fermentation using fresh *Criolla* potato tubers and *Saccharomyces bayanus* yeast, with a biomass growth of 0.344 $mg.mL^{-1}.h^{-1}$, an increase of 1.8046 $°GL.h^{-1}$ in alcohol content, and a decrease of 0.0045 $mg.mL^{-1}.h^{-1}$ in reducing sugars, demonstrating a similar behavior of yeast in fermentations with other tubers.

Before racking, the alcoholic beverage showed sediment formation at a rate of 0.4657 $mL.h^{-1}$. This sedimentation confirmed that the yeast was actively transforming the components of the must through its fermentative power, degrading the sugars. The availability of nutrients in sediments during alcoholic beverage formation was confirmed by (32), including assimilable nitrogen, oxygen, vitamins, minerals, and ergosterol, as well as the presence of inhibitory substances.

3.3. Characterization of the alcoholic beverage obtained

The beverage analyzed in this study exhibited an alcohol concentration of 15.24 °GL, corresponding to 15.24 mL of ethanol per 100 mL of beverage. This value is close to that reported by (33), *i.e.*, ranging from 8.6 to 14 °GL for Brazilian grape wines; to those observed by (34), with 11.3 °GL for a *lulo* wine; and to those recorded by (35) for fermented kiwifruit beverages, with 11.8 °GL. Alcohol content is important because it affects organoleptic characteristics such as the aroma and body of the wine (33). The saccharification stage with α-amylase not only aided in alcohol production by reducing the concentrated sugars derived from *cubio* (plus the sucrose added to the process) during fermentation; it also helped to increase the degree of gelatinization and the water solubility index, as well as to reduce the water absorption index and the viscosity of tuber extracts used in wine production (36). According to (37), fermented alcoholic beverages such as wine, beer, or cider should not exceed alcohol values of 17 $g.100\ g^{-1}$ in order to maintain desirable quality characteristics and a pleasant taste. This observation validates the potential of the *cubio* tuber as a new ingredient for alcoholic beverage production.

The total acidity was 7.21 ± 0.029 $g.L^{-1}$, expressed as tartaric acid, which falls within the recommended range of 3.5 to 10 $g.L^{-1}$ for wine-like alcoholic beverages, indicating the favorable quality achieved through controlled fermentation (38). The obtained value falls within the range reported by (36), *i.e.*, between 5.45 and 8.4 $g.L^{-1}$ for tuber wines. When the total acidity expressed as tartaric acid is above 2 $g.L^{-1}$, it further supports beverage quality. Indeed, pH and acidity are closely related to the solubility of tartaric salts (39). Regarding the total acidity, (40) reported a value of 4.2 g.L^{-1} when using a *Saccharomyces cerevisiae* strain (to induce fermentation) and a different substrate such as palm (*Phoenix sylvestris*) sap. Their result was lower than ours. Diverse strains and substrates may influence the accumulation of total acidity (as tartaric acid).

The average methanol content in the beverage was 1.0327 ± 0.00079 mg.L^{-1}, indicating fermentation stability and quality. The presence of trace amounts of methanol confirms that the process was primarily focused on ethanol production, resulting in a beverage that is safe and suitable for consumption. The obtained value is below the maximum limit specified in the NTC 708 standard (<1000 mg.dm^{-3} of anhydrous alcohol) (22). It is important to mention that surpassing this limit, as noted by (41), can result in metabolic intoxication. Therefore, given its neurotoxic effects, methanol is an unwanted component in any kind of wines (35).

The density of the beverage was 0.9947 ± 0.002 mg.mL^{-1}, indicating the presence of alcohol resulting from yeast activation during the fermentation process. This density value exhibits a direct relationship with the concentration of sugars in the beverage. Similar results were obtained by (42) in the production of a non-distilled alcoholic beverage from milk, where a density value of 1.034 was reported. Furthermore, (40) reported values of 0.99 mg. mL^{-1}, and (43) recorded 0.9916 and 1.0174 mg. mL^{-1} for Peruvian grape wines.

The pH of the beverage was 4.585 ± 0.0018, which falls within the optimal range and is similar to that obtained by (40) (4.2) and by (44) (4.5) during the fermentation of palm sap and coffee husk and mucilage, respectively, resulting in an alcoholic beverage with favorable sensory characteristics. The pH of our beverage was 4.5, which is consistent with the fermentation process of alcoholic beverages, as it started from 5.74 (the pH of *cubio*). Due to the nature of the tuber, values as low as those in traditional wine were not achieved, but microbiological safety was ensured.

3.4. Sensory evaluation of the *cubio* beverage

Fig. **2** shows the aspects rated in the sensory panel by the experts, with the highest score for flavor, followed by those for aroma and color. The panelists described the beverage as having a floral-fruity aroma and a semi-sweet flavor, indicating the presence of volatile compounds derived from fatty acids, carbohydrates, and amino acids produced in the biosynthetic pathway (45). This is because *Saccharomyces bayanus* has been linked to a higher yield of glycerol, lactic acid, succinic acid, malic acid, and, especially, acetate and ethyl ester, in comparison with other strains used in alcoholic fermentation such as *Saccharomyces cerevisiae* (46). The floral aroma may be attributed to the fact that *Saccharomyces bayanus* can produce 2-phenylethanol (2-PE), a highly valuable aromatic alcohol with a rose-like aroma (30).

Regarding the color characteristics of the beverage, the panelists described it as bright lilac, which corresponds to values of 47.76±0.05 L*, 17.16±0.03 a*, and -23.84±0.08 b* in the CIELAB coordinate diagram. These values place the beverage in the red-blue chromatic zone with intermediate brightness, which is lighter compared to red grape wines. The positive L* value indicates a beverage with higher luminosity. The presence of acids in the beverage influences its color and aroma, since they act as antimicrobial agents during the production process (47). In comparison with the characteristics found in wines, pigmentation in the tuber beverage was achieved using 30-40 % of the pigments present in the raw material. Furthermore, copigmentation reactions involving hydroxycinnamic acids and flavonoids influenced the coloration of anthocyanins, contributing to the overall color profile (48). The aroma produced was linked to the alcohol content, acidity, dry extract, total and reducing sugars, and body of the wine (33).

The type of packaging is crucial to preserve the properties of wine, including its flavor, aroma, and overall quality, as appropriate materials can prevent oxidation and other chemical reactions that may degrade it over time. According to (49), selecting the right container is essential for maintaining the stability of bioactive compounds, particularly in wines derived from less conventional sources, as is the case of *cubio*.

As shown in Fig. **2**, the values for each of the independent variables range between 1 and 3, demonstrating a good product acceptance. When the attributes were statistically correlated (data not presented), a low relationship was found between color and flavor and aroma, possibly due to a low correlation.

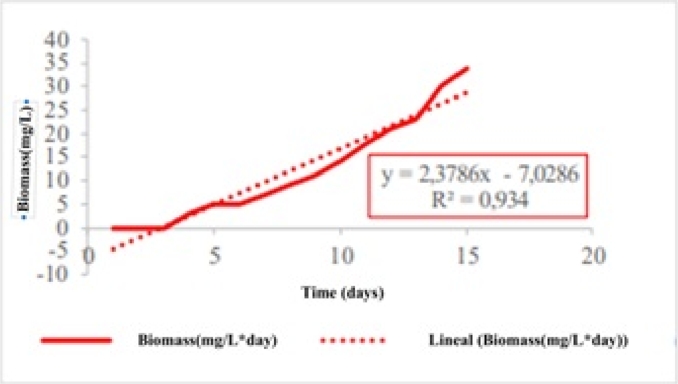

Figure 2. Sensory evaluation results obtained for the *cubio* alcoholic beverage. 1: I like it very much. 2: I like it slightly. 3: I neither like nor dislike it. 4: I dislike it slightly. 5: I dislike it very much.

4. Conclusions

Based on the experimental data, the *cubio* tuber was found to be a viable raw material for obtaining a fermented alcoholic beverage. The characterization of the Colombian *blanca ojo morado* variety of *cubio* revealed its potential as a valuable source of carbohydrates, including reducing sugars (2.18±0.002 %), starch (1.66±0.015 %), and proteins (4.48±0.064 %). These constituents served as substrates for yeast growth and subsequent fermentation. The stages of concentration and the incorporation of α-amylase and glucoamylase enzymes in the fermentation must increased the concentration of reducing sugars, providing a more favorable substrate for yeast metabolism and ultimately facilitating the production of ethanol.

The alcoholic beverage reached a pH value of 4.5, a total acidity of 7.21 ± 0.029 $g.L^{-1}$, a density of 0.9947 $mg.mL^{-1}$, and an alcohol concentration of 15.24 °GL. The concentration of reducing sugars experienced a gradual decrease, at a rate of 15.45 $mg.L^{-1}.day^{-1}$, and the production of alcohol reported a rate of 1.1786 $°GL.day^{-1}$. All these values correspond to an optimal fermentation process. A sensory evaluation conducted by expert panelists yielded favorable ratings for the flavor and aroma characteristics of the beverage.

This suggests that the *cubio* tuber holds promise as an alternative ingredient for the production of high-quality alcoholic beverages, encouraging further exploration and research into the utilization of these ancestral tubers. Moreover, their high nutritional value underscores their potential as a promising food source for the future.

5. CRediT author statement

Martha Morantes: methodology, investigation, writing (original draft). **Alfredo López-Molinello:** conceptualization, investigation, methodology, supervision, validation, visualization, writing (review & editing). **Ismael Povea:** visualization, writing (review & editing). **Lena Prieto:** conceptualization, investigation, methodology, project administration, supervision, validation, writing (original draft, review & editing). **Santiago Sáenz:** visualization, writing (review & editing)

References

[1] FAO, “Promover los cultivos marginados e infrautilizados,” 2017. [Online]. Available: `http://www.fao.org/news/story/es/item/1032703/icode/` ↑3

[2] S. Sáenz-Torres, A. López-Molinello, L. Prieto, and T. Rodríguez, “El cubio como una alternativa productiva sostenible en condiciones de agricultura urbana de Bogotá,” *Eq. Des.*, vol. 34, pp. 121-142, 2019. `https://doi.org/10.19052/eq.vol1.iss34.6` ↑3

[3] R. Chirinos, H. Rogez, D. Campos, R. Pedreschi, and Y. Larondelle, “Optimization of extraction conditions of antioxidant phenolic compounds from mashua (*Tropaeolum tuberosum* Ruíz & Pavón) tubers,” *Sep. Pur. Tech.*, vol. 55, pp. 217-225, 2007. `https://doi.org/10.1016/j.seppur.2006.12.005` ↑3

[4] O. Ortega, D. Kliebenstein, C. Arbizu, R. Ortega, and C. Quiros, “Glucosinolate survey of cultivated and feral mashua (*Tropaeolum tuberosum* Ruíz & Pavón) in the Cuzco region of Perú,” *Econ. Botany*, vol. 60, no. 3, pp. 254-264, 2006. `https://doi.org/10.1663/0013-0001(2006)60[254:GSOCAF]2.0.CO;2` ↑3

[5] F. M. Mejia, J. E. Salcedo, and S. Vargas, “Capacidad antioxidante y antimicrobiana de tubérculos andinos (*Tropaeolum tuberosum* y *Ullucus tuberosus*),” *Rev. U.D.C.A.*, vol. 21 no. 2, pp. 449-456, 2018. `https://doi.org/10.31910/rudca.v21.n2.2018.1083` ↑3

[6] P. Djabayan, L. González, M. Lucena, and C. Valarezo, “Aislamiento y actividad biológica de lectinas obtenidas de semillas de frutas, granos y tubérculos de plantas andinas,” *Info. Tecnol.*, vol. 33, no. 2, pp. 21-36, 2022. `https://doi.org/10.4067/S0718-07642022000200021` ↑3

[7] A. C. Morillo, Y. Morillo, and Y. P. Tovar, “Caracterización molecular de cubios (Tropaeolum tuberosum Ruíz y Pavón) en el departamento de Boyacá,” *Rev. Cien. Agr.*, vol. 33, no. 2, pp. 32-42, 2016. `http://dx.doi.org/10.22267/rcia.163302.50` ↑3

[8] S. E. Aguirre, N.V. Piraneque, and I. Pérez, “Sistema de producción de tubérculos andinos en Boyacá, Colombia,” *Cuad. Des. Rural*, vol. 9, no. 69, pp. 257-273, 2012. ↑3

[9] M. B. Suquilanda-Valdivieso, “Producción orgánica de mashwa (*Treopaeolum tubersum*),” en *Producción orgánica de cultivos Andinos (Manual Técnico)*, M. B. Suquilanda-Valdivieso, Ed., Ecuador: FAO, UNOCANC, Ministerio de Agricultura, Ganadería, Acuacultura y Pesca, 2012, ch. 2, pp. 19-31. `http://www.fao.org/familyfarming/detail/en/c/384373/` ↑3

[10] G. Miller, “Use of dinitrosalicylic acid reagent for determination of reducing sugar,” *Analytical Chem.*, vol. 31, pp. 426-428, 1959. `https://doi.org/10.1021/ac60147a030` ↑4

[11] *Density of sucrose solutions at 0-100°C and 0-70 %*, Official Method of Analysis 962.37, AOAC International, 1995. ↑4, 7

[12] *Protein (crude) in animal feed, forage (plant tissue), grain, and oilseeds, Block digestion, Steam distillation method*, Official Method of Analysis 2001.11, AOAC International, 2005. ↑4, 6

[13] *Ash and fruit products, gravimetric method, alkalinity*, Official Method of Analysis 940.26, AOAC International, 2005. ↑4

[14] Y. Göksungur and U. Güvenç, “Enzymatic hydrolysis and production of ethanol from potato starch,” *Gida*, vol. 19, no. 2, pp. 89-92, 1994. ↑5

[15] L. Sánchez and L. M. Triviño, “Obtención de alcohol etílico a partir de la fermentación de *Saccharomyces bayanus*, en un clon promisorio de papa criolla en (*Solanum tuberosum Grupo Phureja*) cosechado en el Municipio de El Rosal,” undergraduate thesis, Escuela de Ciencias Básicas, Tecnología e Ingeniería, Universidad Nacional Abierta y a Distancia, Colombia, 2014. ↑5, 9

[16] A. Ronquillo, R. Lazcano, I. Pérez, S. Cabrera, and S. Lazcano, “Elaboración y caracterización de vino de frutas e infusión de hierbas,” *Inv. Des. Cien. Tecnol. Alim.*, vol. 1, no. 1, pp. 366-371, 2016. ↑6

[17] *Bebidas alcohólicas. Métodos para determinar el contenido de alcohol*, Norma Técnica Colombiana NTC 5113, ICONTEC Internacional, Colombia, 2003. ↑6

[18] *Bebidas alcohólicas. Métodos para determinar la acidez y el pH*, Norma Técnica Colombiana NTC 5114, ICONTEC Internacional, Colombia, 2003. ↑6

[19] *Bebidas alcohólicas. Método colorimétrico para determinar el contenido de metanol*, Norma Técnica Colombiana NTC 5159, ICONTEC Internacional, Colombia, 2003. ↑6

[20] *Bebidas alcohólicas. Método para determinar el extracto*, Norma Técnica Colombiana NTC 5162, ICONTEC Internacional, Colombia, 2003. ↑6

[21] *Colorimetry-Part 6: CIEDE 2000-Colour difference formula*, ISO/CIE 11664-6:2014, International Organization for Standardization ISO, 2014. ↑7

[22] *Bebidas alcohólicas. Vinos de frutas*, Norma Técnica Colombiana NTC 708, ICONTEC Internacional, Colombia, 2000. ↑6, 10

[23] *Statistix 10. Data analysis software for researchers*. (2013). Analytical Software. ↑7

[24] S. Sáenz-Torres, L. Prieto, and A. López-Molinello, *El cubio (Mashua): producción, transformación y beneficios*, Bogotá, Colombia: Ediciones Unisalle, 2020. `https://doi.org/10.19052/9789585148413` ↑7, 8

[25] B. Aguado, "Influencia del tiempo de soleado sobre la concentración de azúcares reductores y capacidad antioxidante de la mashua (*Tropaeolum tuberosum*) ecotipo negra," undergraduate thesis, Escuela Profesional de Ingeniería Agroindustrial, Universidad Nacional de Huancavelica, Perú, 2017. ↑7

[26] D. Arteaga, L. Chacón, V. Samame, D. Valverde, and L. M. Paucar, "Mashua (*Tropaeolum tuberosum*): composición nutricional, características químicas, compuestos bioactivos y propiedades beneficiosas para la salud," *Agroind. Sci.*, vol. 12, no. 1, pp. 95- 101, 2022. `https://doi.org/10.17268/agroind.sci.2022.01.12` ↑7

[27] D. Romero and L. Tuirán, "Caracterización fisicoquímica, funcional, reológica y composicional de la harina precocida de cubio (*Tropaeolum tuberosum* R&P) cultivado en diferentes fuentes de fertilización," undergraduate thesis, Department of Engineering, Universidad de La Salle, Colombia, 2017. ↑7

[28] F. Velásquez, E. Ramirez, R. Chuquilin, and I. Aliaga, "Optimization of the functional properties of a drink based on tubers of purple mashua (*Tropaeolum tuberosum* Ruíz y Pavón," *Agroind. Sci.*, vol. 10, no.1, pp. 63-70, 2020. `https://doi.org/10.17268/agroind.sci.2020.01.09` ↑7

[29] A. Castañeda-Sánchez and J. A. Guerrero-Beltrán, "Pigmentos en frutas y hortalizas rojas: antocianinas," *Temas Sel. INg. Alim.*, vol. 9, no. 1, pp. 25-33, 2015. ↑8

[30] Y. Zhao, S. Li, Q. Shu, X. Yang, and Y. Deng, "Highly efficient production of 2- phenylethanol by wild-type *Saccharomyces bayanus* strain," *Biores. Tech.*, vol. 403, no. 1, pp. 1-10, 2024. `https://doi.org/10.1016/j.biortech.2024.130867` ↑8, 10

[31] H. Kretzschma, *Levaduras y alcoholes y otros productos de la fermentación*, Barcelona, Spain: Editorial Reverté, 1998. ↑9

[32] I. S. Pretorius, "Tailoring wine yeast for the new millennium: Novel approaches to the ancient art of winemaking," *Yeast*, vol. 15, pp. 675-629, 2000. `https://doi.org/10.1002/1097-0061(20000615)16:8<675::AID-YEA585>3.0.CO;2-B` ↑9

[33] M. Bonatto, M. Gonçalves, A. C. Conti-Silva, and V. Luiz, "Influence of two different vinification procedures on the physicochemical and sensory properties of Brazilian non-Vitis vinifera red wines," *LWT Food Sci. Tech.*, vol. 54, no. 2. pp. 360-366, 2013. `https://doi.org/10.1016/j.lwt.2013.06.020` ↑9, 11

[34] C. Granados, M. E. Torrenegra, D. Acevedo, and P. Romero, "Evaluación fisicoquímica y microbiológica del aperitivo vínico de lulo (*Solanum quitoense* L.)," *Información tecnológica*, vol. 24, no. 6, pp. 35-40, 2013. `https://dx.doi.org/10.4067/S0718-07642013000600006` ↑9

[35] D. Huang, Y. Zhong, Y. Liu, Y. Song, X. Zhao, and Y. Qin, "Reducing higher alcohols by integrating indigenous *Saccharomyces cerevisiae*, nitrogen compensation, and chaptalization methods during fermentation of kiwifruit wine," *LWT*, vol. 184, p. 115059, 2023, doi: `https://doi.org/10.1016/j.lwt.2023.115059` ↑9, 10

[36] S. Bian *et al.*, "Effects of the addition of thermostable α-amylase on the physicochemical and antioxidant properties of extrusion-pretreated *Apios fortunei* used for yellow wine fermentation," *LWT*, vol. 154, p. 112845, 2022. `https://doi.org/10.1016/j.lwt.2021.112845` ↑9

[37] E. Kolb, *Vinos de frutas elaboración artesanal e industrial*, Zaragoza, Spain: Editorial Acribia S.A., 2002. ↑9

[38] D. Ming-Yu, H. Koizumi, and Y. Suzuki, "Comparison of three chromatographic systems for determination of organic acids in wine," *Analytical Sci.*. vol. 11, no. 2, pp. 239-243, 1995. `https://doi.org/10.2116/analsci.11.239` ↑9

[39] A. Pastore, D. Badocco, L. Cappellin, M. Tubiana, and P. Pastore, "Real-time monitoring of the pH of white wine and beer with colorimetric sensor arrays (CSAs)," *Food Chem.*, vol. 452, p. 139513, 2024, doi: `https://doi.org/10.1016/j.foodchem.2024.139513` ↑10

[40] N. Khadka *et al.*, "Study on the changes during the fermentation of the wine prepared from palm (Phoenix sylvestris) sap," *Heliyon*, vol. 10, no. 15, p. e35799, 2024. `https://doi.org/10.1016/j.heliyon.2024.e35799` ↑10

[41] L. García, M. Flórez, C. Marrugo, and Y. Ligardo, "Elaboración y caracterización fisicoquímica de un vino joven de fruta de borojo (*B patinoi Cuatrec*)," *Cien. Doc. Tecnol.*, vol. 27, no. 52, pp. 507-519, 2016. ↑10

[42] L. M. Quispe, "Obtención de una bebida alcohólica a partir de la fermentación de leche," *Rev. Inv. Cien. UNTRM: Cien. Nat. Ing.*, vol. 1, no. 3, pp. 46-51, 2018. `https://doi.org/10.25127/ucni.v1i3.425` ↑10

[43] R. Salazar, G. Espinoza, C. Ruiz, M. F. Fernández, and R. Rojas, "Compuestos fenólicos, actividad antioxidante, contenido de resveratrol y componentes del aroma de 8 vinos peruanos," *Rev. Soc. Quím.* Perú, vol. 77, no. 2, pp. 135-143, 2011. ↑10

[44] S. V. Olivares, M. Silva, and R. A. Caruajulca, "Bebida alcohólica por fermentación de cáscara y mucilago del café (*Coffea arabica* L.) a diferente pH y concentración de levadura," *Rev. Inv. Cien. UNTRM: Cien. Nat. Ing.*, vol. 3, no. 1, pp. 9-15, 2020. `http://dx.doi.org/10.25127/ucni.v3i1.586` ↑10

[45] F. J. Francis and P. C. Markakis, "Food colorants: Anthocyanins," *Crit. Rev. Food Sci. Nut.*, vol. 28, no. 4, pp. 273-314, 1989. `https://doi.org/10.1080/10408398909527503` ↑10

[46] J. Liu *et al.*, "Ethyl esters enhancement of Jinchuan pear wine studied by coculturing *Saccharomyces bayanus* with *Torulaspora delbrueckii* and their community and interaction characteristics," *Food Biosci.*, vol. 46, art. 101605, 2022. `https://doi.org/10.1016/j.fbio.2022.101605` ↑10

[47] P. Ribéreau, D. Dubourdieu, B. Donèche, and A. Lonvaud, *Handbook of enology: The microbiology of wine and vinifications*, London, UK: John Wiley & Sons, 2006. ↑11

[48] S. J. Bloor and R. Falshaw, "Covalently linked anthocyanin-flavonol pigments from blue *Agapanthus* flowers," *Phytochem.*, vol. 53, no. 5, pp. 575-579, 2000. `https://doi.org/10.1016/S0031-9422(99)00572-5` ↑11

[49] I. Povea, *La función del envase en la conservación de alimentos*, Bogotá, Colombia: ECOE Editores, 2014. ↑11

Martha Morantes

Food engineer, Universidad de la Salle, Bogotá, Colombia
Email: mmorantes42@unisalle.edu.co

Alfredo López-Molinello

Food microbiologist from Universidad de Pamplona; MSc in Microbiology from Universidad Nacional de Colombia. Associate professor of the Food Engineering program at Universidad de la Salle, Bogotá, Colombia. Member of the Agrifood, Biotechnological and Chemical Processes research group (MinCiencias). Member of the Colombian Association of Food Science and Technology (ACTA). Speaker at national and international events. Author of articles in indexed scientific journals, as well as of books and book chapters.
Email: alopez@unisalle.edu.co

Ismael Povea

Food engineer, Universidad de la Salle; MSc in Packaging from Michigan State Univesity. Eight published papers in Colombian journals and one in an international journal. Author of the book titled *Role of packaging in food conservation*. International Consultant. Four articles in Colombian newspapers. Fourth highest GPA in the Quality Management specialization program. Third highest GPA during undergraduate studies. Professor, researcher, leader; highly committed to achieving goals.
Email: ipovea@unisalle.edu.co

Lena Prieto

Chemical engineer with a Master's degree in Education, and specialist in Virtual Learning Environments. Undergraduate and postgraduate teacher at Pontificia Universidad Javeriana and Universidad de La Salle. She participates in research projects on food and agro-industrial topics, with national recognition by AGROSAVIA, the Colombian Agricultural Research Corporation, and international recognition by the Regional Fund for Agricultural Technology. As a legacy of her 20 years' worth of teaching, she has written university texts, virtual courses, and scientific articles. She also participated in the Agro-industrial Systems, Processes, and Products Design module of the ICFES state exams.
Email: lprieto@unisalle.edu.co

Santiago Sáenz

Agricultural engineer from Pontificia Universidad Católica del Perú. Master and PhD in Sustainable Agriculture from Universidad Nacional Agraria la Molina, Peru. Specialist in Educational Management from Universidad de la Sabana and in University Teaching from Universidad Santo Tomás. Associate professor of the Agronomic Engineering program at Universidad de La Salle, Yopal campus, Colombia.
Email: ssaenz@unisalle.edu.co

UNIVERSIDAD DISTRITAL
FRANCISCO JOSÉ DE CALDAS

Ingeniería

https://revistas.udistrital.edu.co/index.php/reving/issue/view/1241

DOI: https://doi.org/10.14483/23448393.21253

Research

Bolstering the Spatial Rotation Ability to Understand the Topics of Point and Line in Descriptive Geometry[*]

Potencialización de la habilidad espacial de rotación para comprender las temáticas del punto y línea en geometría descriptiva

Hernando Parra Lara[1][**] and Carlos Alberto Ospina Parra[2]

[1]Universidad Tecnológica de Pereira, Pereira, Colombia
[2]Universidad de Manizales. Manizales. Colombia

Abstract

Objective: The main objective is to determine how the spatial rotation ability (HER) is enhanced in first-year engineering students of Universidad Tecnológica de Pereira (UTP).

Methodology: A qualitative study is proposed which is aimed at understanding the role of students' prior ideas in the development of the HER. Initially, a test (PSVT: R) is administered to a group of students as a pre-test. Four of these students are selected using a Student's t-test. Then, an instrument that measures the notions regarding the concepts of *point* and *line* that students have developed since childhood is applied.

Results: After conducting the post-test, progress in the students' HER is evident. This difference was statistically significant ($p<0.05$). The tests of the four selected students were analyzed using the Atlas ti software.

Conclusions: The development of the HER was evidenced in the results of the normalized PSVT: R post-test, implying the evolution of students' (previous, vague, and imprecise) ideas regarding 3D notions of point and line.

Keywords: spatial ability, previous ideas, pre-test, post-test, descriptive geometry

Article history

Received:
14th /Oct/2023

Modified:
10th /Mar/2024

Accepted:
25th /Apr/2024

Ing, vol. 29, no. 3, 2024, e21253

---

[*] This scientific research article is derived from the Doctoral thesis titled *Understanding the spatial skills of rotation in the learning of descriptive geometry by first-year students of Universidad Tecnológica de Pereira*, linked to the Doctoral program in Didactics, Faculty of Educational Sciences, Universidad Tecnológica de Pereira.

[**] **Correspondence:** heparra@utp.edu.co

Resumen

Objetivo: El objetivo principal es determinar cómo se potencializa la habilidad espacial de rotación (HER) en estudiantes de primer año de ingeniería de la Universidad Tecnológica de Pereira (UTP).
Métodología: Se propone un estudio cualitativo orientado a comprender el rol de las ideas previas de los estudiantes en el desarrollo de la HER. Para ello, inicialmente se aplica una prueba (PSVT: R) a un grupo de estudiantes a manera de *pre-test*. Se seleccionan cuatro de estos estudiantes mediante una prueba t de Student. Luego, se aplica un instrumento que mide las nociones sobre los conceptos de *punto* y *línea* que los estudiantes han desarrollado desde su infancia.
Resultados: Una vez realizado el *post-test*, se evidencia el progreso en la HER de los estudiantes. Esta diferencia fue estadísticamente significativa ($p<0.05$). Las pruebas de los cuatro estudiantes seleccionados fueron analizadas mediante el *software* Atlas ti.
Conclusiones: Se evidenció el desarrollo de la HER en los resultados del *post-test* normalizado PSVT: R, lo que implica la evolución de las ideas (previas, vagas e imprecisas) de los estudiantes respecto a nociones en 3D sobre el punto y la línea.

Palabras clave: habilidad espacial, ideas previas, *pre-test*, *post-test*, geometría descriptiva

Table of contents

1. Introduction

Through the testing of previous ideas regarding point and line, students sharpen their understanding of grounding and palpation, as through a duct or a pipe in 3D. They can visualize and imagine the relationship of a point seen from a plan view with the same line, albeit represented in an elevation view. This allows them to improve their ability to retain information, which is essential when performing or re-performing post-tests (PSVT:R).

Through the development of the spatial ability of rotation (HER), first-year students acquire the method for and faculty of learning the aforementioned subject in the field of descriptive geometry and in all STEM areas (science, technology, engineering, and mathematics).

Testing previous ideas regarding point and line enables the utilization of tools, such as software, that allow students to dynamize their HER.

As for spatial abilities, various studies have been conducted, mainly in the field of psychology (1), in the form of meta-analysis of the characterization of said ability in relation to gender differences, as well as regarding the classification of the spatial relations associated with the ability to quickly rotate and visualize figures in two or three dimensions (mental rotation) and with the ability to mentally manipulate visual information through staged or sequential analysis, imagining the rotations of objects in space. This is especially useful in engineering graphics.

When referring to spatial skills, special emphasis must be placed on mental rotation, which facilitates the accurate and quick rotation of 2D and 3D figures. This is supported by spatial orientation, allowing students to physically or mentally orient themselves in space. In a meta-analysis of the difficulties of 2D and 3D rotation (1), three spatial skills were identified: 1) spatial orientation, which requires students to locate horizontal or vertical positions on a stationary screen while ignoring distracting information and any difficulties in locating themselves in space (preconceptions); 2) mental rotation, *i.e.*, the ability to imagine how objects appear when rotated in two- or three-dimensional space; and 3) spatial visualization, or the ability to manipulate complex spatial information when one requires multiple steps to produce a correct solution.

Spatial ability (2) refers to the ability to generate, maintain, and manipulate abstract visual images. It has been divided into two hierarchies: spatial visualization, known as *spatial vision* and described as the ability to manipulate, rotate, and mentally invert objects from graphic representations; and *spatial orientation*, which depends on laterality and psychomotor development, allowing students to orient themselves physically or mentally in space (3).

For the development of spatial skills, the following tools have been used: manual sketching to perform spatial maneuvers with bodies, perspectives, views, sections, rotations, and symmetries, and the development of surfaces or folds, *etc.* (4); and tools such as Texas A&M University's SketchTivity, which uses advanced technology to provide timely information and feedback to enhance instruction and motivation in learning to draw (5).

The use of information and communication technologies (ICTs), combined with AutoCAD's 2D and 3D capabilities in explaining topics of descriptive geometry (6), as well as the use of augmented reality (AR) for teaching in this area (7), aims to stimulate students' interest in the use of technology and develop perception and spatial analysis skills.

Other works on spatial skills have focused on spatial memory. First-year college students appear to have spatial working memory (SWM), which refers to the system of psychological processes and representations underlying the ability to remember the location of objects in the world for short periods of time (8). Some of the information initially held in the working memory can be retained for longer periods of time and eventually stored in the long-term memory (9).

These works show that spatial information regarding the position of a stimulus should be stored briefly before subsequent rotations, especially in processes requiring multiple rotations or steps. Moreover, it has been claimed that additional storage is necessary to retrieve target rotation sequences with the aim of comparing the target and the potential stimuli after obtaining a multi-step solution.

SWM is considered to be of great importance for students' space and as a psychological mechanism inherent to mental rotations (10,11).

Other research works have focused on mental rotation and mental folding (12) and their similarities and differences from various perspectives (definitions, cognitive processes, components, neurological bases, developmental trajectories, malleability, predictive validity, and psychometric properties), in addition to studying the marked gender differences in mental rotation.

Another study examined the relationship between mental rotation, performance in mathematics, and mathematical self-perception in 113 high school students (13).

Interpreting a landscape requires understanding the relationships between the map, the represented space, and the observer, for which it is necessary to use spatial thinking when solving spatial problems. This is done through the spatial orientation test (perspective taking/spatial orientation test), which is aimed at measuring the spatial orientation component. The results show that map-based tasks are more efficient than route-based ones. Strategies using 2D and a 2D/3D combination are more efficient than those using only 3D (14). Using the same measurement tool and the same population cohort allowed for comparisons based on quantitative data. Data from all these workshops were collected in a single study. By using statistical inference methods and comparisons between different factors, the most effective combinations of variables in the development of spatial orientation could be identified.

Spatial orientation depends on memory capacity and, to a large extent, on the process of lateralization and psychomotor development. In addition, it is governed by the categories of space and time that we use to understand our environment, to remember it, and to react accordingly, with the purpose of processing all the external information received (15). Today, it is emphasized that spatial skills are essential for many applications, especially for STEM education (16). The current goal is to use active learning strategies to develop experiences with the STEM approach, for which it is necessary to integrate innovative and creative teaching practices that allow developing spatial skills. Here, the teacher should be an instigator of doubts and a shaper of intentions, allowing students to propose solutions to problems of their community.

1.1. Prior ideas

The state of the art on prior ideas in engineering freshmen (first-year students) focuses on the elaboration of didactic units for subjects in areas such as mathematics, physics, and chemistry, among others. This design is based on the knowledge of prior ideas and the identification of students' learning styles (17).

Students, when faced with formal instruction, bring their own ideas about the natural phenomena to be taught in the classroom, *i.e.*, they have prior mental schemas (18). These schemas allow subjects to interpret the information imparted and significantly influence the understanding of scientific concepts. Knowledge of students' prior ideas should lead the teacher in planning a didactic unit while aiming to achieve conceptual change (19).

Students are not blank slates when they arrive at the university, nor do they remain frozen in time. From the moment they acquire the skills to question prior knowledge, the university campus becomes a space for transformative growth, as they strive to understand themselves in the face of academic changes and their vision of themselves as researchers (20).

The factors that influence the development of spatial skills are related to students' previous experiences. According to (21), the factors that seem to be significant in students with well-developed spatial skills, whose absence can hinder development, are as follows: having played with construction games during childhood (Lego, blocks, and puzzles); having participated in workshops or product development or mechanics classes in high school (having studied at a university with a vocational technical modality); having used 3D computer games or video games (the spatial attention capacity improves when players train in a persistent way, perfecting their working memory capacity); having participated in some types of sports; and having well-developed mathematical skills.

This includes students who were born in geographic locations where they had to develop their spatial skills for survival and work from an early age, as well as those who were fortunate enough to be born into a household of professionals in the arts, engineering, architecture, crafts, general manufacturing, and areas dedicated to industrial and automotive mechanics.

How students think from the perspective of what they bring to their minds is essential in research. This is a complex and meticulous construct, influenced by beliefs, innate characteristics, and learning histories. The mere fact of tapping into this potential inherent in their human condition allows this work to empower students to become the best they can be, as well as to acquire the skills and motivation to learn when testing prior ideas in 3D. This involves the concepts of *point* and *line* when, within the area of descriptive geometry, they decipher or reveal the solution to real 3D problems in a 2D surface.

Regarding the preconceptions of first-year engineering students, our initiative is structured to transform what they know, how they know, why they know, and their captivation, fascination, or interest (22) into learning dynamics that allow them to automatically relate their prior knowledge of point and line to the 3D and 2D reality of the preconceptions test. This, in order to spark their interest and curiosity in this subject of descriptive geometry.

Currently, at the university, students can enroll in technical programs (engineering and technology) without having taken any technical drawing subject. This allows for the coexistence of young people with no previous knowledge of geometry and those who, although they studied drawing in high school, have not developed their spatial vision skills (23).

1.2. Theoretical framework

The school that supports this research work is pragmatism; objective knowledge may be impossible, so truth can be redefined as that which functions within our limited way of experiencing reality. As indicated by Pierce, ”consider the effects of the objects of your conception. Then, your conception of these effects is the totality of your conception of the object" (24, p. 33).

The real first lesson we are entitled to when learning logic is how to clarify our ideas. However, it is unquestionable that, for an individual, it is much more valuable to have a few clear ideas than to have many confusing ones:

> It is terrible to see how a single confused idea, a single formula without significance, hidden in the head of a young person acts, sometimes, as the obstruction of an artery by inert matter, preventing cerebral irrigation and condemning its victim to perish in the fullness of his intellectual vigor and amidst intellectual abundance. (24, p. 173)

For (25, p. 35), to be thoughtful means to be logical; such a person *ties the dots*, recognizes, calculates, risks an explanation: ”the real potential of intellectual education is the transformation of natural potentialities into proven and experienced abilities". Reflective learning is contextualized knowledge; it means contemplating knowledge with regard to its relations with other things. Reflective learning opens the door to a new logic of thought: that of understanding the third dimension (26).

The prior ideas that students bring with them regarding the concepts of *point* and *line* are linked to their personality, upbringing, informative experiences (in primary and middle school), and social context. These ideas are part of each student’s particular history.

As a first contribution to the urgent need to identify students who can rotate figures in 2D and 3D and implicitly execute the conversion from 2D to 3D, it is necessary to identify, by means of standardized tests (PSVT:R), the population to be intervened. This testing process was developed and implemented by (27). It has 30 items, and it provides a model in its original state, which is then rotated in any of the three Cartesian axes. This rotation model is called *matrix rotation.* This test also provides an exercise proposal consisting of a solid in its original state. Five possible answers are given on how that solid should be rotated with regard to the rotation shown in the matrix. This first perspective, called *diagnostic*, will allow determining, through a qualitative approach, the percentage of students in each of the aforementioned categories.

The current importance of point and line study for an engineering student lies in its contribution to the maturation of spatial reasoning (*i.e.*, the student’s ability to imagine a body in different positions). This is something that every engineering student must cultivate from the first semesters, in order to build a solid foundation that allows them to address the difficulties and demands of the subjects in the curriculum, which necessitate a HER.

Spatial reasoning involves a student’s ability to create drawings, elaborate 3D structures, and visualize the shape and surface of a completely finished object before it is built (28).

The study of point and line is currently important for graduating engineers because it is related to the competence of communication, which allows them to decipher, interpret, explain, convince, know, perceive, and grasp projects with words and not with equations.

The concepts of *point* and *line*, understood and assimilated by engineering students at the beginning of their studies, are transversal to the curriculum and are fundamental in the contents of engineering programs. Students must apply these concepts while making themselves understood to all audience levels.

Capitalizing on how points and line move within a parallelepiped in the three main planes of projection, the auxiliary planes of elevation, and the auxiliary planes is enriching for engineers when it comes to using the appropriate language and linking explanations with understanding, especially regarding a topic related to some area of engineering or a tool for everyday life.

The line the trajectory of a moving point that moves constantly and in the same direction will always represent, for instance, the route of an airplane, the trajectory of a missile, the path of a tunnel, the course of a road, the layout of a viaduct, or the design of a hot air extraction duct, among others. This is also included in the calculation of slope, bearing, true length, and position coordinates. It is an invaluable tool to generate mental resources that aid in solving any problem in professional life. Design is a key element in contemporary engineering education, with design projects now playing a fundamental role in several first-year engineering courses (29).

Descriptive geometry is not an old-fashioned tool for engineers. This field is a part of the graphic expression of architecture (30) and has to do with graphic language, or the set of rules that enable the graphic communication of space through drawing and the methodology of geometry. In addition, when the mathematician Gaspar Monge, its creator, dubbed it as a language necessary to the engineer when conceiving a project, he immortalized it as a science that allows solving problems related to the geometry of space, where representations are built from 3D into 2D, and *vice versa*, through the construction of ideas. The mathematician Theodore Olivier distinguished two distinct fields: the geometrical one, with its abstract and theoretical character of spatial problems; and the graphic one, given its value as an execution of drawing, *i.e.*, as a simple material construction on a sheet of paper. These fields are still valid today, with the support of derived digital tools.

In Latin America, which harbors countries with a broken and irregular topography, with incalculable water resources in the rivers and seas, civil engineers, architects, topographers, mining engineers, electrical engineers, and mechanical engineers are required. The region's development is supported by the exploitation of its mineral and energy resources, in addition to agricultural exports. This range of needs ratifies descriptive geometry as an essential subject in the construction of the curriculum of knowledge, which determines the spatial development of engineering students.

In Latin America, descriptive geometry will never fall into disuse due to its contribution to the rigor and accuracy in science and engineering applications and its role in achieving a capacity for the rational perception of space, essential for operating in 2D on a sheet of paper. The ability to see in space, to rotate figures around one or more axes, and to interpret and provide real solutions to engineering problems in the transition from 3D to 2D only add to the importance of the subject.

2. Methodology

Considering that this research seeks to understand the development of the HER in favoring the learning of point and line within the Descriptive Geometry course in first-year students at Universidad Tecnológica de Pereira (UTP), a qualitative approach seemed to be the most appropriate choice, given the nature of the problem. However, given the use of the PSVT:R test before and after the didactic unit, we considered that it had nested quantitative aspects, given the nature of the data obtained in the test. Likewise, the scope of this research was comprehensive since it sought to specify properties, characteristics, and group profiles; some variables were discovered, and it was possible to add others to be measured (31).

2.1. Application of the PSVT test: R

Initially, we applied the test remotely to a group of 15 students, who signed an informed consent. The test took 20 minutes, and, after it was applied, Student's t-test was conducted based on the response template and two hypotheses:

- H_0. The HER test does not indicate that the students have spatial abilities.
- H_A. The test indicates that the students have spatial abilities.

Note that a statistical analysis was performed to identify trends and frequencies.

At this point in this document, we will look at the instruments used as tools to measure the students' prior ideas regarding point and line.

A. Instrument 1 – Intervention: measuring preconceptions
In the hydraulic circuit, shown in 3D (Fig. 1) and in 2D (Fig. 2), determine, based on the criteria of crossing or cutting lines, AND observing from the front view, whether or not:

a. the horizontal cold water pipe (blue, 1.98 m span) is below the hot water pipe (red, 3.14 m span)

b. the horizontal cold water pipe (blue, 1.98 m section) and the hot water pipe (red, 3.14 m section) represent two perpendicular lines

From the top view, based on the observation and analysis of the 2D (Fig. 3) and 3D (Fig. 4) representations, determine whether or not:

a. the 2.9 m cold water (PVC) lines and the 2.07 m diameter 1/2 hot water line are parallel

From the top 2D plan view and the right 3D side view (Fig. 4), determine whether or not:

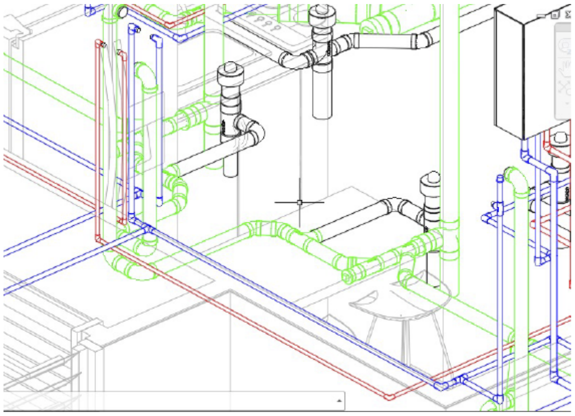

Figure 1. 3D plan of partial distribution, hydraulic circuit

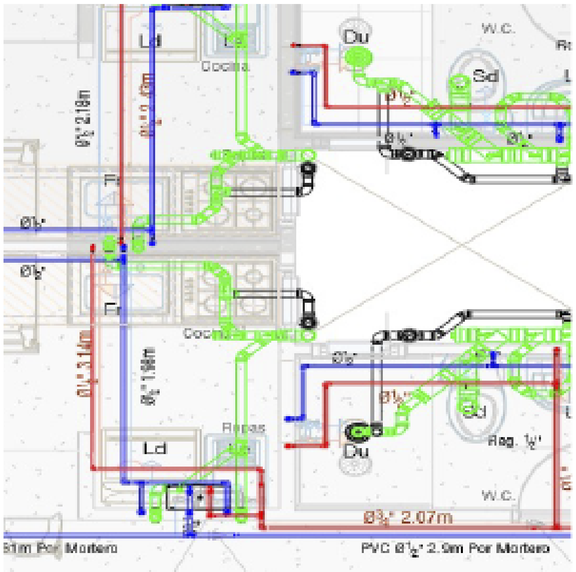

Figure 2. Partial hydraulic circuit, from plan view (top)

b. the 1/2 diameter cold water line (PVC) and the 1/2 diameter hot water line cross or intersect with the 3/4 diameter (black) sanitary sewer pipe

From the plan top view (Fig. 3), determine:

a. whether the main drain line (green), located on the right side of the plan, intersects the 3/4 diameter drainpipe (black)

b. whether the 1/2 diameter hot and cold-water lines are perpendicular, intersecting, or parallel to the black and green drain pipes in the layout (for this analysis, please refer to the 3D drawing provided in Fig. 4)

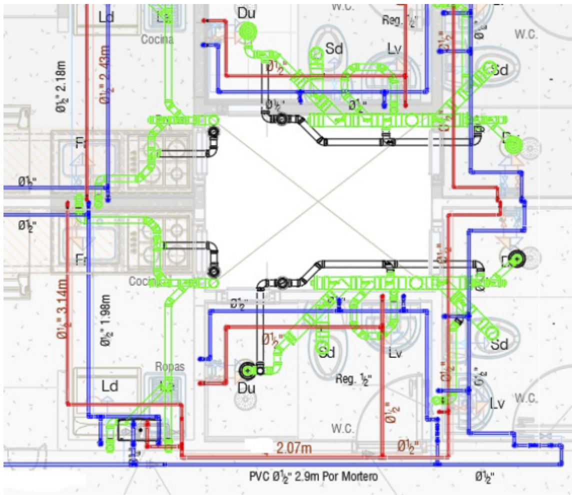

Figure 3. Partial hydraulic circuit, from plan view (top)

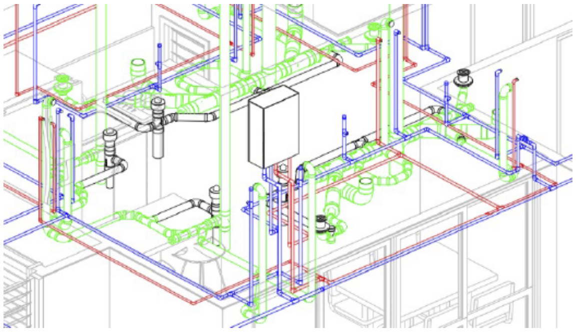

Figure 4. 3D plan of partial distribution, hydraulic circuit

In the HVAC system shown in 3D (Fig. 5) and 2D (Fig. 6), determine whether the medical air injection (blue) and the contaminated air extraction (green) ducts, represented by lines AB and CD, can be considered to be:

a) parallel lines

b) perpendicular lines

c) intersecting lines

d) don't know

In this plant representation, it is necessary to determine whether the air injection duct, which comes from the handling unit,

a) is represented by a line as a point

b) is perpendicular or parallel to the contaminated air duct

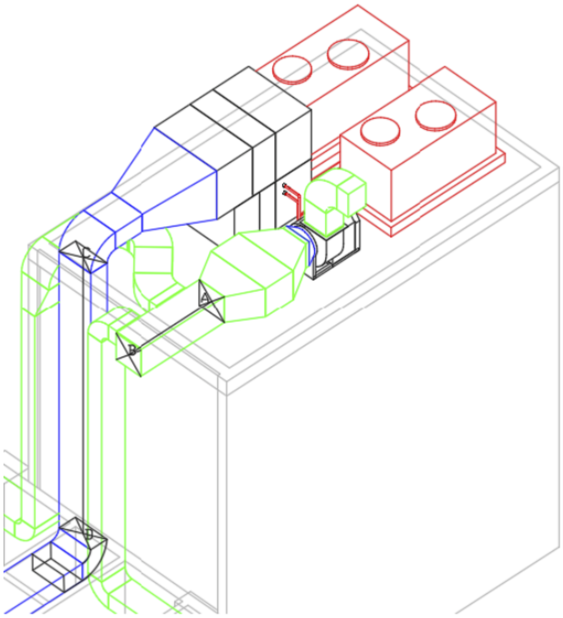

Figure 5. HVAC installation, 3D partial view

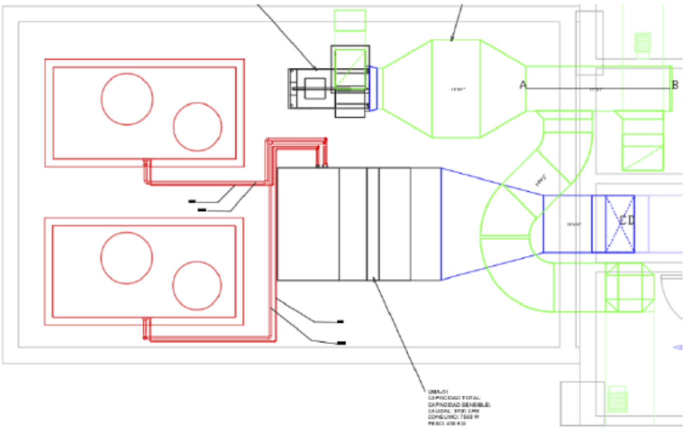

Figure 6. Partial view of the HVAC installation, 2D drawing

3. Results

The analysis of PSVT:R, both the pre-test and the post-test, by means of a Student's t-test (tendency and frequency) allowed determining the extent to which the students improved their HER with respect to both of the above-presented hypotheses (H_0 and H_A).

Tables I and II show the group of students along with their number of correct answers and their score.

Table I. Pre-test group results

Name	Correct answers	Score
1004520565	19	3.1
1089930820	24	4
1004719551	14	2.3
1006691398	19	3.1
1001331030	17	2.8
1003238617	20	3.3
1004684151	20	3.3
1116259674	29	4.8
1000077989	25	4.1
1088825177	26	4.3
1006319734	16	2.7
1126597041	21	3.5
1088824366	19	3.1
1069714443	17	2.8
1116279112	20	3.3

Table II. Pre-test student's T-test analysis

Grouped variance	21.18847619
Hypothetical difference of the means	0
Degrees of freedom	28
Statistics t	8.773535403
P(T<=t) one tail	0,791
Critical value of t (one-tailed)	1.701130934
P(T<=t) two tails	0.59126
Critical value of t (two-tailed)	2.048407142

3.1. Hypothesis

95 % confidence level with 14 degrees of freedom.

As the p-value (Excel output) for one tail is 0.791, it falls in the region of acceptance. Therefore, the null hypothesis is accepted: not all students have spatial thinking.

3.2. Hypothesis

95 % confidence level with 14 degrees of freedom.

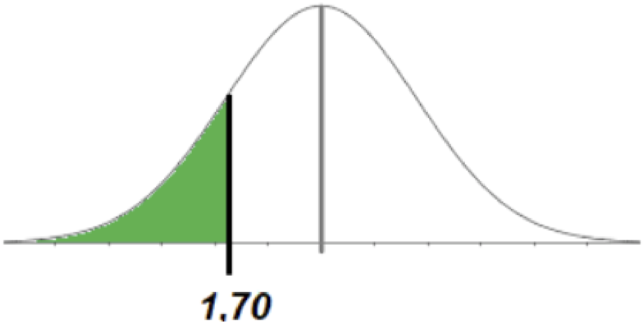

Figure 7. Student's t distribution

Table III. Post-test group results

Name	Correct answers	Score
1004520565	28	4.6
1089930820	24	4
1004719551	23	3.8
1006691398	19	3.1
1001331030	26	4.3
1003238617	21	3.5
1004684151	22	3.6
1116259674	27	4.5
1000077989	26	4.3
1088825177	27	4.5
1006319734	21	3.5
1126597041	21	3.5
1088824366	22	3.6
1069714443	21	3.5
1116279112	20	3.3

If the alternative hypothesis is accepted, then all students are able to think spatially.

It can be observed that the p-value for one tail is 0.0088. Since this value is lower than $\alpha = 0{,}05$, it can be said, with 95 % confidence, that the alternative hypothesis is accepted, which means that the students obtained a better average in the post-test.

3.3. Pre-test and post-test analysis

This subsection presents the analyses carried out in the SPSS software with regard H_0 and H_A. These hypotheses are presented below.

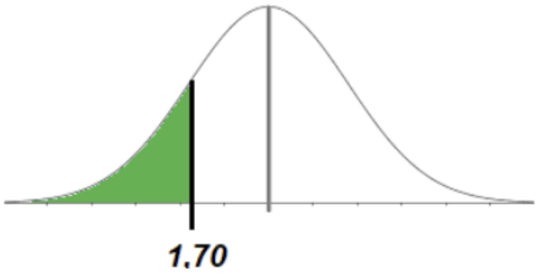

Figure 8. Student's t distribution

Table IV. Student's T-test post-test analysis

Media	19.71428571	3.264285714
Variance	44.21978022	1.217857143
Remarks	14	14
Grouped variance	22.71881868	
Hypothetical difference of means	0	
Degrees of freedom	26	
Statistic t	9.131077935	
P(T<=t) one tail	6.79371E-10	
Critical value of t (one-tailed)	1.70561792	
P(T<=t) two tails	1.35874E-09	
Critical value of t (two-tailed)	2.055529439	

Table V. Continued student's T-test post-test

Hypothetical difference of means	0
Degrees of freedom	13
Statistic t	-2.71861415
P(T<=t) one tail	0.008779643
Critical value of t (one-tailed)	1.770933396
P(T<=t) two tails	0.017559285
Critical value of t (two-tailed)	2.160368656

- H_0. The post-test is equal to the pre-test in grade point average.
- H_A. The post-test is higher than the pre-test in grade point average.

The alternative hypothesis is accepted, indicating that the students scored higher in the post-test.

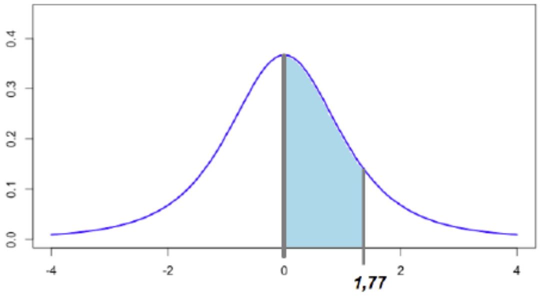

Figure 9. Analysis in EXCEL

Table VI. Pre-test and post-test student's T-test analysis

T-test for means of two paired samples		
	3.1	**4.6**
Media	3.385714286	3.78571429
Variance	0.481318681	0.20747253
Observations	14	14
Pearson correlation coefficient	0.610293958	
Hypothetical difference of the means	0	
Degrees of freedom	13	
Statistic t	-2.718614159	
P(T<=t) one tail	0.008779643	
Critical value of t (one-tailed)	1.770933396	
P(T<=t) two tails	0.017559285	
Critical value of t (two-tailed)	2.160368656	

3.4. Analyzing the test on the notion of point and line using Atlas ti 2023

After applying the test that measures the notion of point and line, some units of analysis were identified for each of the students. From them, some categories were established, with their corresponding codes. This was done using the Atlas ti 2023 software.

Initially, with the results of the PSVT:R, a quantitative analysis was performed. Regarding the qualitative analysis, we considered a work unit of four students for an in-depth case study. These students were selected because they had the lowest HER test scores.

Analysis 1006319734. It can be seen how, throughout this test, the student responds with her own criteria, rooted in her simple notion of point and the line, based on her preconceptions and life experiences (from their childhood, adolescence, and high school years).

1. From the analysis units [90.-b. the blue and red pipes FORM A 180° ANGLE], [49.-f. they do not cut because they are parallel], [98.-a. yes, they are parallel because they never cross], [58.-9. yes, they are parallel; these ducts never cross or cut], [73.-f. yes, they are parallel because they never cross], [60.-c. yes, ducts B and C are parallel, because they FORM A 180° ANGLE], [30.-f. parallel lines], [61.-d. yes, ducts D and E are parallel lines because they never touch each other], [29. they FORM A 180° ANGLE], [50. g. they do not cross, they FORM A 180° ANGLE], [48.-e. parallel because they never touch each other], and [31.-g. no, the lines never cross each other because they are parallel], the subcategory FORM A 180° ANGLE emerges, corresponding to the first preconceptions: the notion that everything on the planet is flat.
2. In the units of analysis [72.-e. yes they FORM A 90°ANGLE perpendicular ducts], [76.i. if the ducts (E, I) are perpendicular, they form a 90° angle], [59.b. if they are perpendicular, they FORM A 90° ANGLE], [127.b. yes, they are on different axes. They FORM A 90° angle], [126.a. no, because they are not on the same axis; they FORM A 90° ANGLE], and [75.h. no, they are parallel. They FORM A 90° ANGLE. They are perpendicular], the subcategory FORM A 90° ANGLE is identified as a category of an individual's first notions of knowledge regarding basic displacements in space.
3. In the units of analysis [46.c.2. vertical because it is the line CD], [28. d.2. VERTICAL LINE observed as a point from top view], [27. c.2. the line CD is observed from the front view, VERTICAL LINE], [47. d.2. vertical, because it is the line AB], the subcategory VERTICAL LINE is identified, which is associated with observing a line as a point from a plan view if this line is in its true length.
4. From the units of analysis [26.b. represented by the AB blue duct, clean air], [44.a. CD is green colored and ascending], [25.a. CD is green colored], [45.b. AB blue colored, carries medicinal air], the subcategory OBSERVATION arises.

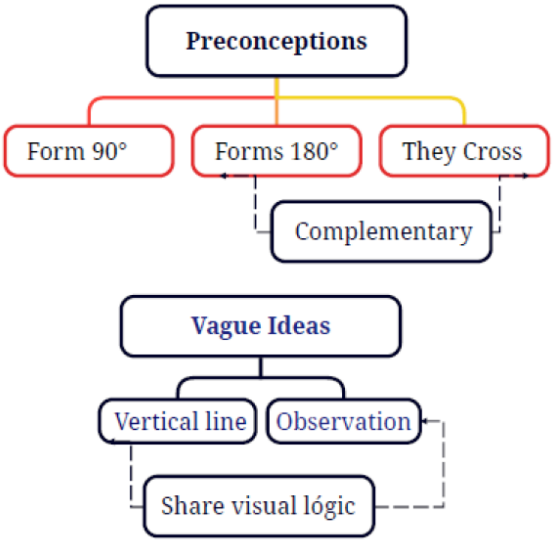

Figure 10. Axial coding: preconceptions and vague ideas

Analysis 1001331030. It is observed how the student answers this test with his own criteria, rooted in his simple notion of point and line, due to the ingrained prejudices from his childhood, adolescence, and high school years.

1. In the units of analysis [27.c. it is a VERTICAL LINE; in 3D, it is CD], [28.d. it is a VERTICAL LINE; according to 3D, it is AB], [46.c. the extraction duct represented by the VERTICAL LINE, green], and [10.a. it is a vertical duct], in interrelation with the unit [47.a. injection duct represented by a VERTICAL LINE, blue], the subcategory VERTICAL LINE is observed, which is related to the basic notion of the first graphs analyzed by the students.
2. From the units of analysis [44.a. the discharge duct represented by CD], [26.b. AB, because the air discharge duct is CD], [134.b. no, because they do not touch according to the 3D plan], [133.a. no, because one is vertical and the other is horizontal], [46.c. the extraction duct represented by the green vertical line], [47.d. injection duct represented by a blue vertical line], and [45.b. the injection duct represented by AB], the subcategory OBSERVATION arises.
3. For the subcategories VERTICAL LINE and OBSERVATION, there are two common units of analysis: [46.c. the extraction duct represented by the green vertical line] and [47.d. extraction duct represented by a vertical line, blue]. This is evidence of the visual logic and geometric affinity of the two sub-categories.
4. In the units of analysis [75.i. yes because, according to the 2D plane, they intersect at a point], [74.h. no because, according to the 2D plane, they intersect at a point], [73.g. yes because, according to the 2D plane, they intersect at a point], [58.b. ducts A and F are perpendicular according to the 2D plane], [105. b. no, in no part of the plane do they intersect], [120.b. according to the 3D plane, the pipes intersect], [86.b. no, because at no point in the 2D plane do they touch], [135.c. they do not intersect according to the 2D and 3D planes], and [134.b. no, because they do not touch according to the 3D plane], the subcategory FORM A 90° ANGLE arises, which is closely related to the OBSERVATION subcategory, as they have two coded units in common (134.b. and 133.a.) and are in coincidence or synchrony. This convergence demonstrates a geometric connection, which is visually perceived by the student during their exploration and inspection of the test.
5. From the units of analysis [105.b. no, in no part of the plane do they CROSS], [93.a. no because, in the 3D plane, there is a blue pipe above], [120.b. according to the 3D plane, the pipes CROSS], [86.b. no, because at no point in the 2D plane do they touch], and [85.a. no, because according to the 2D view, they do not CROSS], the subcategory CROSS emerges, defining lines that neither intersect nor are parallel and have different directions.
6. From the units [60.d. ducts D and E are parallel accordingFrom the units [60.d. ducts D and E are parallel according to 2D plan], [59.c. ducts B and C are parallel according from the 2D view], [72. yes, they are parallel according to the 2D plan], [49. they do not intersect or cut each other; AB and CD are parallel], [48.e. lines AB and CD are parallel], [57.a. ducts A and B are parallel according to the 2D plan], [30.f. they do not intersect; they do not cut], [71.e. yes, they form a 90° angle; lines G, H, and I are parallel], [29.e. the lines are parallel to each other], [94.b. no because, from the 2D view, the lines are parallel], [31.g. they do not intersect anywhere], [104.a. yes because from the 3D view, the pipes are parallel], [50.g. they do not intersect], and [93.a. no because, in the 3D

plane, the blue pipe appears to be above], the subcategory FORM A 180° ANGLE emerges, which is related to the fact that using 3D images is the best way to validate and recall student's prior ideas. to 2D plan], [59.c. ducts B and C are parallel according from the 2D view], [72. yes, they are parallel according to the 2D plan], [49. they do not intersect or cut each other; AB and CD are parallel], [48.e. lines AB and CD are parallel], [57.a. ducts A and B are parallel according to the 2D plan], [30.f. they do not intersect; they do not cut], [71.e. yes, they form a 90° angle; lines G, H, and I are parallel], [29.e. the lines are parallel to each other], [94.b. no because, from the 2D view, the lines are parallel], [31.g. they do not intersect anywhere], [104.a. yes because from the 3D view, the pipes are parallel], [50.g. they do not intersect], and [93.a. no because, in the 3D plane, the blue pipe appears to be above], the subcategory FORM A 180° ANGLE emerges, which is related to the fact that using 3D images is the best way to validate and recall student's prior ideas.

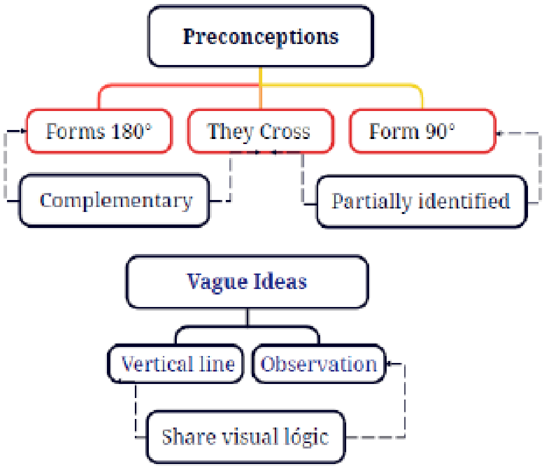

Figure 11. Axial coding: preconceptions and vague ideas

Analysis 1004719551. It is observed how, throughout this test, the student responds with defined criteria, reinforced by her primitive knowledge of point and line, by her prejudices and experiences from her childhood, adolescence, and secondary education years.

1. From the units of analysis [55. they are parallel lines], [94. they never intersect], [111. they are parallel lines (AB and CD); they never intersect], [29. they do not intersect], [69. parallel lines (D and E)], and [27. parallel lines (AB and CD)], the subcategory FORM A 180° ANGLE emerges. This subcategory reveals the logical coherence of the student's prior knowledge about the notion of 180° in space.
2. In the units [79. they do not cut because they CROSS], [85. in 3D, the cold water pipe CROSSES over the hot water pipe], [95. the cold and hot water pipes CROSS over the drain pipe], and [78. the hot and cold water pipes CROSS over the green and black drain pipes], the subcategory CROSS is observed, which, from a 3D view, allows the student to assume a logical position, based on the experience collected during her upbringing, adolescence, and puberty.

3. From the units of analysis [121.b. ducts AB and CD are perpendicular], [71.h. the ducts E and I form perpendicular lines], [56.b. A and F FORM A 90° ANGLE], [68.e. between ducts B and G, H and I FORM A 90° ANGLE], [72.i. ducts E and I are perpendicular], and [70.9. ducts C and G form perpendicular lines], the subcategory FORM A 90° ANGLE arises, which is related to the prior ideas of students, as these are the most common shapes in their context.
4. In the units [26. the AB line is vertical], [25.c. the CD line is vertical], [45.d. the AB line is vertical], [44.c. the CD line is vertical], the subcategory VERTICAL LINE is observed, which is associated, in a basic and primary way, with the first images that young students drew in their childhood.
5. From the units of analysis [43.b. AB carries medicinal air], [23. CD is green], [42.a. CD is green], and [24.b. AB is the blue duct and carries clean air], the subcategory OBSERVATION arises.

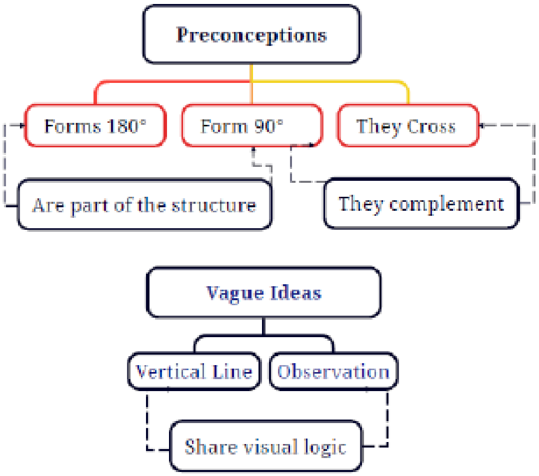

Figure 12. Axial coding: preconceptions and vague ideas

Analysis 1069714443. In this test, the student responds with the judgment or methods stemming from his basic notion of point and line, from the preconceptions and habits built throughout his childhood, adolescence, and passage high school years. taken from the network, 1069714443 Network Source: Atlas. Ti 23

1. Based on the units of analysis [58.c. the extraction pipeline is represented by a VERTICAL LINE], [30.c. the extraction pipeline is represented by the VERTICAL LINE CD], [10. because this line AB is represented as a VERTICAL LINE], [32.d. the injection pipeline is represented by the VERTICAL LINE AB], and [60.d. the injection pipeline is represented by a VERTICAL LINE], the subcategory VERTICAL LINE is defined, which is related to the first graphs studied by students in their first stage of school life.
2. In the units [30.c. the extraction duct is represented by the vertical line CD], [75.a. the ducts represented by the letters A and B are parallel lines], [36.f. the ducts represented by the lines AB and CD do not intersect], [109.b. the horizontal cold water pipes (blue) and the hot water pipe], [34.e. the ducts represented by the lines AB and CD are parallel], [92.f. the ducts denoted by the letters D and E are parallel lines], [118.a. yes, they are parallel lines because they never

intersect and form a 180° angle], [62.e. the ducts represented by the lines AB and CD are parallel], [66.g. the ducts represented by the lines AB and CD do not intersect], [64.f. the ducts represented by the lines AB and CD do not intersect], [28.b. the clean air injection duct is represented by the letters AB], [79. c. the ducts arranged between B and C are represented by two parallel lines], [38.g. the ducts represented by the lines AB and CD do not intersect], [54.a. the air discharge duct is represented by the letters CD], [81.d. they do not intersect because they are parallel lines, and, according to the 3D plan, they form a 180° angle], [56.b. the clean air injection duct is represented by the letters AB], [136.b. the hot and cold water lines are parallel and intersect the green and black drainage pipes], [95.i. the duct lines formed between E and I are perpendicular], [146.a. the ducts represented by AB and CD are not parallel lines; they intersect], the subcategory OBSERVATION is observed. This is related to the main characteristics of the student, and it allows him to react to the stimuli generated by any kind of action.

3. From the units [34.e. the ducts represented by lines AB and CD are parallel], [75.a. the ducts represented by letters A and B form parallel lines], [109.b. the horizontal cold water (blue) and hot water (red) pipes], [64.f. the ducts represented by the lines AB and CD do not intersect], [79.c. the ducts arranged between B and C represent two parallel lines], [38.g. the ducts represented by the lines AB and CD do not intersect], [92.f. the ducts represented by the letters D and E form parallel lines], [79.c. the ducts arranged between B and C represent two parallel lines], [81.d. they do not intersect because they are parallel lines, and, according to the 3D plan, they form A 180° ANGLE], [66.g. the ducts represented by the lines AB and CD do not intersect because they form parallel lines], [62.e. the ducts represented by lines AB and CD are parallel], [118.a. yes, they are parallel lines because they never intersect and FORM A 180° ANGLE], and [135.a. the 1/2 diameter green drainage line intersects the black 3/4 diameter drainage pipe; both pipes intersect], the subcategory FORM A 180° ANGLE arises. This implies that the student can see the difference between a line that crosses and one that intersects.

4. In the units [28.b. the clean air injection duct is represented by the letters AB, blue], [26.a. the air discharge duct is represented by the letters CD], [56. the clean air injection duct is represented by the letters AB], and [108.a. the cold water pipe is passing over the hot water pipe], the subcategory DESCRIPTION appears. Students can recognize the vague idea of confusing intersecting lines with a simple description.

5. Based on the units of analysis [108.a. the chilled water pipe is passing over hot water pipe], [119.b. the 1/2 diameter chilled water (PVC) lines and the hot water line intersect the sewer pipe], [100. 101.a. the 5/8 and 1 1/8 diameter cooling pipes and injection duct CROSS each other], [146.a. the AB and CD ducts do not form parallel lines; they CROSS], [148.c. the AB and CD ducts CROSS each other, because they form a 90° angle], and [101. they CROSS each other because it can be seen in the 3D plan which clean air duct is above the other], the subcategory CROSS is defined. This is the reason why the ducts form 180° angles and lines that do not intersect and are not parallel. They have different directions and no common points.

6. In the units of analysis [93.g. the lines of ducts C and G are perpendicular], [147.b. the ducts AB and CD correspond to perpendicular lines], [91.e. between duct B and the line of variable section of ducts G, H, and I, there are perpendicular lines], [77.b. between duct A and F, there are two

perpendicular lines], [94.h. the lines of ducts D and H are not parallel], [136.b. the hot and cold water lines are parallel and intersect at 90° with the green and black drainage pipes], [95.i. the lines formed between ducts E and I are perpendicular], [148.c. the ducts of AB and CD intersect because they FORM 90° ANGLES], and [119.b. the 1/2 diameter cold water lines (PVC) and the hot water line intersect the drainage pipe], the subcategory FORM A 90° ANGLE is observed. Two lines are perpendicular if one of them is in true length and forms an angle of 90° with respect to the other.

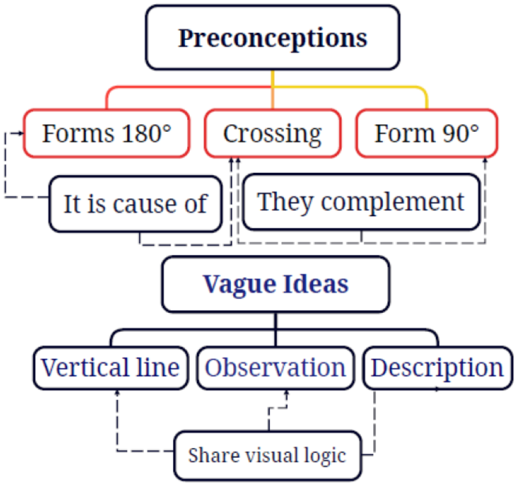

Figure 13. Axial Coding: preconceptions and vague ideas

4. Conclusions

In the studied group of students, the development of the HER was demonstrated, as a result of testing prior ideas in 3D regarding point and line. As a consequence, the results of the standardized test, called *post-test* (PSVT:R), were obtained. Since the p-value (Excel output) for one tail is 0.0000000679, it falls in the rejection region. Therefore, the alternative hypothesis is accepted: all students have spatial thinking.

In the analysis of the pretest and posttest, it can be observed that the p-value for one tail is 0.0088. Since this value is less than α=0.05, it can be said, with a confidence level of 95 %, that the alternative hypothesis is accepted, which means that the students obtained a better average in the post-test.

Through the analysis conducted via the Atlas ti tool, it was possible to observe that the students answered the test with their own criteria, rooted in their traditions and customs, which allow them to express and respond from their primitive and simple notion of point and line, a notion that is influenced by their experiences, prejudices, and habits and molded since their childhood, adolescence, and high school stages.

5. CRediT author statement

H. Parra-Lara: conceptualization, data curation, formal analysis, investigation, methodology, software, validation, visualization, writing (original draft). *C. A. Ospina-Parra:* project administration, supervision, writing (review and editing).

References

[1] M. C. Linn and A. C. Petersen. ”Emergence and characterization of sex differences in spatial ability: A meta-analysis,” *Child Dev.*, vol. 56, no. 6, pp. 1479-1498, 1985. https://doi.org/10.2307/1130467 ↑3

[2] D. F. Lohman, "Spatial ability: Individual differences in speed and level. Technical Report No. 9. Aptitude Research Project,” Stanford Univ., CA, School of Education, 1979. ↑3

[3] G. McGee, "Human spatial abilities: Psychometric studies and environmental, genetic, hormonal and neurological influences,” *Psychol. Bulletin*, vol. 86, no. 5, pp. 889-918, 1979. https://doi.org/10.1037/0033-2909.86.5.889 ↑3

[4] S. A. Sorby and B. J. Baartmans, "The development and assessment of a course for enhancing the 3-D spatial visualization skills of first year engineering students,” *J. Eng. Edu.*, vol. 89, 2000. https://doi.org/10.1002/j.2168-9830.2000.tb00529.x ↑3

[5] D. Jaison, M. B. Weaver, and S. Ray, “WIP teaching engineers to sketch: Impacts of feedback from an intelligent tutoring software on engineers’ sketching skill development,” in *2022 IEEE Front. Edu. Conf. (FIE)*, 2022. [Online]. Available: https://doi.org/10.1109/FIE56618.2022.9962419 ↑3

[6] A. A. Kahharov, Ïntensive methods of developing students’ spatial imagination in the teaching of graphic sciences,” *Annals Romanian Soc. Cell Biology*, vol. 25, no. 4, art. 11885, 2021. [Online]. Available: http://annalsofrscb.ro/index.php/journal/article/view/4042 ↑3

[7] N. A. Aguilera-González, "How to include augmented reality in descriptive geometry teaching,” *Procedia Comp. Sci.*, vol. 75, pp. 250-256, 2015. https://doi.org/10.1016/j.procs.2015.12.245 ↑3

[8] K. Dent and M. M. Smyth, Çapacity limitations and representational shifts in spatial short-term memory,” *Visual Cog.*, vol. 13, no. 5, pp. 529-572, 2006. https://doi.org/10.1080/13506280444000760 ↑3

[9] K. Cotton and T. J. Ricker, ”Examining the relationship between working memory consolidation and long consolidation,” *Psychonomic Bulletin Rev.*, 2022. https://doi.org/10.3758/s13423-022-02084-2 ↑3

[10] O. Ha and N. Fang, "Spatial ability in learning engineering mechanics: Critical review,” *J. Prof. Issues Eng. Edu. Prac.*, vol. 142, no. 2, art. 0000266, 2016. https//doi.org/10.1061/(ASCE)EI.1943-5541.0000266 ↑4

[11] J. Buckley, D. Canty, and N. Seery, "Spatial working memory in mental rotations: A case for exploring neural efficiency and cognitive strategies," 2018. [Online]. Available: https://sites.asee.org/edgd/wp-content/uploads/sites/22/2018/07/43-J-Buck.pdf ↑4

[12] B. N. Verdine, R. M. Golinkoff, K. Hirsh-Pasek, and N. S. Newcombe, "Spatial skills, their development, and their links to mathematics," *Links Spatial Math. Skills Preschool Years*, vol. 82, no. 1, pp. 7-30, 2017. https://doi.org/10.1111/mono.12280 ↑4

[13] L. M. Weckbacher and Y. Okamoto, "Mental rotation ability in relation to self- perceptions of high school geometry," *Learn. Indiv. Diff.*, vol. 30, pp. 58-63, Feb. 2014. https://doi.org/10.1016/j.lindif.2013.10.007 ↑4

[14] C. Carbonell Carrera, J. L. Saorín, and S. Hess-Medler, "Spatial orientation skill for landscape architecture education and professional practice," *Land*, vol. 9, no. 5, art. 161, 2020. https://doi.org/10.3390/land9050161 ↑4

[15] M. Giner, "Problemas en el desarrollo de la lateralidad," 2007. [Online]. Available: http://psicopedagogias.blogspot.com.es/2007/11problemas-en-el-desarrollo-de-la.html ↑4

[16] C. Ramos, I. C. Angel, U. G. López, M. Y. M. Cano, and R. Core, Çore elements of STEM approach educational experiences," *Rev. Científica*, vol. 45, no. 3, art. 19298, 2022. https://doi.org/10.14483/23448350.19298 ↑4

[17] F. N. Jiménez, L. Beleño, J. Agudelo, and J. L. Muñiz, "Didactic units in physics as learning enhancers for engineering students," *Form. Univ.*, vol. 13, no. 6, pp. 143-154, Dec. 2020. https://doi.org/10.4067/S0718-50062020000600143 ↑4

[18] M. Prosser, K. Trigwell, E. Hazel, and F. Waterhouse, "Students' experiences of studying physics concepts: The effects of disintegrated perceptions and approaches," *Eur. J. Psychol. Edu.*, vol. 15, pp. 61-74, 2000. https://doi.org/10.1007/BF03173167 ↑5

[19] L. S. Nadelson, B. C. Heddy, S. Jones, G. Taasoobshirazi, and M. Johnson, Çonceptual change in science teaching and learning: Introducing the dynamic model of conceptual change," *Int. J. Edu. Psychol.*, vol. 7, no. 2, pp. 151-195, Jun. 2018. https://doi.org/10.17583/ijep.2018.3349 ↑5

[20] M. J. Kirker and I. Stonebraker, .ᴬrchitects, renovators, builders, and fragmenters: A model for first year students' self-perceptions and perceptions of information literacy," *J. Acad. Librarianship*, vol. 45, no. 1, pp. 1-8, Jan. 2019. https://doi.org/10.1016/j.acalib.2018.10.009 ↑5

[21] S. A. Sorby, "Educational research in developing 3-D spatial skills for engineering students," *Int. J. Sci. Edu.*, vol. 31, no. 3, pp. 459-480, Feb. 17, 2009. https://doi.org/10.1080/09500690802595839 ↑5

[22] T. J. van Weert and A. Pilot, "Task-based team learning with ICT: Design and development of new learning," *Edu. Info. Tech.*, vol. 8, pp. 95-214, Jun. 1, 2003. https://doi.org/10.1023/A:1024562515675 ↑5

[23] S. A. Sorby, T. Drummer, and R. Molzon, "Experiences in using spatial skills testing instruments with younger audiences," *J. Geom. Graph.*, vol. 10, no. 2, pp. 227-235, 2006. [Online]. https://www.heldermann-verlag.de/jgg/jgg10/j10h2sorb.pdf ↑5

[24] J. Houser and C. Kloesel, *Obra filosófica reunida de Charles Sanders Peirce*, vol. I (1867-1893). Mexico: Fondo de Cultura Económica, 2012. ↑6

[25] J. Dewey, *Cómo pensamos*. Barcelona, Spain: Ediciones Paidós Ibérica S.A., 1989. ↑6

[26] Z. C. G. Escobar, "De la ruptura a la sutura de la secuencia tecnológica desde las posibilidades divergentes del pragmatismo: a partir del pensar, el aprender y el creer,"PhD dissertation, Universidad Tecnológica de Pereira, Pereira, Colombia, 2017. ↑6

[27] R. Guay, *Purdue Spatial Visualization Test: Rotations*, 1977. ↑6

[28] B. M. del R. Ordaz, "Diseño de un producto multimedia como recurso que coadyuve al proceso de enseñanza-aprendizaje de la geometría descriptiva en las licenciaturas de diseño,"MS thesis, Universidad Autónoma Metropolitana, 2010. ↑6

[29] S. A. Sorby, Üsing adaptive comparative judgment to holistically assess creativity of design solutions: A comparison of first-year students and educators' judgments,ïn *Annual Conf. Expo. Harbor Eng. Edu*. 30 Years, 2023. ↑7

[30] J. M. Gentil, "Papel de la geometría descriptiva en la enseñanza de la arquitectura,"1986. [Online]. Available: `https://idus.us.es/bitstream/handle/11441/51269/papel%20de%20la%20geometria.pdf;jsessionid=B9AD368CA06EF768B8F5351F88CCDCFA?sequence=1` ↑7

[31] R. Hernández, S. Fernández, C. Baptista, P, *Metodología de la investigación*, 6th ed. Mexico, D.F., Mexico: McGraw-Hill Education, 2014. ↑8

Carlos Alberto Ospina Parra

PhD in Education, with an emphasis on Pedagogy, Didactics, and Curriculum in University Education, as obtained from Rudecolombia, the network of state universities of Colombia (Universidad de Caldas, Universidad de Cartagena, Universidad del Cauca, Universidad de Nariño, Universidad Tecnológica de Pereira, Universidad del Tolima, Universidad Pedagógica y Tecnológica de Colombia, Universidad del Atlántico). Universidad de Manizales. Manizales. Geological Engineer, National University of Colombia, Medellín. Director of doctoral, master's, and bachelor's theses; member of doctoral, master, and bachelor thesis committees. University professor (undergraduate and postgraduate studies, in addition to the Doctoral Program in Development and Environment the Doctoral Program in Education and Diversity, and the Doctoral Program in Science Education).
Email: carlosospinaparra@umanizales.edu.co

Hernando Parra Lara

Mechanical engineer, Universidad Autónoma (1991), Specialist in Physical Instrumentation, Universidad Tecnológica de Pereira (UTP, 1996), Master of Physical Instrumentation, UTP (2009), Doctoral candidate in Didactics, Faculty of Education Sciences, UTP. Since 2013, he is a professor at the Department of Drawing, Faculty of Basic Sciences, UTP.
Email: heparra@utp.edu.co